2012

Thermophysical properties study of micro/nanoscale materials

Xuhui Feng
Iowa State University

Thermophysical properties study of micro/nanoscale materials

by

Xuhui Feng

A dissertation submitted to the graduate faculty

in partial fulfillment of the requirements for the degree of

DOCTOR OF PHILOSOPHY

Major: Mechanical Engineering

Program of Study Committee:
Professor Xinwei Wang, Major Professor
Professor Song Zhang
Professor Hui Hu
Professor Gap-Yong Kim
Professor Qingze Zou

Iowa State University

Ames, Iowa

2012

TABLE OF CONTENTS

LIST OF FIGURES

LIST OF TABLES

ACKNOWLEDGEMENT

Although I am the only author for this dissertation, a great many people have contributed to its production. Therefore I owe my gratitude to those who provide guidance, instructions and comments to my research work, who help me with the experiment, and also who supports me with full heart, love and patience.

First and foremost, I want to give my deepest gratitude to my adviser, Dr. Xinwei Wang. It was great fortune to have him as my adviser who shares his excellence, caring and patience. His wise guidance always ensures me at the right track to success, while his patience and support helped me to overcome many crisis situations, both in research work and in personal life. Meanwhile, I am also deeply grateful to those professors who are on my committee, Dr. Song Zhang, Dr. Hui Hu, Dr. Gap-Yong Kim, Dr. Qingze Zou, and previous members, Dr. Cheryl Farr and Dr. Zhiqun Lin, for their time and efforts spent on my work. It is always my pleasure to have these professors who would share their ideas that has significantly enlightened me.

Most importantly, none of this would have been achieved without the love and support from my family. My family, to whom this dissertation is dedicated to, has been always unaltered source of love, caring and strength. I would like to express my gratitude to my wife, Fei, for her support, encouragement and unwavering love. I also thank my parents, my little brother and my lovely angle, Yanyan. I would never have come this far without

their love. Special thanks are given to all colleagues and friends, Xiaopeng Huang, Yanan Yue, Xiangwen Chen, Guoqing Liu, Xiaoduan Tan, Jingchao Zhang, Huan Lin, Zaoli Xu, Shen Xu, Chong Li and Nathan. It was wonderful and inspiring time working with them.

Finally, Support of this work from the National Science Foundation is gratefully acknowledged.

ABSTRACT

Thermal transport in low-dimensional structure has attracted tremendous attentions because micro/nanoscale materials play crucial roles in advancing micro/nanoelectronics industry. The thermal properties are essential for understanding of the energy conversion and thermal management. To better investigate micro/nanoscale materials and characterize the thermal transport, pulse laser-assisted thermal relaxation 2 (PLTR2) and transient electrothermal (TET) are both employed to determine thermal property of various forms of materials, including thin films and nanowires.

As conducting polymer, Poly(3-hexylthiophene) (P3HT) thin film is studied to understand its thermal properties variation with P3HT weight percentage. 4 P3HT solutions of different weight percentages are compounded to fabricate thin films using spin-coating technique. Experimental results indicate that weight percentage exhibits impact on thermophysical properties. When percentage changes from 2% to 7%, thermal conductivity varies from 1.29 to 1.67 W/m·K and thermal diffusivity decreases from 10^{-6} to 5×10^{-7} m^2/s. Moreover, PLTR2 technique is applied to characterize the three-dimensional anisotropic thermal properties in spin-coated P3HT thin films. Raman spectra verify that the thin films embrace partially orientated P3HT molecular chains, leading to anisotropic thermal transport. Among all three directions, lowest thermal property is observed along out-of-plane direction. For in-plane characterization, anisotropic ratio is around 2 to 3, indicating that the orientation of the molecular chains has strong impact on the thermal transport along different directions.

Titanium dioxide (TiO_2) thin film is synthesized by electrospinning features porous structure composed by TiO_2 nanowires with random orientations. The porous structure caused significant degradation of thermal properties. Effective thermal diffusivity, conductivity, and density of the films are $1.35\sim3.52\times10^{-6}$ m^2/s, 0.06~0.36 W/m·K, and 25.8~373 kg/m^3, respectively, much lower than bulk values. Then single anatase TiO_2 nanowire is synthesized to understand intrinsic thermophysical properties and secondary porosity. Thermal diffusivity of nanowires varies from 1.76 to 5.08×10^{-6} m^2/s, while thermal conductivity alters from 1.38 to 6.01 W/m·K. SEM image of TiO_2 nanowire shows secondary porous surface structure. In addition, nonlinear effects are also observed with experimental data. Two methods, generalized function analysis and direct capacitance derivation, are developed to suppress nonlinear effects. Effective thermal diffusivities from both modified analysis agree well with each other.

CHAPTER 1. INTRODUCTION

1.1 Thermal transport in one-dimensional structures

The thermal transport in solid materials is fulfilled by the transport (movement and collision) of phonons (dielectric or semiconductive materials) and free electrons (metals). In micro/nanoscale materials, thermal transport is anticipated to be drastically different from that in its bulk counterparts. Therefore heat transfer in micro/nanoscale materials deserves special and attention and treatment due to several reasons: firstly, the size of material is comparable to characteristic length of phonons, such as mean free path and wavelength; secondly, existence of grain boundaries and crystal imperfections significantly alters the movement and transport of energy carriers; thirdly, under micro/nanoscale, the heat transfer is usually induced by ultrafast thermal excitation, such as picoseond ($\sim 10^{-12}$s) or femtosecond ($\sim 10^{-15}$s) laser-material interaction. These spatial and temporal constrains strongly confine and impact the transport of energy carriers (electron/phonon) and induce impedance to heat transfer. Practically, the most straightforward consequence observed is the accumulation of thermal energy and degradation of thermal performance in micro/nanoelectronics. With the rapid development of semiconductor industry, both size and dimension of the electronic components are highly reduced. However, the demands for power and reliability become unprecedentedly strong and urgent. Therefore, investigation of the thermal transport in micro/nanoscale materials would be critical to the advancement of semiconductor industry. Two relevant aspects would be discussed in this work. The first

aspect is to seek for novel candidates that present excellent thermal properties and contribute better thermal system management. The second one is to develop more efficient and precise techniques to investigate the thermal transport in the candidates.

1.1.1 Thin films

Low-dimensional nanostructures, including films, wires, fibers, tubes and rods, have demonstrated their inspiring novelties and promising utilizations in various industries, such as electronics, optical, energy and micromechanical industries [1]. Especially for thin film coating that has been widely used in micro/nanoscale devices, the heat transfer within such small scale strongly influences the thermal performance of micro/nanoscale transistors, solid-state lasers, sensors and actuators [2]. Different from conventional films, size effect presents more significant impacts on thermal transport within thin films. In addition the thermal transport in thin films is strongly influenced by structural imperfections introduced during the delicate fabrications process. Therefore, depending on the various fabrication techniques, to understand thermal properties of synthesized thin films becomes increasingly essential for heat transfer analysis in micro/nanoscale devices. Cahill [3] reviewed several measuring techniques for studying films of wide range of thicknesses. 3ω technique is capable of measuring films of tens of um thickness and is examined to be insensitive to radiative heat loss. For film that has thickness less than 10 um, another technique [4] is used by measuring the thermal boundary resistance that produces temperature drop at the interface between two solids. Phonon scattering mechanisms were also considered in this

experiment and it is found that the thermal conductivities of thin amorphous and crystalline films can differ significantly from the bulk materials. Goodson [5] investigate the thermal conduction in amorphous dielectric layers that affect the performance and reliability of electronic circuits and predicted the influence of phonon-boundary scattering on the effective conductivity normal to the layers. Same technique of Swartz and Pohl [4] was adapted and the results of SiO_2 layer fabricated using oxygen-ion implantation (SIMOX) presented consistency with the bulk samples, indicating that neither thermal boundary resistance nor highly resistive interfacial layers are present. The temperature and thickness dependence of heat transport for SiO_2 and SiNx films of 20-300 nm thick that were fabricated by plasma-enhanced chemical vapor deposition were investigated by Lee and Cahill [6] using 3ω method. It was found that the thermal conductivity has little dependence on film thickness for films as thin as 100nm. If thickness of film is reduced to be smaller than 50nm, thermal conductivity decreases with the film thickness. For polymer films, the in-plane and out-of-plane thermal conductivities of spin-coated polyimide films with thicknesses between 0.5 and 2.5 μm were studied with various techniques. Data reported indicated that the lateral thermal conductivity is larger by a factor of six than the effective vertical thermal conductivity for the films studied.

For particular solid thin films that are reported in this report, both polymer films and inorganic materials with different interior structures are included. As a promising organic polymer material, P3HT has been proven to have advantages over conventional

semiconductors in light of weight, processability and environmental sustainability while it still has electrical conducting property similar to semiconductors. This polymer material has become an essential subject of interest for both academic and industrial researchers. Various achievements have been reported regarding its development [7]. Synthesis of P3HT was conducted and significant attentions have been paid on improving the regioregularity and controlling the molecular weight and polydispersities of the fabricated P3HT [8-13]. Although the preparation of P3HT has been widely studied, it is still a complicated chemical or electrochemical process for non-chemistry professionals, not to mention to fabricate P3HT of defined molecular weight or specific regioregularity. The availability of commercial-grade P3HT has substantially boosted in-depth and extensive research on developing various forms of P3HT such as thin films [14-21], microwires [16, 21, 22] and nanofibers [21, 23-28], and also on their electrical, optical and thermal properties in practical applications such as photovoltaic cells and field-effect transistors. In order to determine the density of P3HT film, an atomic force microscopy (AFM) in combination with Rutherford backscattering spectroscopy data was applied and the density was estimated at 1.33 ± 0.07 g/cm^3 [14]. The thermal behavior and morphology transition of P3HT thin films developed by spin-casting was studied by Hugger *et al.* [15] using x-ray diffraction measurements with AFM data. The transition temperature was found about 225 °C and a layered and smectic liquid crystalline phase of P3HT formed. Another efficient method to promote order-disorder transformation of P3HT in solution by ultrasonic oscillation was presented by Zhao *et al.* [29]. Upon ultrasonic oscillating, chain

entanglements were decreased in the ordered precursors. 4 minutes was enough to yield the best crystallinity of the film. The intrinsic photoconductivity of P3HT polymers was measured and conclusion was made that higher mobility is associated with higher molecular weight by using optical pump-THz probe spectroscopy [17]. A study [30] on the molecular structure of P3HT indicated that a rotation of the planes containing the conjugated rings in P3HT substantially contributed to electrical conductance: the rotation reduces the electron and hole bandwidths and opens up the energy gap between occupied and empty states. To enhance the conductance of P3HT, germanium endometallo fullerene was added into P3HT matrix and the temperature is also significant to this adding process for achieving high conductance [31]. In practical applications, P3HT was adopted to synthesize a composite with phenyl-C61-Butyric acid methyl ester (PCBM) as the active layer in polymer photovoltaic cells. It was proven that heat treatment dramatically improved the cell's performance. The power conversion efficiency was improved up to 2.8% under white light illumination because the annealing contributed to optimizing both the donor/acceptor morphology [32]. Research by Janssen *et al.* [18] also revealed the effect of thermal treatments in optimizing the morphology of P3HT/PCBM films for organic solar cells by monitoring the optical absorption and resonant Raman scattering.

Additionally, for P3HT film, of particular interest is the often strong anisotropy caused by molecular structures. Fabrication process such as spin-coating or stretching could yield highly aligned molecular structures along the deformation direction, and consequently

yield highly anisotropic properties, for instance, the thermal properties that we will study in this work. Study of anisotropy has already been conducted on numerous polymers. Models by Henning [33] and Hansen [34] were proposed to account for the impact of molecule orientation on the thermal transport in amorphous polymers. For semicrystalline polymers, the molecular alignment can results in larger anisotropy than that in fully-amorphous polymers. Choy's model [35] to study the anisotropic thermal transport in polymer material adopted the thermal conductivity of crystallite perpendicular and parallel to molecular orientations, along with geometrical definition for the orientation of the crystallite and draw direction. Experimental investigations of the anisotropic heat conduction in stretched polymers have been conducted by several groups. Kilian and Pietralla [36] measured the dependence of anisotropy factor of thermal diffusivity of uniaxial stretched polyethylene. Results showed that the intrinsic anisotropy factor ranges from about 2 for completely amorphous structure to about 50 for completely crystalline polymers, respectively. Rantala [37] measured the anisotropic ratio of thermal conductivity of plastic foils whose thicknesses were about 30-100 μm and draw ratios was from about 2 to 8. The determined anisotropic ratios vary in small range 1-2. Piraux's work [38] proved that for highly orientated structures, the thermal conductivity is enhanced by 15 to 60 times higher than that of non-orientated polyacetylene. Choy [39] developed a pulsed photothermal radiometry technique by combining a line-shaped laser beam with laser-flash radiometry method. This technique is able to measure the thermal conduction behaviors for bi-axially stretched polymer films. A polyethylene film with a draw ratio of 200 was measured and

the anisotropy with thermal diffusivity was determined to be even greater than 90. Kurabayashi's work [40] presented three techniques to examine the vertical and lateral thermal conduction in polymer film on substrate. Data reported indicates that the lateral thermal conductivity is larger by a factor of six than the effective vertical thermal conductivity when the film thickness varies between 0.5 to 2.5 μm. Harmonic joule heating technique [41, 42] was employed to study the anisotropic thermal conductivity of dielectric films. This technique employs metal lines that serve as both heater and thermometer. The lateral spreading of heat inside the film changes the one-dimensional temperature field to achieve the purpose of measuring anisotropic thermal conductivity. For solution-cast P3HT films, the temperature dependence of anisotropic conductivity was investigated by Liu [43], indicating that conductivity in the perpendicular direction increases with increasing temperature while conductivity along parallel direction decreases greatly after 50 ºC. This change is attributed to structural anisotropy variation with temperature change. Thermoreflectance imaging technique [44] with localized heat source provides an instant and detailed description of the 2-dimensional thermal maps of area surrounding the heat source. It is valid for materials with either isotropic or anisotropic in-plane/out-of-plane thermal conductivity in thin films.

Different synthesis methods of P3HT film, such as solvent casting and spin coating, are widely used to produce P3HT thin film [15]. In solution-casted thin films, P3HT forms needle or plate like crystallites oriented with respect to the substrate, while in spin-coated

P3HT film, non-equilibrium structures with reduced order and orientation is always displayed. In this work, free-standing spin-coated P3HT thin film is fabricated for anisotropic thermal transport investigation. Two transient techniques will be applied for thermal characterization. Pulsed laser-assisted thermal relaxation 2 (PLTR2) [45], which is capable to characterize both in-plane and out-of-plane thermal transport, will be used to measure the 3-dimensional anisotropic thermal properties. Another technique, transient electrothermal (TET) [46, 47] is used as a validation of the results from PLTR2. In addition, TET could be used to determine the anisotropic thermal conductivity. TET technique was used in our group to investigate the thermophysical properties of P3HT films fabricated from solution with different concentrations of P3HT content [47]. Concentration of P3HT content in the solution not only impacts the thickness of the spin-coated thin film, it has also strongly influenced the thermophysical properties. When studying the anisotropic thermal transport in P3HT thin films, the concentration of P3HT content in the solution is fixed at 2%, in order to keep the thickness of P3HT film to be around a few tens of microns, and also to eliminate irrelevant impact on thermal properties.

Due to its unique properties in photocatalytic decontamination [48], sensor materials [49, 50], dye-sensitized solar cells [51] and also photoelectrochemical cells [52], titanium dioxide (TiO_2) of low-dimensional nanostructures, has been intriguing considerable attentions of both fundamental and practical perspectives when altering the particle sizes, crystalline state and morphology [53, 54]. Intensive and in-depth applications of TiO_2

nanostructures are reported recently. A varieties of techniques are used for have been employed for synthesizing TiO_2 nanostructures, such as sol-gel method [55-61], chemical vapor deposition [62, 63], hydrothermal reaction [64-70], anodic oxidation [71-75], electrospinning [76-83] and many others [84-93]. The properties of TiO_2 nanostructures vary substantially with the synthesis principles [94] and large collections of studies and achievements have been reported regarding their electrical and thermal properties and how they are influenced by various TiO_2 nanostructures, including TiO_2 nanofibers [76-79, 81-83], nanopowders [95], nanotubes [96, 97], nanowires [98-102] and thin films [103-109]. Among all micro/nanostructures, TiO_2 thin film, which can be fabricated via several methods [103-109], is substantially important to several applications, such as protective coatings, microelectronic applications, optical coatings, and photochemically active layers. The research on physical properties of TiO_2 thin film has been carried out focusing on diverse aspects. The electrical conductivity of TiO_2 thin films was studied by Zhao *et al.* [110] to explore the effect of film thickness and the material of substrate on which the film is deposited by magnetron sputtering. For thermal properties, Zhang *et al.* [111] investigated the thermal diffusivity of nano-structured TiO_2 thin films on silicon substrate and concluded that the thermal diffusivity is also dependent on the film thickness and annealing temperature. Moreover, plenty of findings have been reported on the thermal conductivity, which is the key property in determining the capability of TiO_2 to transfer heat. A direct reading thermal comparator [112] was used to measure the thermal conductivity of TiO_2 thin-film coatings and it is found that the thermal conductivity is

several orders of magnitude lower than that of bulk material. For electron-beam (EB) deposited and ion-plated (IP) thin films of TiO_2, Wu *et al.* [113] studied both absorption and thermal conductivity. The films fabricated by EB and IP techniques both show much lower thermal conductivity than bulk material while IP coatings presented higher thermal conductivity. Cahill *et al.* [114] also measured the thermal conductivity of TiO_2 optical coatings fabricated by reactive evaporation and ion beam sputtering, and the results indicated a thermal conductivity of about 6-16 mW/cm·K, which is lower than reported value for bulk TiO_2. 3ω method was adopted by Lee *et al.* [115] to measure the thermal conductivity of rutile-structured micro-crystalline TiO_2 film and a strong dependence of the thermal conductivity on the substrate temperature was observed. When the substrate temperature is around 400 ºC the thermal conductivity approaches the bulk value of about 8 W/m·K. In-plane thermal conductivity of TiO_2 thin film [116] was measured using the thermo-reflectance method and the results indicated to be one order of magnitude smaller than the bulky value. TiO_2 films of different phases including crystalline, non-crystalline and amorphous were all measured by Martan *et al.* [117] using a two-detector measurement system of pulse photothermal radiometry. The measurement revealed that the anatase embraced higher thermal conductivity than rutile and amorphous phases. Maekawa *et al.* [63] investigated the TiO_2 films grown by MOCVD and the relationship between the microstructure and thermal conductivity, showing that the feather-like texture film exhibited extremely lower thermal conductivity than bulk TiO_2. Cross-plane thermal conductivity of highly-ordered amorphous and crystalline mesoporous TiO_2 thin films was

measured by 3ω method [118] with porosities of 30% and 35%. The thermal conductivity of crystalline sol-gel mesoporous TiO_2 thin films was about 1.06 W/m·K and comparison was made to show that the connectivity and size of the crystalline domains can provide control over thermal conductivity in addition to porosity.

For experiments that have been undertaken to study the thermophysical properties of TiO_2 thin films, most of them concentrated on the films directly fabricated on substrate by sputtering method or vapor deposition technique. The properties of TiO_2 coating film are proven to be highly related to the physical properties of the substrate, such as the material of substrate, deposition temperature and pressure. Due to its small size, little work has been reported regarding the thermophysical properties of discrete TiO_2 thin film embracing interconnected network of nanowires.

1.1.2 Nanostructure

When dimension of material has been reduced to the level comparable to the characteristic length of the heat transfer carriers, such as mean free path (MFP) and wavelength, the thermophysical property is drastically different from its bulk counterparts because scattering from boundaries and imperfections become predominant in thermal transport process. To understand and characterize the thermal properties of such minuscule structures is essential to microelectronics. By using electron beam and photolithography technique, Majumdar *et al.* [119] fabricated a micro-scale suspended device to measure the

thermal transport property of single multi-wall carbon nanotube (CNT) with known heat flow and temperature gradient in steady state. Similar technique using microfabricated devices [120] was employed to measure thermal and thermoelectric properties of other one-dimensional nanostructures including individual single crystalline intrinsic silicon nanowire [121] and carbon nanofiber [122]. The thermal contacts between sample and microfabricated device was studied and platinum (Pt) deposition was applied to have reduced the contact thermal resistance for about 9-13%. Zhang [123] used thermoreflectance imaging technique to measure the heat transfer along a silicon nanowire suspended between two thin-film heaters and the calculated thermal conductivity of the sample is about 46 W/m·K. When size of wire decreases, the thermal conductivity also decreases. This conclusion is consistent with the theoretical speculation from Yang and Chen [124], who applied a generic model to study the phonon transport and thermal conductivity of simple and tubular nanowire composite and the result show that the effective thermal conductivity changes also with the radius of the nanowires due to the nature of ballistic phonon transport.

In-depth consideration was given to single TiO_2 nanowire in this report after completing the investigation of TiO_2 thin films. Both anatase and rutile-phase TiO_2 Nanowires was successfully fabricated by Xu *et al.* [98] via molten salt-assisted and pyrolysis route. Moreover, TiO_2 mesostructure composed of discrete TiO_2 nanowires were synthesized and studied for their properties and applications. Lei and his group synthesized

highly-ordered TiO_2 nanowire array by a sol-gel method [55]. Those TiO_2 nanowires were examined to be single crystalline anatase with uniform diameter around 60 nm. Mesoporous titania network that consists of anatase TiO_2 nanowires was synthesized to be applied in photocatalysis, photovoltaics and bone-tissue engineering. Boercker [102] studied the growth mechanism of TiO_2 nanowires for Dye-sensitized solar cells. By using a surfactant-assisted "oriented attachment" mechanism [99], TiO_2 nanonetwork that is composed of single crystal anatase nanowires was synthesized and it was approved that the light-to-electricity conversion yield of 9.3% after applying it as TiO_2 thin-film electrode in dye-sensitized solar cells. Although intensive attentions have been devoted to studies of TiO_2 mesostructure of nanowires, few knowledge has been presented concerning the properties of single TiO_2 nanowire. Štengl [101] once prepared and characterized TiO_2 nanowires with diameter around 10 nm by studying their surface area and pore size distribution change with temperature in the range 350 -1000 °C. To be utilized in dye-sensitized solar cells, TiO_2 nanowires were treated with $Nb(Oet)_5$ solutions and it was confirmed in Beppu's work [125] to have high heat resistant properties and even shapes when heated up to 450 °C, which consequently increased the electron diffusion coefficient and photoelectrical conversion efficiency.

Thermophysical properties of single TiO_2 nanowires consequently become our research interest after accomplishing the thermal characterization of anatase thin films. As will be introduced in this report, the TiO_2 thin film synthesized by electrospinning is

observed to be composed of numerous unoriented TiO_2 nanowire and the intrinsic properties and polymorph structure of the nanowire is most assumable to strongly influence the meso-properties of the films. Additionally, as a crucial physical property, density varies substantially with distinct fabrication methodologies; nevertheless it draws little attention when TiO_2 material is extensively studied with different forms and structures.

1.2 Scope of this research

To fulfill proposed concerns and questions, different fabrication techniques are applied in this report for materials of particular structure due their dimensions and composition natures. Electrospinning is adopted to synthesize anatase TiO_2 thin films and also the single anatase TiO_2 nanowires, while spin-coating is applied directed on fabricating the P3HT thin films. The induced interior structure would also be different depending specific fabrication processes. After completing the sample preparation, thermal characterization is performed using diverse techniques, such as transient electrothermal (TET) technique [126], pulse laser-assisted thermal relaxation (PLTR2) technique and calibration of temperature coefficient of resistance. Certain modifications are made to ensure the TET technique and calibration procedure more specifically suitable for the different samples. Other than thermal properties, important physical properties such as density and porosity are also our interest with specific materials. The theoretical principles, analytical solutions and analysis of the thermal characterizations are addressed in Chapter 2 with sample results being presented to confirm the accuracy and efficiency of the

characterization. In Chapter 3 and 4, thin films of around tens micrometers and with different composition natures are fabricated and then characterization are conducted to understand their thermal properties, while the internal structures are distinctly different. In order to understand more about the intrinsic properties of single TiO_2 nanowire that composes the TiO_2 thin film, in Chapter 5, TiO_2 nanowire of about hundreds of nanometers diameters are prepared for further thermal characterization. Regarding the nonlinear effects existed within the measurement, data analysis methods are developed to suppress those effects. Conclusions are made in Chapter 6 to present main findings regarding thermal property of the materials studied and more in-depth analysis will also be presented.

CHAPTER 2. THERMAL CHARACTERIZATION PRINCIPLES AND TECHNIQUES

In this chapter, comprehensive thermal characterization techniques are introduced for understanding the thermal properties of low-dimensional materials. The major properties studied in this report are thermal diffusivity and thermal conductivity, along with some other physical properties such as density and porosity. Depending on the structural natures of the samples, many techniques, such as transient electrothermal (TET) technique, [46, 126] optical heating and electrical thermal sensing (OHTES) technique [127], transient photo-electro-thermal (TPET) [128] technique and pulse laser-assisted thermal relaxation (PLTR) technique [45], have been comprehensively utilized in our group to measure the thermal properties. Laser beam or electrical heating are usually applied in these techniques to provide transient heating. As an essential property to decide how excellent the material conducts thermal energy, thermal conductivity of the materials in this report is determined by combining the TET method with a calibration procedure of the temperature coefficient of resistance, which is performed at quasi-equilibrium process and provides more details about the electro-thermal relationship of the material. Another important thermal property, thermal diffusivity is directly determined by TET technique, which has addressed its competence and excellence in measuring the thermal properties [46, 126].

2.1 Transient electrothermal (TET) technique

Compared with steady state technique, TET presents its advantages on several aspects. First, TET technique can be applied to metallic, nonconductive and semi-conductive one-dimensional small-scale structures including films, wires and tubes, given appropriate coating layers. Second, TET features much stronger signal levels (hundreds to thousands of times higher) compared with 3ω and OHETS techniques. Third, TET technique requires much reduced response time (usually less than one second) and much faster experiment cycle.

2.1.1 Experimental configuration

In TET technique, the to-be-measure sample is suspended between two metal (copper, aluminum, etc.) electrodes as shown in Fig. 2-1. Both ends of the sample are pasted with conductive paint to enhance electrical conduction and attenuate contact thermal resistance. Base with suspended sample as shown in Fig. 2-1 is then positioned in a vacuum chamber ($< 1.0 \times 10^{-3}$ Torr) to minimize the air convection effect. A current source is connected to the base to provide constant current signal, and the rise time of the device is negligible compared with thermal response time of sample. Another high-speed oscilloscope with 1 MΩ impedance is employed to record the real-time voltage-time (*U-t*) response. All connections and cables in the experimental setup are shielded to suppress environmental noise. At the beginning of the experiment, DC current is provided through

the sample to introduce electrical heating. Induced temperature evolution of the wire strongly depends on the heat transfer along it and consequent temperature rise leads resistance change, which is converted to the voltage change recorded by oscilloscope. A typical *U-t* profile of platinum (Pt) wire is presented in Fig. 2-2. It is observed in this plot that the voltage is zero before the current is provided and then immediately rises to a non-zero anticipated value as soon as the current feeding is turned on. Under continuous constant current, the voltage recording on the oscilloscope increases and then reaches a stable value if cycle time is long enough. Particularly, for rise state, only very few irrelevant points emerge before reaching the anticipated voltage, indicating that the voltage response is linear and no substantial impacts to reduce the current passing through the Pt wire. At the moment when the current feeding is terminated, the voltage instantaneously decreases to zero value with only very few intermediate points, as well implying that mostly only the resistance of Pt wire takes effect. If the to-be-measured sample is nonconductive, a thin film of metal is coated on the surface of the wire to make it electrically conductive.

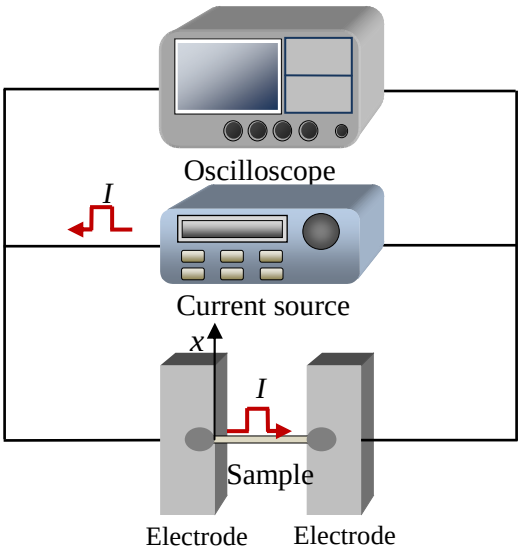

Figure 2-1. Experimental configuration of transient electrothermal technique.

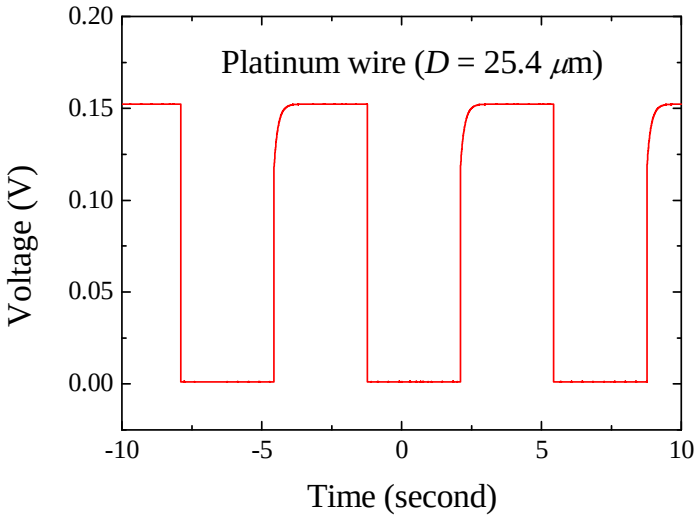

Figure 2-2. Voltage-time (*U-t*) response profiles of a platinum wire via the TET measurement.

2.1.2 Theoretical principles

In order to derive the thermal diffusivity from a *U-t* profile as shown in Fig. 2-2, theoretical solution to relate the temperature variation with the voltage change is required for data fitting purpose. The experimental setup can be interpreted as a one-dimensional heat transfer problem if the length of the sample is long enough compared with the diameter. The electrical heating power may change a little with time and is assumed to be constant in this experiment. The initial condition of the problem is $T(x, t = 0) = T_0$, where T_0 is the room temperature. Since the dimension of the electrode is much larger than the sample dimension, the temperature of the electrode can be assumed to be constant during the whole measurement. Therefore, the boundary conditions are reasonably described as $T(x = 0, t) = T(x = L, t) = T_0$. For the heat transfer along the x-directional and if the thermal radiation is neglected, governing equation is as follows,

$$\frac{\partial\left(\rho c_p T\right)}{\partial t} = k\frac{\partial^2 T}{\partial x^2} + q_0, \tag{1}$$

where ρ, c_p and k are density, specific heat and thermal conductivity of the sample, respectively. For analysis purpose, these properties are assumed constant and independent of temperature. Details for solving this equation are given in the work from another colleague [126]. Analytical solution is solved using Green's function,

$$G_{X11}\left(x,t\middle|x',\tau\right) = \frac{2}{L}\sum_{m=1}^{\infty} exp\left[-m^2\pi^2\alpha\left(t-\tau\right)/L^2\right]\times\sin\left(m\pi\frac{x}{L}\right)\sin\left(m\pi\frac{x'}{L}\right). \tag{2}$$

The temperature distribution along the length direction is then expressed as

$T(x,t) = T_0 + \frac{\alpha}{k}\int_{\tau=0}^{t}\int_{x'=0}^{L} q_0 G_{X11} dx' d\tau$. The average temperature of the sample $T(t)$ is then obtained by integrating $T(x, t)$ over the whole length,

$$T(t) = \frac{1}{L}\int_{x=0}^{L} T(x,t)\,dx = T_0 + \frac{8q_0L^2}{k\pi^4}\sum_{m=1}^{\infty}\frac{1-exp\left[-(2m-1)^2\pi^2\alpha t/L^2\right]}{(2m-1)^4}. \quad (3)$$

With enough thermal transport time, the temperature distribution along the sample reaches steady state and is $T_0 + q_0L^2/(12k)$ based on Eq. (3). q_0 is the electrical heating power per unit volume and is expressed as $q_0 = I^2R/(AL)$, in which A and L are cross-sectional area and length of the sample, respectively. Normalization of average temperature increase into dimensionless form presents

$$T^* = \frac{96}{\pi^4}\sum_{m=1}^{\infty}\frac{1-exp\left[-(2m-1)^2\pi^2\alpha t/L^2\right]}{(2m-1)^4}. \quad (4)$$

The voltage evolution (U_{sample}) recorded by the oscilloscope is directly related to the average temperature change of the sample as

$$U_{sample} = IR_0 + I\eta\frac{8q_0L^2}{k\pi^4}\times\sum_{m=1}^{\infty}\frac{1-exp\left[-(2m-1)^2\pi^2\alpha t/L^2\right]}{(2m-1)^4}, \quad (5)$$

where U_{sample} is the voltage over the sample recorded by the oscilloscope, I is the constant current fed through the sample, R_0 is the resistance of sample without heating, and η is the temperature coefficient of resistance of the sample. One typical profile based on Eq. (5) is

seen in Fig. 2-3 and it is obvious that the recorded voltage change is inherently analogous to the temperature evolution of the sample as seen in Fig. 2-2. The methodology how to derive the thermal properties from the U-t profile is also interpreted in this figure. For each *U-t* response profile, a transient voltage rise state appears as soon as the current starts to feed and this transient state is analogous to temperature change shown in Eq. (4). In order to obtain the thermal diffusivity, global fitting of the experimental data to theoretical solution is performed by trying different trial values of thermal diffusivity and the best fit (least square) gives that thermal property of the measured sample.

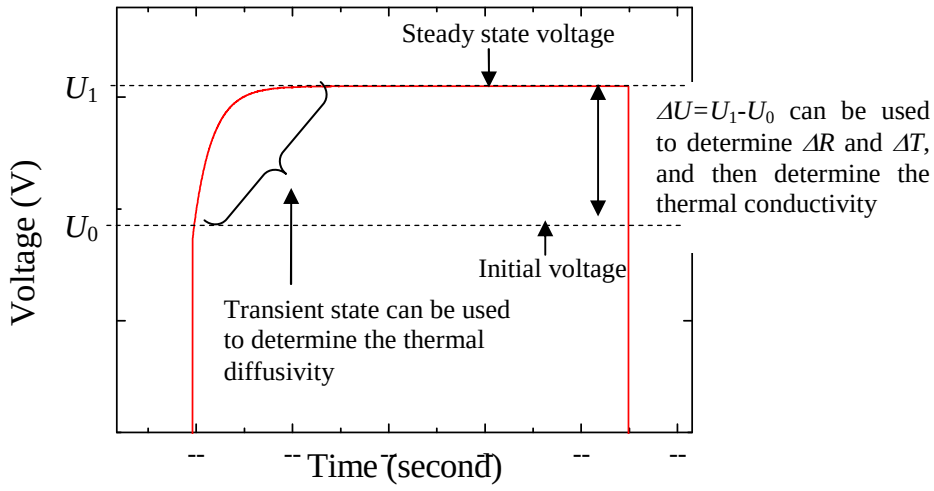

Figure 2-3. Methodology to determine the thermophysical properties based on the experimental *U-t* profile.

2.2 Temperature coefficient of resistance calibration

From Eq. (4), if time is long enough, the temperature distribution along the sample reaches the steady state and the average temperature of the wire becomes $T_{stable} = T_0 + q_0 L^2 / (12k)$. q_0 is the electrical heating power per unit volume and can be expressed as $q_0 = I^2 R / (AL)$, while the A and L are the cross-sectional area and length of the sample, respectively. This steady state is also observed in Fig. 2-3. When temperature distribution reaches steady, the resistance remains constant and the voltage does not change any more. Therefore, the temperature variance $\Delta T = T_{stable} - T_0 = q_0 L^2 / (12k)$ is obtained. With the calibration result of temperature coefficient of resistance η and the resistance change ΔR during the heating process, the temperature change ΔT is calculated and then the thermal conductivity is obtained as $k = I^2 RL / (12A\Delta T)$.

The calibration procedure is performed immediately before or after the TET measurement is finished, and the temperature range normally covers the temperature varying range in TET experiment. Therefore the experimental setup of calibration procedure is very similar to the TET setup and the experimental base is still the one shown in Fig. 2-1. Instead of using the constant current source and oscilloscope, DC power supply is connected to provide heating source while the temperature and resistance change are recorded by thermocouple meter and digital multi-meter, respectively. During the calibration procedure, the coated sample is suspended between two conductive electrodes

by silver paste. Thermocouple is attached to one side of the electrode, close enough to the sample, and the other end of the thermocouple is connected to a thermocouple meter to simultaneously monitor the temperature change. The whole stage including the electrodes and the sample suspended between the electrodes is situated on a heating plate. This calibration procedure is conducted also in a vacuum chamber whose pressure is kept lower than 10^{-3} Torr to reduce unnecessary heat dissipation. The heating power is precisely controlled to maintain the process moderate. After the temperature reaches the speculated temperature value, the heating is turned off and the cooling process begins. During the cooling process, temperature decrease is relatively slow compared to the heating process. Therefore the time can be assumed to be long enough to achieve even temperature distribution and the readings from the thermocouple meter can be approximated as the temperature of the sample. Both temperature and resistance readings are recorded to attain the temperature-resistance calibration profile for further data processing.

2.3 Modification process to derive real thermal properties

Not all materials measured are excellent electrical conductive, therefore, in order to enhance the electrical conducting behavior, a metallic thin film is coated over the nanowire surface. This metallic coating ensures the sample to rapidly conduct electrical current and generate heat which transfers along the axial direction such that the thermal properties can be measured. When the heat flows in the coating layer and materials are both along the axial direction, the effective thermal conductivity of the whole sample can be expressed as

$$k_{eff} = \frac{k_s A_s + k_f A_f}{A_s + A_f}, \tag{6}$$

where k is thermal conductivity and A the cross sectional area, while subscripts s and f indicate bare low-dimensional sample and the coated iridium film, respectively. To simplify the equation an assumption is made that the cross-sectional area of bare sample is much greater than that of the iridium film, which implies $A_s > A_f$. Meanwhile, according to the definition of Lorenz number, k_f is expressed as

$$k_f = \frac{L_{Lorenz} TL}{RA_f}, \tag{7}$$

Combine Eq. (6) and Eq. (7), we can determine the real thermal conductivity of bare TiO_2 nanowire as

$$k_s = k_{eff} - \frac{L_{Lorenz} TL}{RA_s}, \tag{8}$$

The Lorenz number for different metallic film varies slightly and it also is relevant to temperature. For example, the Lorenz number for gold is 2.35×10^{-8} W·Ω/K^2 at 0 °C and 2.40×10^{-8} W·Ω/K^2 at 100 °C [129], which is seen to have only weak variation within the normal temperature range in the measurements and is usually treated as a constant within the temperature range in TET experiment [130]. However, due to the fact the thickness of gold films are usually around tens of nanometers, the Lorenz number is estimated to be

significantly different from the value of bulk materials, 2.4×10^{-8} W·Ω/K^2. Research is now in progress to understand the dependence of Lorenz number on film thickness. Therefore in this work, Lorenz number is usually taken a larger value than 2.4×10^{-8} W·Ω/K^2. Specific value of Lorenz number is dependent on the film thickness and also the material of the film. Using temperature and resistance at steady state, the real thermal conductivity of sample is determined based on Eq. (8), and the portion of contribution from the metallic coating is also known. Same strategy is also applied to calculate the real thermal diffusivity of the sample after the effective volume-based specific heat is obtained as $C_{eff} = \rho c_p = k_{eff} / a_{eff}$. Then the real thermal diffusivity is expressed as

$$\alpha_s = \alpha_{eff} - \frac{L_{Lorenz} TL}{RA_s C_{eff}}, \tag{9}$$

With known real thermal conductivity and thermal diffusivity, if the specific heat can be specified with the measured sample, the real density of the material is then derived precisely. Mostly due to nature of different fabrication techniques, the density of synthesized materials is differently from its bulk value, slightly or sometimes significantly. For this reason, to accurately determine the density of the materials bears substantial importance, for understanding the principles of small-scale thermal transport phenomenon.

Radiation heat transfer from the film surface may be an important issue to be considered in this work. For radiation heat transfer from film surface, it can be

approximated by $q_{rad}=\varepsilon\sigma A[(T_0+\Delta T)^4-T_0^4]$, where ΔT is the average temperature rise over the sample, ε is the surface emissivity, σ the Stefan-Boltzmann constant, A is the effective surface area for radiation heat transfer (equals to $2(W+D)\cdot L$). Meanwhile, from the expression to calculation thermal conductivity in TET technique, the heat generation is estimated as $q_{gen}=V12k\Delta T/L^2$, in which the V is the volume of sample and expressed as $W\cdot D\cdot L$. This radiation and heat generation estimation is for the steady state of the thin film with a uniform heat generation inside. Although a simple ratio between the radiation heat flow and heat generation cannot precisely represent the experimental case, it provides a sound first-order approximation of the radiation effect. The ratio of radiation to overall heat generation is estimated as,

$$\frac{q_{rad}}{q_{gen}}=\frac{\varepsilon\sigma\cdot 2(W+D)L\cdot\left(4T_0^3\Delta T+6T_0^2\Delta T^2+4T_0\Delta T^3+\Delta T^4\right)}{\frac{WDL\cdot 12k\Delta T}{L^2}} \quad (\Delta T = T_0, D = W)$$

$$\approx\frac{2\varepsilon\sigma T_0^3 L^2}{3kD} \quad (10)$$

This ratio is derived based on assumption that $\Delta T << T_0$ and thickness of film is small enough compared to other two dimensions. At transient state, the ratio is even smaller due to gradually increasing temperature. For instance, for an arbitrary P3HT thin film, it is estimated that the ratio is even less than 1%, by varying the length from 2mm to 4mm. In conclusion, the radiation heat transfer in this model is negligible compared to the heat conduction along the sample, if the geometry of sample is accordingly controlled.

2.4 Pulsed laser assisted thermal relaxation 2 (PLTR2) technique

As discussed in previous section, TET technique uses a step DC current as thermal excitation to induce temperature rise. Upon heating, it will take a certain time to reach the steady state. This time it takes is strongly dependent on the thermophysical properties and geometry of to-be-measured samples. However, limited by the slow rise time of the current source (~2 μs), it is hard to implement TET on short sample or along thickness direction. Therefore PLTR2 technique is developed to overcome the drawbacks of TET technique to characterize thermal transport along short samples.

2.4.1 Experiment setup of PLTR2

Different from TET technique, PLTR2 [45] is a laser-based technique that is capable to simultaneously determine thermal properties along both in-plane and cross-plane from a single measurement. This technique originates from flash technique and a distinct difference is that, instead of using infrared detector to probe temperature rise on back surface, constant electricity is always fed through the film to sense the resistance change. Because of the enhancement of electrical conduction in P3HT film, resistance change is used to depict temperature change and consequent to determine the thermal property. A schematic of PLTR2 is shown in Fig. 2-4. This sketch about experimental setup of PLTR2 technique is not scaled. Using proper coatings, the PLTR2 technique can be used to metallic,

nonconductive and semiconductive micro- and nanoscale materials. In Fig. 2-4, a coating configuration is presented to demonstrate how a semi-/nonconductive materials is characterized using PLTR2.

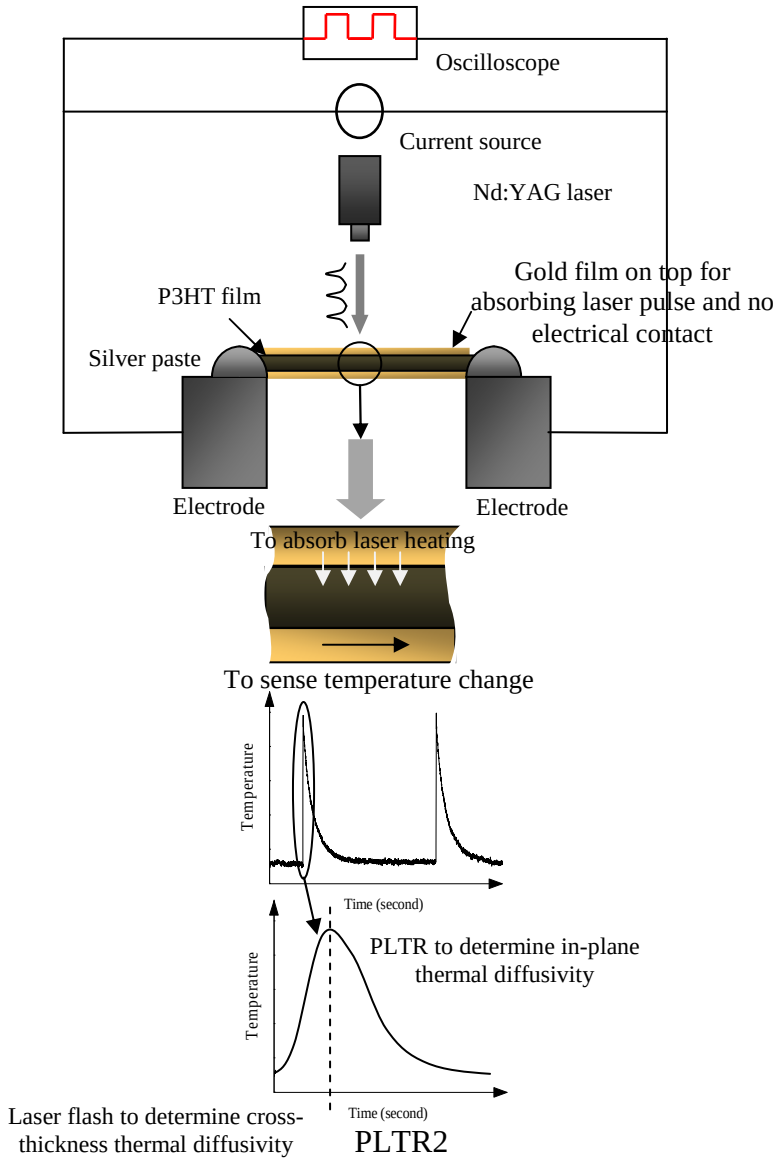

Figure 2-4. Experimental principle for applying TET and PLTR2 techniques to characterize 3-dimensional anisotropic thermal transport in P3HT microfilm.

As seen in Fig. 2-4, experimental setup of PLTR2 is analogous to TET, except that PLTR2 utilizes a pulsed laser for thermal excitation purpose. In the whole experiment, a small amount of DC current is fed through the sample to probe the temperature change and an ultrafast oscilloscope is applied to record the consequent voltage variation with time, as shown in Fig. 2-4. Usually, gold coating is applied to enhance the electrical conduction is the sample does not embrace strong metallic characteristics. Different from TET technique, both sides of the sample need to be coated and coating on each side fulfills different purposes. The gold film on top surface is for absorption of laser beam. Absorbed laser energy excites the electrons in neighboring thin layers. Due to the relatively small electronic heat capacity, the electron temperature increases soon and then hot electrons interact with lattice in the gold layer through scattering, causing the temperature of the whole gold layer to rise immediately. The absorbed energy then transfers from gold layer to underlying P3HT film through phonon-phonon scattering. This vertical thermal transport process happens in extremely fast manner such as a few hundred of microseconds. After the whole sample reaches uniform temperature, thermal energy will be dissipated to surroundings via the contact with electrodes and heat transfer along the length direction will be a much slower process compared with the temperature rise vertically.

2.4.2 Physical model of PLTR2 technique

It is distinctly observed in Fig. 2-4 that every signal from PLTR2 measurement comprises two states. For the instantaneous vertical temperature increase, Parker analytically analyzed it in flash technique [131] and the thermal diffusivity is expressed as,

$$\alpha = 1.38D^2 / \pi^2 t_{1/2} \ , \tag{11}$$

where the $t_{1/2}$ is the time required to reach half of the maximum temperature rise and D is the thickness of P3HT thin film.

The vertical thermal transport is followed by a relatively slow heat transfer along length direction due to the dissipation of thermal energy to surroundings. Because the length of thin film is significantly greater than then thickness, the physical model is simplified to be one dimension (in the length direction of the film). One-dimensional heat diffusion equation is then used to describe the thermal relaxation,

$$\frac{\partial(\rho c_p T)}{\partial t} = k\frac{\partial^2 T}{\partial x^2} + q_0, \qquad q_0 = \begin{cases} s, & 0 \le t \le \Delta t \\ 0, & t > \Delta t \end{cases} \ , \tag{12}$$

where the q_0 includes both joule heating and laser pulse heating. Because the joule heating introduced by a constant DC current contributes only steady temperature distribution during the whole process, only laser pulse heating is considered here. Δt is the laser pulse width and the laser intensity is assumed to be constant during Δt (~ 7 ns). This laser heating time is drastically smaller than characteristic time of heat diffusion in sample. This equation can be solved using Green's function and more details can refer to another work in our group.

Only analytical solution is presented here for analyze. Integration of the solution $T(x, t)$ along the length direction gives the temporal temperature variation and it is then normalized to be,

$$\bar{T}(t) = \frac{1}{L}\int_{x=0}^{L} T(x,t)dx$$
$$= \begin{cases} \dfrac{8sL^2}{k\pi^4}\displaystyle\sum_{m=1}^{\infty}\dfrac{1-exp\left[-(2m-1)^2\pi^2\alpha t/L^2\right]}{(2m-1)^4} & (0 < t \le \Delta t) \\ \dfrac{8sL^2}{k\pi^4}\displaystyle\sum_{m=1}^{\infty}\dfrac{exp\left[-(2m-1)^2\pi^2\alpha t/L^2\right]\left\{exp\left[(2m-1)^2\pi^2\alpha\Delta t/L^2\right]-1\right\}}{(2m-1)^4} & (t > \Delta t) \end{cases} \quad (13)$$

Since only temperature decay after laser heating is the process that we are interested in, the solution for time larger than Δt is considered and is then normalized as $T^* = \left[\bar{T}(t) - \bar{T}_{\min}\right] / \left[\bar{T}_{\max} - \bar{T}_{\min}\right]$. Here $\bar{T}_{\min}$ is 0 and $\bar{T}_{\max}$ is the maximum temperature rise of the sample. During the laser irradiation, the heat transfer in sample's length direction is neglected because the ultrafast time scale. Therefore $\bar{T}_{\max}$ is calculated as $q_0\Delta t / \rho c_P$ based on the energy conservation. Then the normalized temperature relaxation can be written as

$$T^* = \frac{8L^2}{\alpha\Delta t\pi^4}\sum_{m=1}^{\infty}\frac{exp\left[-(2m-1)^2\pi^2\alpha t/L^2\right]\left\{\exp\left[(2m-1)^2\pi^2\alpha\Delta t/L^2\right]-1\right\}}{(2m-1)^4} \quad . \quad (14)$$

Since the pulse time Δt is only a few nanoseconds, $\exp\left[\left(2m-1\right)^2 \pi^2 \alpha \Delta t / L^2\right]$ is simplified as $1+\left(2m-1\right)^2 \pi^2 \alpha \Delta t / L^2$ using Taylor expansions. Further convergence study is carried out and proves that when Δt is small, the term of $(2m\text{-}1)^2$ is small enough by taking m as 15. Therefore further simplifications are made to Eq. (14) give a temporal temperature distribution for the thermal relaxation process,

$$T^* = \frac{8}{\pi^2} \sum_{m=1}^{\infty} \frac{exp\left[-\left(2m-1\right)^2 \pi^2 \alpha t / L^2\right]}{\left(2m-1\right)^2} \quad . \tag{15}$$

This equation demonstrates that for any material with arbitrary length, normalized temperature relaxation follows the same profile with respect to the Fourier number ($Fo = \alpha t/L^2$). Fitting method is applied to vary the thermal diffusivity to obtain the best value which gives minimum difference. In practice, the laser beam has Gaussian distribution in space. To suppress the spatial non-uniformity of the laser beam, the beam spot is chosen to be larger than the length of film, ensuring that laser intensity distribution over the sample is uniform.

CHAPTER 3. THERMAL TRANSPORT IN ORGANIC MICRO-FILMS

In this chapter, thermal properties and porosity of micro-scale thin films will be investigated using TET technique with calibration of the temperature coefficient of resistance. The materials introduced in this chapter include two different kinds: inorganic semi-conductive anatase titanium dioxide (TiO_2) thin film and organic conductive Poly(3-hexylthiophene) (P3HT) thin film. Different fabrication techniques induce different interior structures and consequently cause distinct thermophysical properties. This chapter will focus on organic P3HT thin films while the anatase TiO_2 thin film is introduced in next chapter. Section 3.1 and 3.2 focuses on P3HT film, including sample preparation, relevant experimental details of the TET technique and the calibration, measured results and discussions. In section 3.3, P3HT thin films are investigated and the relationship between the interior structure and thermophysical properties are presented. Additionally, section 3.4 discussed about the anisotropy in thermal property of spin-coated P3HT film and PLTR2 technique is applied to study the anisotropic thermal properties, showing that anisotropic factor is large than 1 and partial orientation caused by the spin coating process exists within the polymer thin films.

3.1 Sample preparation

Regioregular P3HT (average molecular weight = 50,000 MW) was purchased from Rieke Metals and anhydrous chloroform is obtained from Sigma Aldrich. As-purchased

compounds are used without further processing. Preparation of P3HT solution was conducted in an argon glove compartment and the solution is then magnetically stirred in a capped vial for 1 hour, with auxiliary heating up to 50 °C to help dissolve. The P3HT thin film was prepared in air by spin-coating at 5000 rpm for 45 s in a Pyrex glass dish. Thickness of the P3HT thin film may slightly vary from spot to spot because the bottom of the dish is not absolutely flat. Although P3HT is a conductive polymer material, the relatively poor electrical conductivity is not sufficient for acquiring strong signal in our thermal characterization experiment. Therefore after the P3HT thin film was removed from the dish, it was coated with an ultra-thin gold layer for enhancing electric current conducting and thermal sensing purpose. The coating procedure was done using a Denton vacuum sputtering device and continued for 100 s, which is estimated to generate a gold coating of 50 nm thickness. Further discussion will be given later to examine the influence of the gold coating on thermophysical properties measurement later. In order to identity the crystal structure of the P3HT thin film, A Voyage confocal Raman spectroscopy was used and a comparison of typical Raman spectrums of the prepared P3HT thin films is presented in Fig. 3-1, with excitation laser of 532 nm wavelength, 0.2 mW power and $3\times10\ \mu m^2$ spot size. A scan time of 30 s is chosen for all samples and the orientations of samples are all perpendicular to the laser. It can be observed that for P3HT films fabricated from solutions of different P3HT weight percentages, the Raman spectra follow similar distributions and the characteristic bands are distinctly observed for every P3HT thin film, while the intensity varies with P3HT solution weight percentage. Among all spectra, the band with a maximum

value around 1448 cm^{-1} is related to the $C_\alpha = C_\beta$ bond of the thiophene ring, while the other peak around 1382 cm^{-1} represents the $C_\alpha - C_\beta$ bond stretching [132]. Exact value of the peaks for different films may be moderately different but close enough. Under identical integration time higher P3HT solution weight percentage gives sharper and more distinct peaks. For the Raman spectrum peak height, it is proportional to $[1-\exp(-2z_0/\tau)]$ where z_0 is the film thickness and τ the optical absorption depth. τ is proportional to the inverse of film density (ρ). As discussed later (Fig. 3-4), when the P3HT solution weight percentage is higher during fabrication, the fabricated film is thicker and has a higher density. This explains why the higher P3HT solution weight percentage in fabrication gives higher Raman peak intensity.

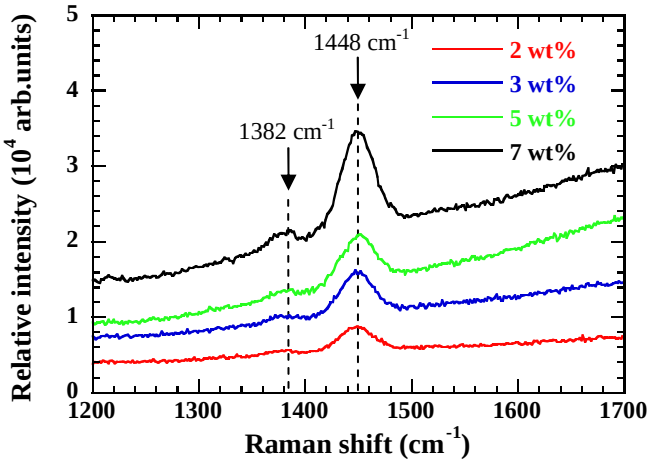

Figure 3-1. Comparison of Raman spectrum of P3HT thin films fabricated with different P3HT solution weight percentages.

3.2 Experiment procedures

For Au-coated P3HT thin films, the electrical conductance and thermal conductance are significantly enhanced compared with bare samples. Calibration procedure is conducted before the TET measurement to determine the temperature coefficient of resistance for the P3HT thin films. As discussed before, the Au-coated P3HT thin film was suspended between two aluminum electrodes by silver paste and a *K*-type thermocouple was attached to measure the temperature change of the P3HT thin film. Although the thermocouple is pasted to the electrode surface, an assumption is made that the temperature readings represent the P3HT thin film's temperature since the film is in excellent contact with the electrode surface using the silver paste. The calibration procedure was conducted in the vacuum chamber the pressure in which is kept lower than 10^{-3} Torr to reduce unnecessary heat convection to air. During the calibration, a DC voltage of about 44 V was engaged for the heater placed under the stage and the temperature variation during calibration is controlled between 25 °C and 60 °C to avoid potential damage to the P3HT thin film. Temperature and resistance readings during the cooling phase were collected because in the cooling phase there is no heat generation in the heater and the heat transfer is relatively slow compared to the heating process. Therefore the collected temperature can be assumed the evenly-distributed temperature of the suspended P3HT thin film.

After the calibration procedure is completed, TET experiment setup was performed after the temperature-resistance calibration procedure. During the TET experiment, a step

DC current of about a few mA (I) was fed through the P3HT thin film to generate electrical heat. Transient temperature increase of the P3HT thin film is strongly dependent on the heat transfer within the film and it then leads to resistance change and induces an overall voltage change. The voltage change of P3HT thin film under the fed DC current was collected by an oscilloscope. Details about TET technique are introduced in Chapter 2 and a sample profile is also given in Fig. 2-2.

3.3 Results and discussions

3.3.1 TET measurement of thermal conductivity and thermal diffusivity

All prepared P3HT thin films are about 20-50 μm thick. The thickness measurement has about 10% uncertainty and its impact on the final results will be discussed later. In this section, a selected P3HT thin film is chosen to demonstrate the experiment and post-processing procedure. All details of this film are listed in Table 3-1 while a microscopic image is presented in Fig. 3-2(a) to show its real dimensions during the measurement.

Table 3-1. Details of the experimental parameters and results for a selected P3HT thin film characterized by using the TET technique.

Length (mm)	3.66
Width (mm)	0.29
Thickness (μm)	33.0
Resistance (Ω)	34.0
DC current (mA)	6.00
Weight percentage (wt%)	3.00
Effective density (kg/m^3)	1200
Measured thermal diffusivity ($\times 10^{-7}$ m^2/s)	8.06
Real thermal diffusivity ($\times 10^{-7}$ m^2/s)	7.64
Effective thermal conductivity (W/m·K)	1.57
Real thermal conductivity (W/m·K)	1.48

As discussed in Guo's work [126], theoretical fitting of the normalized experimental temperature rise (Eq. (4)) is conducted by using different trial values of the thermal diffusivity of the sample. The value giving the best fit of the experimental data is taken as the property of the film. Fitting of the experimental data for this film is illustrated in Fig. 3-2(b) and the thermal diffusivity is determined at 8.06×10^{-7} m^2/s, which still includes the influence of the gold coating layer. Based on Eq. (9), both the density and specific heat of this material are required to evaluate this influence. Calorimetric measurements revealed that for regioregular P3HT an endothermic transition from a crystalline to a liquid crystalline state occurs at 210-225 °C [15]. However, because of the low temperature range during our experiment, the endothermic transition is not considered and the specific heat is

around 1550~1620 J/kg·K, depending on the specific temperature of the P3HT film [15].

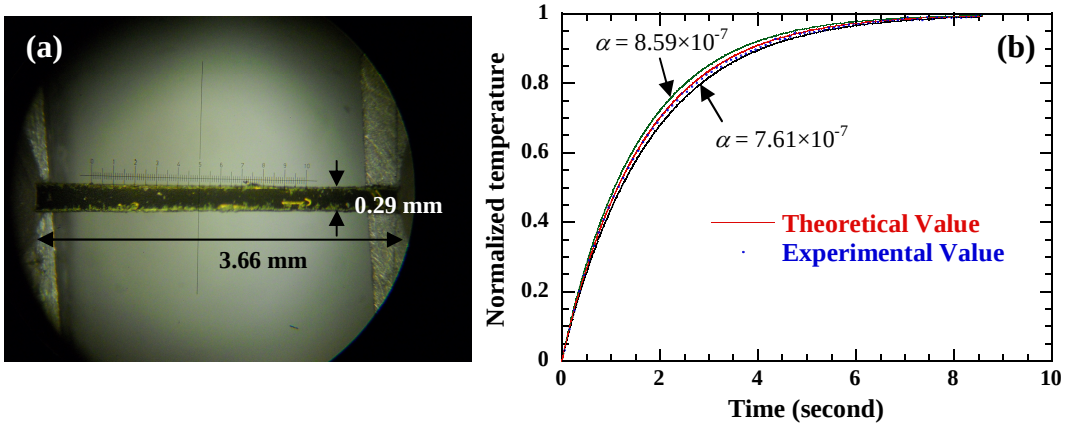

Figure 3-2. (a) Microscopic image of the selected P3HT thin film listed in Table 3-1, and (b) comparison between the theoretical fitting and experimental data for the normalized temperature rise versus time.

According to Erwin's work [14], the density of P3HT thin film can be derived based on film thickness and the molecular weight of a P3HT monomer and the average value of density for P3HT thin film is determined at 1.33±0.07 g/cm^3 by measuring the thickness and combining the Rutherford backscattering spectroscopy data. Nevertheless, in this work the density of every P3HT thin film is individually estimated using obtained thermal conductivity, thermal diffusivity and specific heat based on the definition of the thermal diffusivity, $\alpha = k/\rho c_p$. The thermal conductivity of the P3HT thin film is calculated from the calibration procedure of temperature coefficient of resistance η. As analyzed before, the heating and temperature range are moderate to assure the P3HT thin film is intact, and a typical calibration profile of the P3HT thin film in Table 3-1 is displayed in Fig. 3-3. A distinct linear temperature-resistance relationship similar to an excellent conductor is

presented and linear fitting is used to obtain the temperature coefficient of resistance, which is 3.04×10^{-2} Ω/K for this P3HT thin film. With 6 mA DC current passing through this film, the resistance change is calculated to be 0.76 Ω and the consequent temperature change is 25.1 K, which is in the expected temperature variation range and assures the P3HT thin film undamaged during the experiment procedure. The thermal conductivity is derived based on previous expression as 1.57 W/m·K. Then the effective density of the P3HT thin film in Table 3-1 is calculated to be 1200 kg/m^3, which is close to the literature value considering the measurement uncertainty.

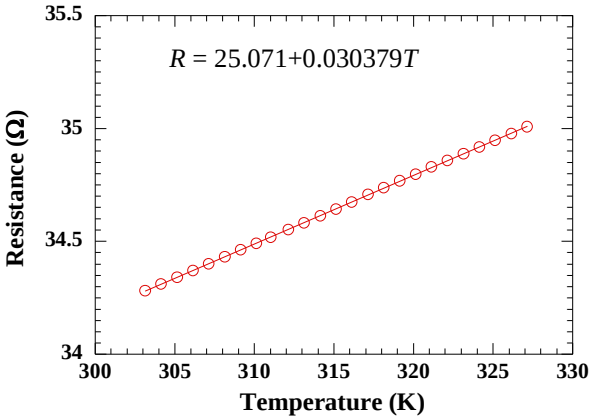

Figure 3-3. Linear fitting curve of temperature coefficient of resistance for the P3HT film in Table 3-1.

The thermal diffusivity and thermal conductivity for calculating the density are both effective values that include the effect of gold coatings. In order to rule out the impact, modification is performed with known dimensional parameters and physical properties. The real thermal diffusivity is 7.64×10^{-7} m^2/s and the real thermal conductivity is 1.48 W/m·K based on Eq. (9) and (8), implying that the impact of gold coating is small (around 5%).

The obtained thermal conductivity is higher than typical value for polymer material that is less than 1 W/m·K.

3.3.2 Thermophysical properties of P3HT thin films with different dimensions

Table 3-2. Experimental data and results of all P3HT thin films

#	Length (mm)	Width (mm)	Thickness (μm)	%	I (mA)	$\Delta R/\Delta T$ (Ω/K)	ρ (kg/m^3)	α ($\times 10^{-7}$ m^2/s)	k (W/m·K)
1	2.60	0.23	26.0	2.0	6.0	0.019	878	9.00	1.29
2	2.65	0.43	22.0	2.0	8.0	0.018	1030	8.79	1.45
3	3.24	0.29	18.0	3.0	5.0	0.023	935	10.3	1.55
4	3.66	0.29	33.0	3.0	6.0	0.030	1200	7.64	1.48
5	3.05	0.50	35.0	5.0	5.0	0.062	1590	6.14	1.57
6	2.98	0.39	39.0	5.0	5.0	0.062	1640	6.33	1.67
7	3.32	0.42	31.0	7.0	8.0	0.025	1470	6.79	1.59
8	2.14	0.32	52.0	7.0	15.	0.008	1570	5.75	1.44

P3HT thin films fabricated from solutions of different P3HT weight percentages are measured to explore the relationship between the weight percentage and thermophysical properties. However, even though under the same weight percentage, the internal structure of fabricated samples may still have slight difference and therefore the measured data from the same weight percentage are treated separately instead of exploring the average values.

The obtained data still demonstrate certain trend when minor deviations exist within the data from the same weight percentages. Detailed information about all P3HT thin films is listed in Table 3-2, along with the real thermophysical properties and effective density. The thermal conductivity and diffusivity in Table 3-2 are the values exclusive of gold coating effect. Because of different P3HT solution weight percentages, the densities of spin-coated P3HT thin films are different, varying from 878 to 1640 kg/m^3 while the literature value is around 1330 kg/m^3 [14]. This variation is supported by the Raman spectra shown in Fig. 3-1 in which it can be seen that higher P3HT solution weight percentage contributes to more distinct band. When the weight percentage increases from 2 wt% to 7 wt%, the average density of all P3HT thin films at each weight percentage increases from 954 kg/m^3 to 1520 kg/m^3. Higher weight percentage gives higher density when the values around 7 wt% have deviations which may be attributed to the uncertainty introduced by thermal conductivity measurement. The thickness is also believed to be impacted by the P3HT solution weight percentage. When it changes as 2, 3, 5 and 7 wt%, the average thickness of P3HT thin films at each solution weight percentage is measured at 24, 26, 37 and 42 μm, respectively. The flatness of the film surface varies from spot to spot because of the quick spin-coating process and different weight percentages. Surface flatness is an important factor to import errors into the thickness measurement, which consequently impact the measured thermal properties. When preparing the P3HT solution, higher weight percentage gives higher viscosity of the solution. Therefore during the spin-coating procedure, thicker film is fabricated with higher viscosity. Detailed relation between the thickness, density and the

P3HT weight percentage during fabrication is illustrated in Fig. 3-4.

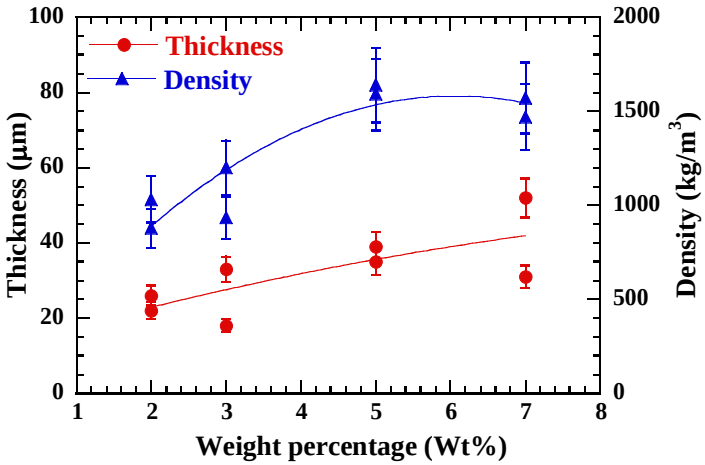

Figure 3-4. Thickness and density of P3HT thin films versus the P3HT solution weight percentage, and the curves are used to guide eyes to view the data trend.

Figure 3-5(a) shows the variation of thermal conductivity and thermal diffusivity versus the P3HT solution weight percentage. For thermal conductivity, it shows insignificant change but only slight vibration around 1.5 W/m·K with average deviation less than 15%. Therefore considering the measurement uncertainty, this deviation is not distinct and the P3HT solution weight percentages can be concluded to have little influence on the thermal conductivity. On the other hand, the thermal diffusivity shows significant impact from the P3HT solution weight percentages. When weight percentage ascends from 2 wt% to 7 wt%, the thermal diffusivity descends from 8.90×10^{-7} to 6.27×10^{-7} m^2/s. This decrease of the thermal diffusivity is mostly induced by the density increase as shown in Fig. 3-4. An X-ray diffraction (XRD) analysis performed with Siemens D500 is presented in Fig. 3-5(b). 3 peaks are observed at 5.4, 10.8 and 16.3 °. From the separation of each peak, it can be

identified that the three peaks represent three parallel crystal planes, each of which can be reasonably assigned to (001), (002) and (003) plane, respectively. A single spacing separation is calculated to be 16.4 Å [133] from XRD data. The XRD of all P3HT thin films indicates that with different P3HT solution weight percentages the XRD profiles follow same peak values and plane separations. It means the crystal structure of all P3HT thin films fabricated from P3HT solution of different weight percentages does not demonstrate distinct difference.

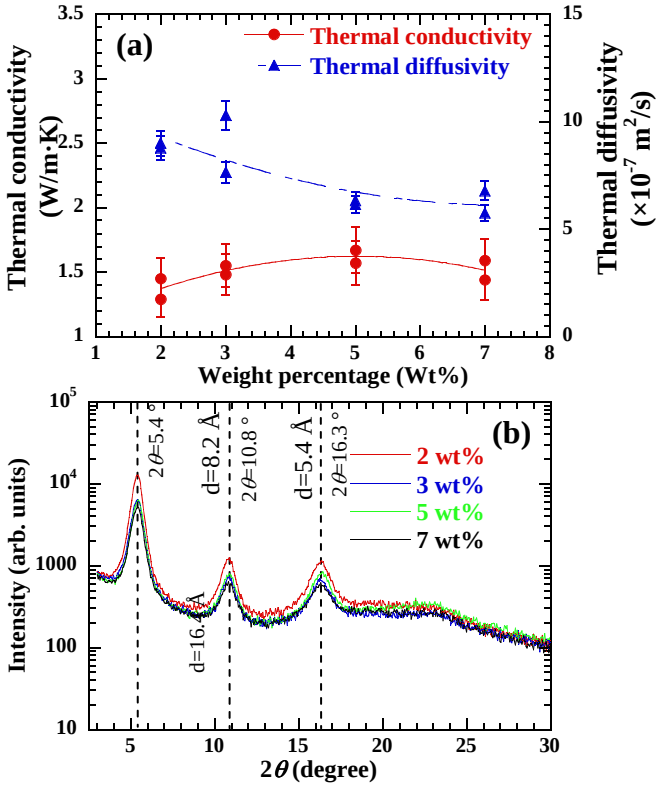

Figure 3-5. (a) thermal conductivity and thermal diffusivity of P3HT thin films versus the P3HT solution weight percentage. The curves are to guide the view of data trend. (b) XRD graph of P3HT thin films fabricated from solutions of different weight.

In Figure 3-6 the relationships between density and thermal diffusivity and thermal conductivity are presented. Because the structure of fabricated P3HT films embraces loose nature, density may vary distinctly dependent on the fabrication conditions and it becomes an important physical property of P3HT. Compared with the P3HT solution weight percentage, the density proves to be a better parameter to study the variation of thermal conductivity and thermal diffusivity. The thermal conductivity slightly increases from 1.29 W/m·K to 1.67 W/m·K with density increase. The variation range of thermal conductivity is about 30% within the density scope. Although the impact of density on the thermal diffusivity is also not strong, the thermal diffusivity shows contrary influence from density when it decreases from 1.03×10^{-6} to 5.75×10^{-7} m^2/s with little deviation. It can be concluded that although density affects both thermophysical properties, the tendencies are different. Thermal conductivity only relies on the amount of phonons and the scattering process inside the material. Undoubtedly with similar crystal structures higher density means less cavity and higher thermal conductivity. On the other hand, the thermal diffusivity is a ratio of the material's ability to conduct thermal energy over the capability to store thermal energy. The effect of density on storing energy is more than that on increasing thermal conductivity. The comprehensive effect is that the thermal diffusivity decreases with increasing density, which is contrary to the trend of thermal conductivity. Compared with the P3HT solution weight percentage, density exhibits stronger influence on the variation tendency of the thermophysical properties. In Fig. 3-5(a), the profiles can be simply interpreted as variations within a certain range while in Fig. 3-6 the profiles give

more distinct tendencies with changing parameters. Because the crystal structures are identical for all P3HT thin films, and P3HT solution of same weight percentage probably yields different density, the density can be treated as a more representative factor to explain the thermophysical property difference among all P3HT thin films.

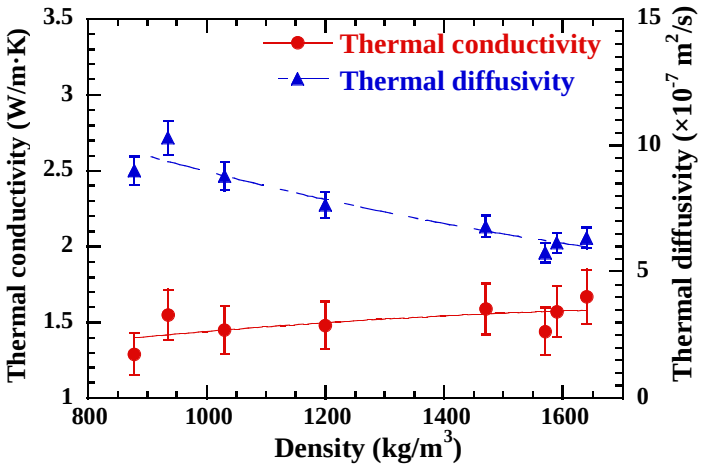

Figure 3-6. Thermal conductivity and thermal diffusivity versus the density of the P3HT thin films listed in Table 3-2, and the curves are used to guide eyes to view the data trend.

For error assessment purpose, error bars are also shown in Fig. 3-4, 3-5(a) and 3-6. As analyzed before in this section, the major contributor of errors is the measurement of dimensions, especially the thickness. Although the deformation caused by micrometer caliper is usually just 1-2 μm, it is not negligible in this experiment because the extremely thin film thickness is only around 20-50 μm. Therefore the maximum measurement uncertainty from the thickness is evaluated to be about 10%, as shown by the error bars in Fig. 3-4. For film length and width, they are read directly from the pictures taken by microscopy and the errors are assumed to be as small as 1%. All experimental devices and

equipment, such as the constant current source, oscilloscope and digital multi-meter are calibrated before the measurement. Therefore the uncertainties from current and resistance readings are negligible. From the equation to calculate effective thermal conductivity, the total uncertainty of k is about 10.1%, demonstrating that the largest uncertainty generates from the measurement of thickness.

For thermal diffusivity, it is directly measured with TET technique and the error is estimated to be 6% as shown by the other two profiles in Fig. 3-2(b). This value is determined by changing the thermal diffusivity to examine if any distinct deviation generates. With thermal conductivity and thermal diffusivity, the uncertainty of density can also be derived and is estimated to be around 12% according to error propagation theory. After obtaining the errors of all necessary variables, the uncertainties of real thermal diffusivity and real thermal conductivity are calculated to be 6.4% based Eq. (9) and 10.7% based on Eq. (8) after subtracting the impact from gold coating, respectively. Error bars for both thermal properties are added in Fig. 3-5(a) and 3-6 to better assist to present the uncertainties in this experiment.

3.4 Anisotropic thermal transport in P3HT thin film

3.4.1 3-dimensisonal anisotropic thermal characterization

P3HT thin film with strong anisotropic crystal structures is synthesized using spin-coating process. Different from ultradrawn polymer films, the draw ratio of P3HT film is not expected to be high. Although strong centrifugal force stretches the molecular chains to orientate along particular direction, the effect is not as strong as the films stretched afterwards. In addition, during the spin-coating process, the chloroform content quickly evaporates and the formed molecular chains contract to certain level. Therefore, the caused anisotropy in crystal structure is not as ideal as expected with ultradrawn polymer films and the molecular chains are mostly with partial alignments regarding specific orientation. The sample preparation is shown in Fig. 3-7(a) and a small rectangular structure is chosen to demonstrate the partially aligned anisotropy in the spin-coated P3HT films. A Cartesian coordinate system is shown in Fig. 3-7(a) to demonstrate how the three-dimensional anisotropic thermal property is defined. *x*-*y* plane is the plane in which P3HT molecular chains are formed. In this plane, two separate directions are again identified based on the orientation of molecular chains. One is the direction parallel to the orientation (*x*-axis) and the other is perpendicular to the orientation (*y*-axis). *z*-axis represents the thermal diffusivity at cross-plane direction. Atomic force microscopy is applied to diagnose the topography of the spin-coated film. Images of different scales in Fig. 3-7(b) show that no evident microstructure is observed. The initial state as obtained from spin coating is

amorphous and the crystallinity is much lower. Annealing is expected to assist transition to higher crystallinity and better alignment [15].

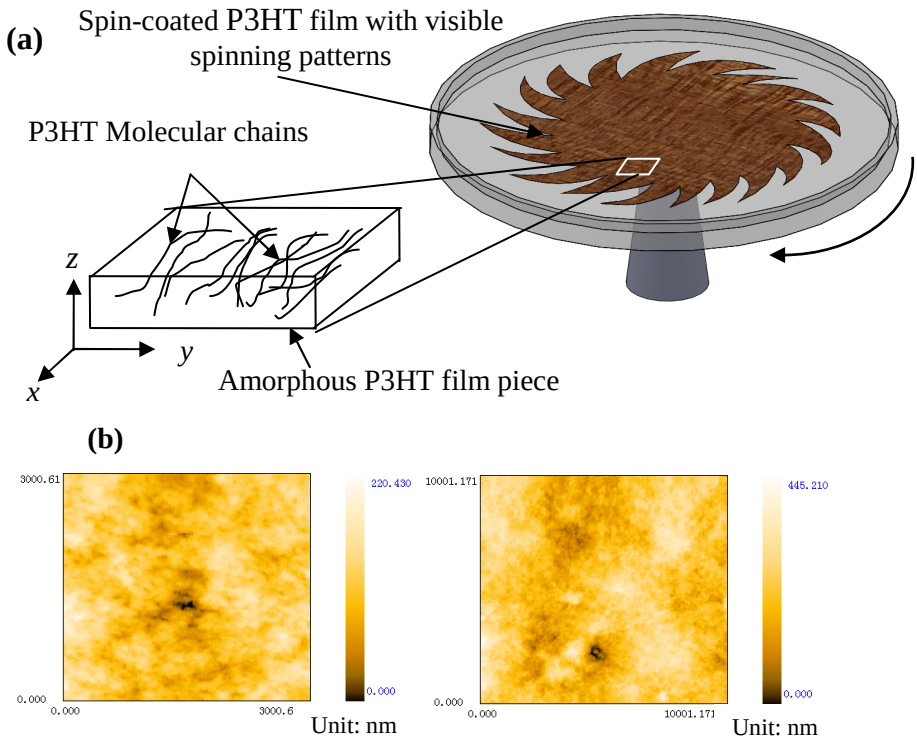

Figure 3-7. (a) A schematic of the molecular structure of a P3HT thin film. The spin-coating process causes the molecular chains to partially align parallel in *x*-*y* plane. (b) AFM images of spin-coated P3HT film as prepared at 3×3 μm (left) and 10×10 μm (right).

In this section, one P3HT thin film is particular selected to demonstrate the anisotropic thermal characterization process and post data analysis using both PLTR2 and TET techniques. Experimental setup for PLTR2 can be referred to Fig. 2-4. Pulsed Nd:YAG laser (Quantra-Ray) of 1064 nm wavelength is utilized to provide periodical laser irradiation. Temporal span of each pulse is about 6 to 8 ns and the energy is about 200 nJ.

Laser beam spatially obeys Gaussian distribution and the size of beam spot is about 8mm. It is much larger than the P3HT film length, which is around 2-4 mm. Size comparison between laser beam spot and P3HT film supports the assumption made in PLTR2 analytical model that the film receives uniform laser irradiation. Constant DC signal provided by a current source (Keithley 6221) is fed through the film through the whole measurement. Magnitude of the DC signal is carefully selected to ensure both appreciable voltage signal level and minimum joule heating. An oscilloscope (Tektronix TDS 7054 digital phosphor oscilloscope) is connected to the film to record voltage variation for data analysis. As seen in Fig. 2-4, the recorded voltage profile contains information for determining both in-plane and out-of-plane thermal properties. In Fig. 3-8(a), for the selected P3HT thin film, fitting profile of thermal decay for deducing in-plane thermal diffusivity is presented and the thermal diffusivity is determined to be 4.66×10^{-6} m^2/s. By varying the value of thermal diffusivity, the uncertainty of the in-plane thermal diffusivity derived to be 10% using PLTE2 technique when distinct deviation is observed. For out-of-plane thermal diffusivity, it is calculated directly based on the rapid temperature rise under laser irradiation, as shown in Fig. 3-8(b). The time to reach half of the maximum temperature rise, $t_{1/2}$, is determined from this graph and then is used to deduce the out-of-plane thermal diffusivity using Eq. (11). However, as observed in this graph, the temperature rise profile is not smooth and contains oscillation in data. Further examination shows that the voltage increase is just slightly greater than 1.5 mV and very comparable to the noise level, which is around 0.3mA. Based on the laser flash theory, thermal excitation is applied on front surface and

consequent temperature increase on rear surface is probed for analysis. However, the maximum front surface temperature rise of front surface under laser irradiation is estimated to be tens of times greater than the maximum temperature at the rear surface. In order to induce the appreciable temperature change, the laser energy exerted on front surface of the P3HT film needs to be strong but destruction may probably be caused to the film. To simultaneously keep the sample intact and achieve sensible signal, different values of laser energy and probing DC current are tried to acquire the best voltage signal. Although the profile in Fig. 3-8(b) still features obvious oscillation and noise, it is good enough for derivation of out-of-plane thermal diffusivity. Further analysis using weighted smooth algorithm to fit original data points helps to determine an accurate value of $t_{1/2}$. The out-of-plane thermal diffusivity α_{cross} using this strategy is determined to be 2.14×10^{-7} m^2/s, about one order of magnitude lower than the in-plane direction.

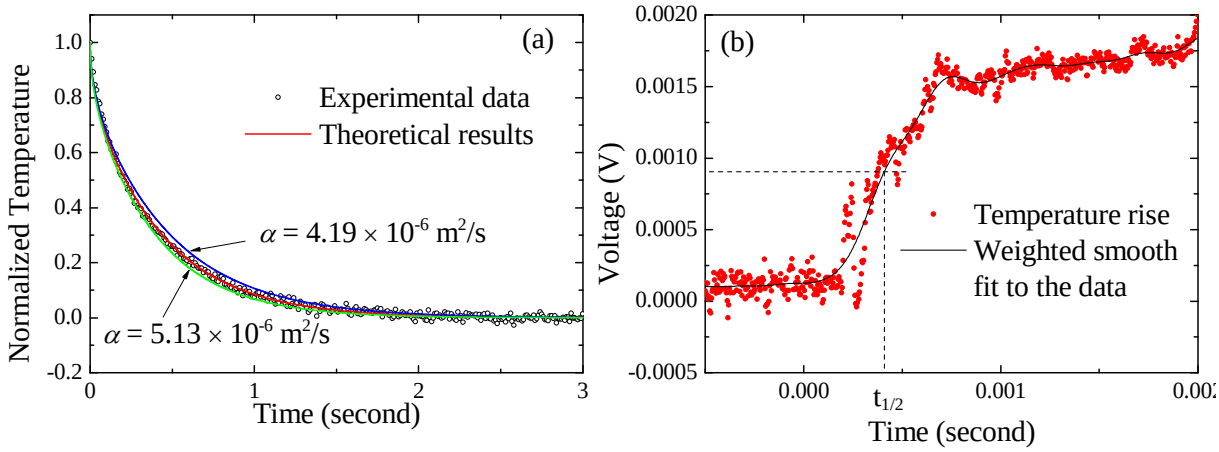

Figure 3-8. (a) Fitting curve to derive the in-plane thermal diffusivity using PLTR2 techniques and (b) Temperature rise curve from pulsed laser irradiation.

Different from PLTR2 technique using laser irradiation, TET technique applies electricity as a source of thermal excitation and measures in-plane thermal properties only. Experiment setup of TET technique is similar to that of PLTR2 as shown in Fig. 2-4, except that laser apparatus is no longer required. Same current source (Keithley 6221) is used to supply step current signal and the voltage response is recorded by the high-speed oscilloscope (Tektronix TDS 7054 digital phosphor oscilloscope). Least square fitting results from TET techniques is shown in Fig. 3-9(a) and the in-plane thermal diffusivity is derived to be 4.73×10^{-6} m^2/s. The same strategy by altering the thermal diffusivity to observe appreciable deviation is used to determine the uncertainty of TET technique. Uncertainty for the thermal diffusivity from TET measurement is about 8%. Comparison between the in-plane thermal diffusivity determined by TET and PLTR2 significantly suggests that the in-plane thermal diffusivity is derived with high creditability, with only about 1.5% difference. From the voltage-time profile in TET technique, thermal conductivity is further calculated with the calibration process of temperature coefficient of resistance. To execute the calibration, a heating plate is used to provide heat fluence and thermocouple is closely attached to the P3HT film, ensuring that the thermometer reading can accurately reflect the temperature change of thin film. A digital multimeter (Agilent 34401A) is connected to monitor the resistance change. As analyzed before, the heating and the consequent temperature range are controlled moderate to assure the intactness of P3HT thin films [134]. A typical calibration profile of this selected P3HT thin film is displayed in

Fig. 3-9(b). Distinct linear temperature-resistance relationship similar to metallic materials is presented and the resistance is mainly contributed by the gold film, which strongly enhances the electrical conduction of the film. The temperature coefficient of resistance is determined to be 3.54×10^{-2} Ω/K for this film. With 14mA DC current passing through the film, resistance change is calculated to be just 1.36 Ω and the relevant temperature variation is 38.4 K, suggesting a modest temperature variation during the calibration. Thermal conductivity is then derived as 3.98 W/m·K, close to the thermal conductivity of P3HT film in our previous work [47].

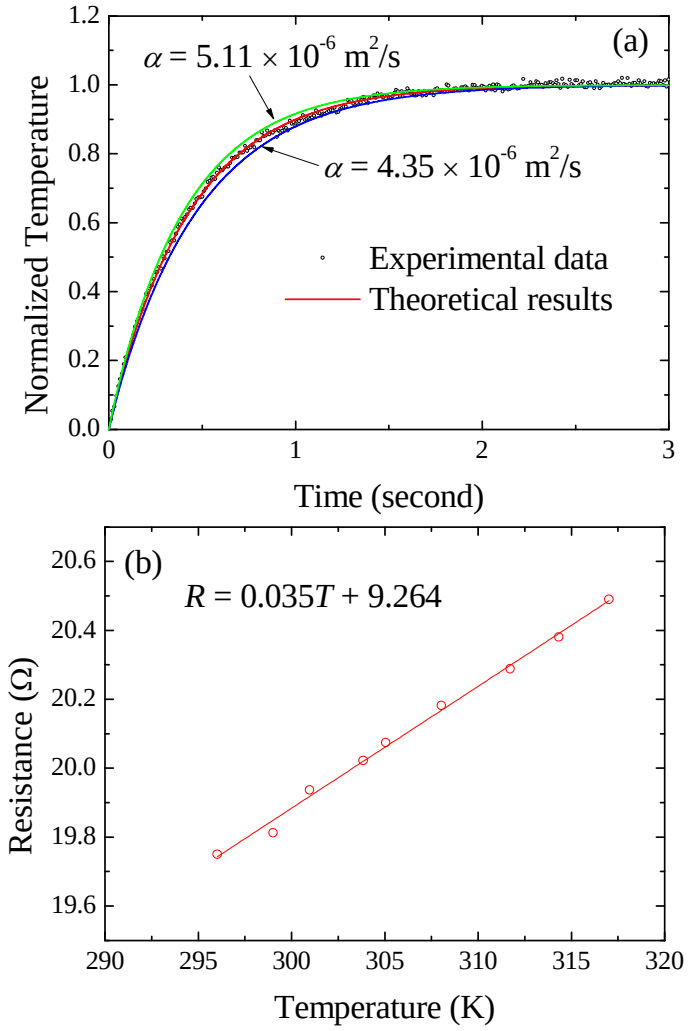

Figure 3-9. (a) Comparison between theoretical solution and experimental data for P3HT microfilm using TET and (b) linear fitting graph of temperature coefficient of resistance for P3HT film.

So far the thermal properties determined using TET and PLTR2 are still effective values, containing contributions from the gold film. Methodology to exclude effect of gold film is introduced in previous section. Effective volume-based specific heat is calculated as

$C_{eff} = \rho c_p = k_{eff} / \alpha_{eff}$. Using the effective thermal properties from TET, effective volume-based specific heat is determined to be 0.82×10^{-6} J/m^3·K. Value of Lorenz number used in this work is 4.9×10^{-8} W·Ω/K^2, which is chosen considering that the Lorenz number drastically increases with reduced size. For bulk metals, Lorenz number is used as 2.45×10^{-8} W·Ω/K^2, while for gold film of 10 nm thickness, this value rises to 7.40×10^{-8} W·Ω/K^2. Therefore an approximated mid-value (4.90×10^{-8} W·Ω/K^2) for Lorenz number is estimated and used in this work. By subtracting the effect of gold film, in-plane thermal diffusivity of P3HT thin film is revised as 4.09×10^{-6} m^2/s for PLTR2 and 4.12×10^{-6} m^2/s for TET. Therefore the influence from gold films is estimated to be about 12%, indicating that gold film does not significantly impact the measurement. In-plane thermal conductivity is modified using Eq. (8) and is derived to be 3.43 W/m·K, implying that the impact of gold coating is also small (around 14%). Calorimetric measurements revealed that for regioregular P3HT an endothermic transition from a crystalline to a liquid crystalline state occurs at 210 - 225 °C [9]. However, because that the temperature during the experiment spans around 25 - 60°C, the endothermic transition is not considered and the specific heat is around 1550~1620 J/kg·K, depending on the instantaneous temperature of the P3HT film [15]. According to Erwin's work [14], the density of P3HT thin film can be derived based on film thickness and the molecular weight of a P3HT monomer. The average value of density for P3HT thin film is determined at 1.33 ± 0.07 g/cm^3 by measuring the thickness and combining the Rutherford backscattering spectroscopy data. Nevertheless, in this work the density of P3HT thin film is individually estimated using obtained thermal conductivity,

thermal diffusivity and specific heat, based on the definition of the thermal diffusivity, $\alpha = k / \rho c_p$. The density of the P3HT thin film is calculated to be 506 kg/m^3, much lower than the literature value. Considering that spin-coating process induces highly porous structure, the density is reasonably lower than bulk value.

3.4.2 Anisotropic thermal transport in microscale P3HT films

Thickness of prepared P3HT thin films varies in a range from 10 to 35 μm. The thickness measurement is executed using micrometer caliper and the uncertainty is estimated to be around 10% based on multiple measurements. In this part, 3-dimensional anisotropy with thermal transport in spin-coated films will be distinguished and studied, along with explanation from crystal structure perspective. During the spin coating process, combination of the quick volatilization of chloroform content and intense centrifugal force has caused visible spinning pattern seen with the spin-coated film (Fig. 3-7(a)), indicating the existence of particular orientation of molecular chains. Diagnosis of P3HT crystal structure using Raman spectroscopy verifies that distinct orientation exists within the film and the spectra is shown in Fig. 3-10. The band with a maximum value around 1448 cm^{-1} is related to the C_α=C_β bond of the thiophene rings, while the small peak around 1382 cm^{-1} represents C_β-C_β bond stretching [132]. By adjusting the angle between polarized laser and presumed orientation of molecular chains (C_α=C_β bond), the intensity of peak at 1448 cm^{-1} drastically changes. Detailed trend is shown in the inset graph of Fig. 3-10. The intensity of

peak at 1448 cm^{-1} is at the maximum level at 15º. When the angle increases, the intensity accordingly decreases and achieves the minimum level at 90º. This variation profile depicts that there is a direction inside the film along which the Raman spectra give the strongest signal. This direction is assumed to be the orientation of aligned P3HT molecular chains. However this profile also explains that the orientation of chains would not be very perfect and only partial alignment is generated because of the quickly dry process of chloroform and contraction of polymer molecular chains.

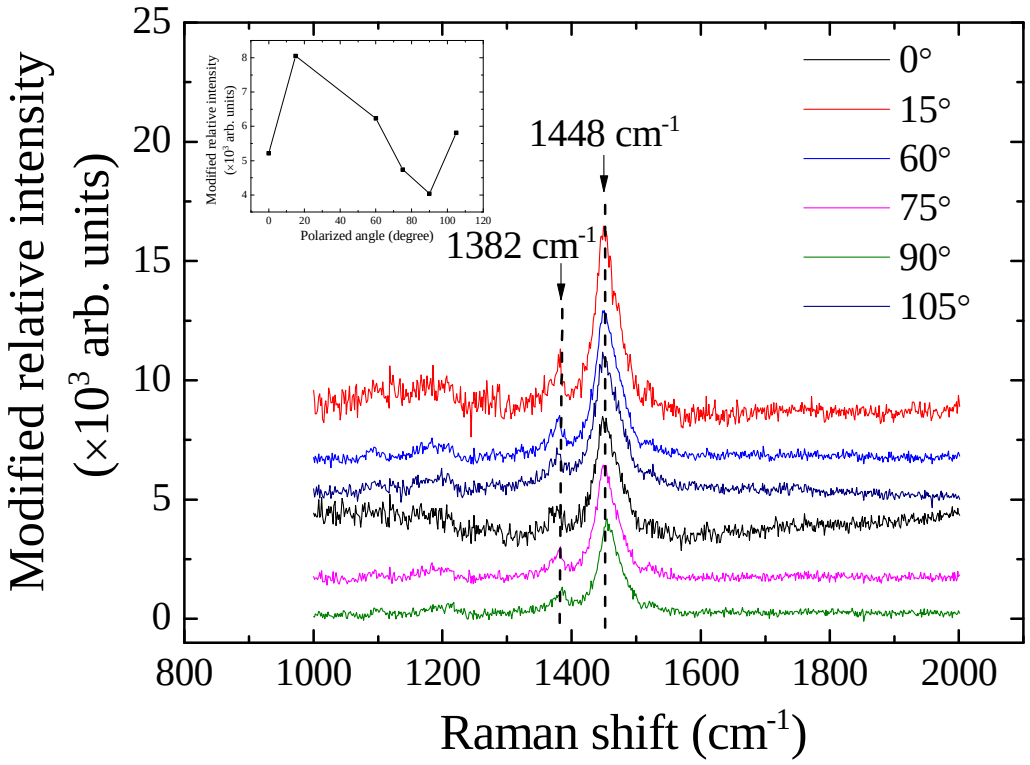

Figure 3-10. Raman spectra of P3HT film with different angles to the polarized laser.

Different from previous investigation of anisotropy in polymer film, the thermal property along all three directions will be studied, as shown by the coordinate system in Fig. 3-7(a). Investigations along all three directions comprise this 3-dimensional characterization of anisotropy in P3HT thin films. The spin-coating process causes the polymer chains to be oriented along a particular direction because of the strong centrifugal force. In addition, the solvent-drying process induces large stress in the film that squeezes the polymer molecules into a few microns along the out-of-plane direction. Therefore, the aligned molecular chains exhibit curvature to certain degrees and the curvature mostly exists along in-plane direction. This anisotropic distribution of crystal structure is support by Fig. 3-11(a). A fact worthy of attention is that thermal conductivity can only be directly measured for parallel and in-plane perpendicular directions because the calibration process is not applicable for out-of-plane perpendicular direction. However, indirect method is still feasible to determine the out-of-plane perpendicular thermal conductivity. With known out-of-plane perpendicular thermal diffusivity $\alpha_{\perp,out}$ and effective volume-based specific heat ρc_p, the out-of-plane perpendicular thermal conductivity is calculated. In Fig. 3-11(a), thermal conductivity versus density of P3HT thin films is shown with error bars. It is observed in this figure that appreciable difference between parallel direction thermal conductivity k_p and perpendicular directions $k_{\perp,in}$ and $k_{\perp,out}$. For parallel direction, thermal conductivity k_p increases from about 2.0 to 3.5 W/m·K. Along in-plane perpendicular direction, the thermal conductivity is vibrating around 0.8 W/m·K. The values of thermal conductivity obtained are close to the results in my previous work about P3HT thin film

[47]. For out-of-plane direction, the thermal conductivity shows flat trend vibrating around 0.2 W/m·K, indicating the weakest coupling of atomic motions along this direction. In addition, the thermal conductivities in parallel and in-plane perpendicular directions present increasing tendency with rising density. Kurabayashi's work [40] indicated that anisotropy in the thermal and mechanical properties both result from the anisotropy of the crystalline domains. The strong coupling of atomic vibrations by covalent bonds along the molecular chains enhances energy transport and yield more substantial thermal conductivity along chain direction. Contrarily, weak Van der Waals interaction between the neighboring chains impedes the transport of lattice vibrations and induces relatively large thermal resistance to conduction between the Chains. For polymer film that embraces perfectly aligned structures, the thermal conductivity anisotropy factor $k_{\mathrm{p}} / k_{\perp,in}$ is predicted to be greater than 10^3 [135]. In this study, the molecular chains in spin-coated film are estimated to be partially aligned as discussed before. Thus, the thermal conductivity anisotropy factor is estimated to be varying around 2 to 3, much lower than values for perfectly orientated structure.

In Fig. 3-11(b), thermal diffusivities for both parallel and perpendicular directions for all samples are presented with error bars. Analogous to thermal conductivity, thermal diffusivity also exhibits distinct anisotropy. Among all three directions, thermal diffusivity in the out-of-plane perpendicular direction, $\alpha_{\perp,out}$, varies in the range from 1 to 3×10^{-7} m^2/s. These values are about one order of magnitude lower than thermal diffusivities in the other

directions, which are of 10^{-6} m^2/s order. Other than out-of-plane direction, thermal diffusivity also presents distinguishable anisotropy between parallel and in-plane perpendicular directions. In parallel direction, a_p changes from 2 to 4 × 10^{-6} m^2/s, while in in-plane perpendicular directions, the thermal diffusivity $a_{\perp,in}$ is confined within lower range from about 6 × 10^{-7} to 1.2 × 10^{-6} m^2/s. Dependence of thermal diffusivity on density exhibits opposite tendency compared with the thermal conductivity. Higher density induces lower thermal diffusivity, as observed in my previous work [47] regarding the P3HT film. Thermal conductivity only relies on the densities of phonons and the scattering inside film. Therefore with similar crystal structures, higher density means less cavity and enhanced thermal transport. Nevertheless, the thermal diffusivity is a ratio of material's ability to conduct thermal energy over the capability to store thermal energy. Probably because effect of density on storing energy is stronger than enhancing thermal transport, the overall effect is that thermal diffusivity decreases with increasing density. Furthermore, as described in experiment section, PLTR2 and TET techniques are both efficient and precise to characterize anisotropic thermal diffusivity. From Fig. 3-11(b), thermal diffusivities determined by both techniques are observed to be consistent. Calculated difference ((α_{PLTR2} - α_{TET}) / α_{PLTR2}) based on two sets of results mostly varies lower than 30%, confirming that two techniques are capable of characterizing thermal property and results are obtained with a high credibility. A few outliners probably caused by experiment uncertainty are identified.

For error assessment purpose, error bars are also shown in Fig. 3-11. As analyzed before in this section, the major contributor of errors is the measurement of dimensions, especially the thickness. Although the deformation caused by micrometer caliper is usually just 1-2 μm, it is not negligible in this experiment because the extremely thin film thickness is only around 10-35 μm. Therefore the maximum measurement uncertainty from the thickness is evaluated to be about 10%. For film length and width, they are read directly from the pictures taken by microscopy and the errors are assumed to be as small as 1%. All experimental devices and equipment, such as the constant current source, oscilloscope and digital multi-meter are calibrated before the measurement. Therefore the uncertainties from current and resistance readings are negligible. From the equation to calculate effective thermal conductivity, the total uncertainty of k_{eff} is about 10.1%, demonstrating that the largest uncertainty generates from the measurement of thickness.

For thermal diffusivity, the error is estimated to be 8% for TET technique (Fig. 3-8(a)) and 10% for PLTR2 (Fig. 3-9(a)). These values are determined by changing the thermal diffusivity to examine distinct deviation. With effective thermal conductivity and thermal diffusivity, the uncertainty of effective density can also be derived and is estimated to be around 12.9% according to error propagation theory. After obtaining the errors of all necessary variables, the uncertainties of real thermal diffusivity from TET technique and from PLTR2 are then calculated to be 8.6% and 10.8%, respectively, based on Eq. (9). Uncertainty for real thermal conductivity of P3HT thin films is 10.7% based on Eq. (8),

after subtracting the impact from gold film. Then real density of P3HT films is determined from real thermal properties and the error is estimated to be 14.5%. For out-of-plane perpendicular direction, thermal diffusivity presents relatively stronger noise level and the uncertainty contains contribution from thickness measurement and reading of the parameter $t_{1/2}$. It is estimated that errors of out-of-plane perpendicular thermal diffusivity and thermal conductivity are about 17.3% and 22.0%, respectively. Error bars for thermal properties and density are added in Fig. 3-11 to present the uncertainties in this experiment.

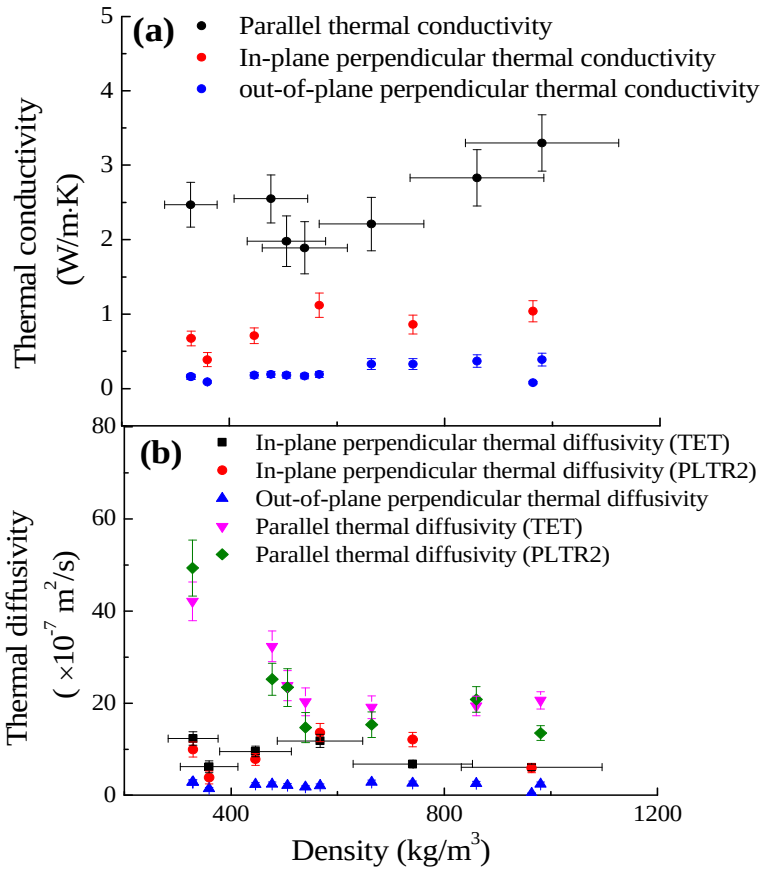

Figure 3-11. (a) In-plane thermal conductivity versus density of P3HT thin films and (b) 3-dimensional anisotropic thermal diffusivity versus density of P3HT thin films.

CHAPTER 4. THIN FILMS COMPOSED OF NANOWIRES

Different from the P3HT thin films fabricated using spin coating process, TiO2 thin film is synthesized using electrospinning technique combined with TiO_2 pre-cursor. For spin coating technique, strong centrifugal force stretches and also aligns each molecular chain along certain orientations. Therefore, the induced crystal structure demonstrates alignment to certain extent. Electrospinning also impose strong electrical force and stretches the solution into single nanowires in a very quick manner. However the orientation of as-spun nanowires is more controllable than film fabricated from spin coating process. In this chapter, no special treatment is imposed on the collection of electrospun nanowires and the distribution of nanowires is random and show interconnected network. In next chapter, it will be seen that if special treatment is done to the collection, highly aligned structure is also feasible.

4.1 Sample preparation

Electrospinning technique [76] is employed for preparing fibular mesostructure composed of nanowires and the experimental setup can be referred to Fig. 4-1. In this procedure, 1.5 g of titanium tetraisopropoxide [$Ti(O\mathit{i}Pr)_4$] was mixed with 3 mL of acetic acid and 3 mL of ethanol. After 10 minutes, the solution was mixed with another 7.5 mL of ethanol containing 0.45 g of PVP (Aldrich, M_w=1,300,000), followed by magnetic stirring for about 1 hour in a capped vial. The well-stirred solution was immediately loaded into a

syringe equipped with a 23 gauge stainless steel needle. The needle was connected to a 20 KV ultra-high voltage which was supplied by a power supply and a voltage amplifier that was able to amplify an input voltage by 1000 times. A plate wrapped by aluminum foil was placed 6 cm below the needle tip for collecting purpose. The whole electrospinning process was performed in open air. With the ultra-high electric field around kV/cm, the polymer solution in the syringe was injected from the needle and was stretched into continuous ultrathin fibers. Given certain duration time, the fibers collected by the aluminum foil form a thin film, which actually consist of numerous discrete nanowires.

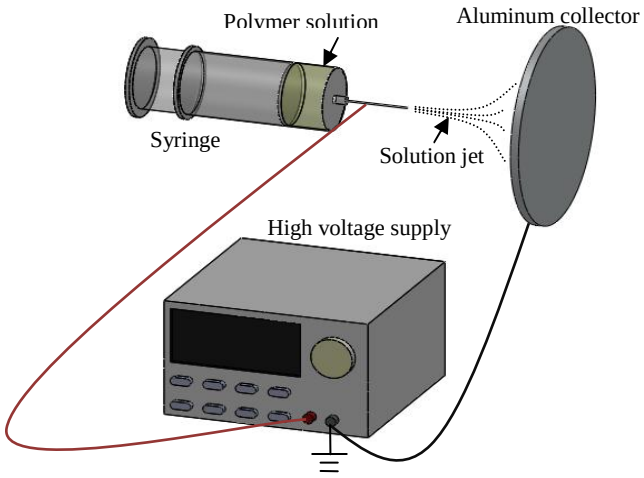

Figure 4-1. Schematic illustration of the experimental setup for the electrospinning technique.

The as-spun film was left in open air for about 5 hours to let the continued hydrolysis of $Ti(OiPr)_4$ to complete and then the PVP compound was selectively removed from annealing in open air at 500 ºC for 3 hours. Atomic Force Microscopy (AFM) was

employed to study the surface topography of samples both before and after annealing, and the images are presented in Fig. 4-2. As observed in these images, each individual nanowire has approximately uniform cross-sectional area, and the average diameter is in the range from 300 to 1050 nm (left image in Fig. 4-2). Because Ti(O*i*Pr)$_4$ can be rapidly hydrolyzed by moisture in the air, continuous networks (gel) of TiO_2 sols are able to keep forming in the nanowires. As the PVP is selectively removed from the sample using annealing, the nanowires maintain the continuous structures and the average diameter decreases to about 200 to 700 nm (right image in Fig. 4-2). This size reduction could be explained by the evaporation of PVP from the nanowires and also the crystallization of TiO_2.

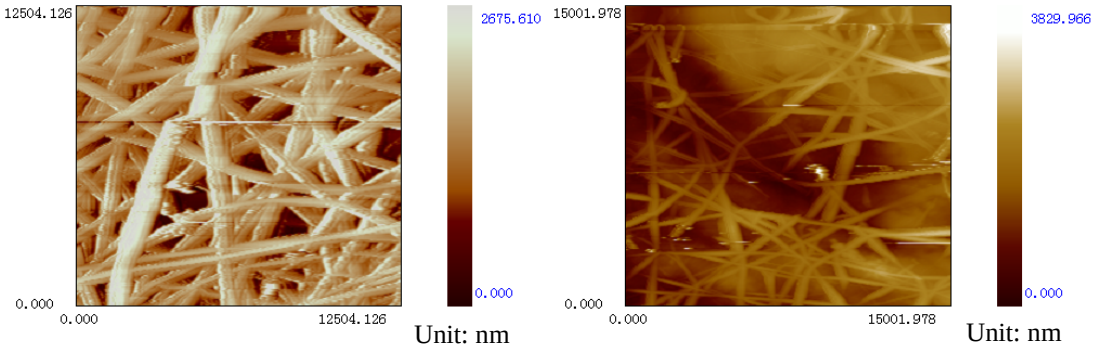

Figure 4-2. AFM images of nanostructure of TiO_2 thin film: (left) before annealing; (right) after annealing.

In order to precisely identify the polymorph of synthesized TiO_2 samples, Raman spectroscopy examination was conducted on the samples and the spectrums of as-prepared and annealed samples are presented in Fig. 4-3. For as-prepared film at room temperature it indicates no distinct peaks but trivial fluctuation. On the other hand, explicit Raman peaks

are observed with the annealed sample. Broader features are located in the range from 100 to 1000 cm^{-1} and 4 distinct Raman peaks are observed at 135, 392, 515, and 633 cm^{-1}. This peak distribution is in perfect accordance with previous results [136], and the annealed sample can be identified as anatase polymorph of TiO_2. The Raman peak at 135 cm^{-1} is very sharp and it has been identified as a symbolic peak for anatase crystal structure when comparing to rutile crystal, which is another typical polymorph of TiO_2 and can be transformed into from anatase under higher temperature annealing. Based on the GF-matrix method using the force constants given in Ohsaka's work [136], the peaks at 135 cm^{-1}, 392 cm^{-1} are the O-Ti-O bending type vibrations and the other modes of peaks at 515 cm^{-1}, 633 cm^{-1} represent Ti-O bond stretching type vibrations.

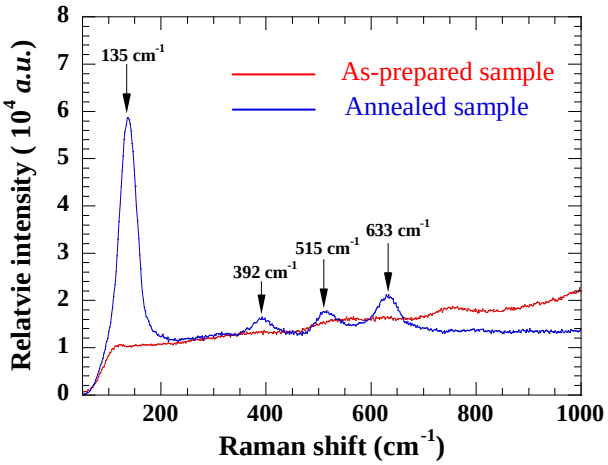

Figure 4-3. Raman spectrum of TiO_2 film at room temperatures and 500 °C.

After obtaining anatase TiO_2 thin films, coating process is necessary for the samples to be efficiently measured by TET technique and calibration process, as introduced in Chapter 2. Because of the poor electrical conductivity of TiO_2 for acquiring strong signal,

an ultra-thin Au film is coated on one side of the film to make it capable of quickly conducting transient electric current and thermal sensing. The coating procedure is executed by using a Denton vacuum coating device and the coating process continues for 200 s, which is estimated to generate a film of 100 nm thickness and is longer than the time applied on P3HT samples. Coating times for different materials are significantly different and it is attributed to the diverse surface topography and structures. In addition, it is also strongly dependent on the conducting nature of the fabricated materials.

4.2 Experimental details

Experimental setup for measuring TiO_2 thin film is similar to that for P3HT film. After its electrical conductance and thermal conductance have been strongly improved by gold coating, the whole sample with the base to hold it was transferred into a vacuum chamber for follow-up characterizations. The Au-coated film was suspended between two aluminum electrodes by silver paste and a *K*-type thermocouple was attached to simultaneously monitor the temperature change. The whole stage including the aluminum electrodes and the sample suspended between the electrodes was positioned on a heating plate. Heat convection effect is minimized so that the one-dimensional heat conduction model can be used to describe the whole setup. Voltage of about 36 V was provided to maintain the process moderate and the data recorded when the temperature of sample starts to decrease from 45 ºC.

TET measurement was conducted when the temperature of sample reaches room temperature and keeps stable. The fed current was estimated to be around a few mA based on the theoretical model. Instant voltage response profile was recorded for further analysis from the oscilloscope. The applied current should be chosen carefully to make sure firstly the voltage change is noticeable and strong enough and secondly the current won't be too strong to cause excess heat accumulation, which would bring damage to the sample.

4.3 Results and discussions

4.3.1 TET measurement of thermal conductivity and thermal diffusivity

Table 4-1. Details of the experimental parameters and results for a selected TiO_2 thin film characterized by using the TET technique.

Length (mm)	2.63
Width (mm)	0.56
Thickness (μm)	57.0
Resistance (Ω)	44.5
DC current (mA)	4.00
Effective density (kg/m^3)	53.1
Measured thermal diffusivity ($\times 10^{-6}$ m^2/s)	3.20
Real thermal diffusivity ($\times 10^{-6}$ m^2/s)	2.94
Effective thermal conductivity (W/m·K)	0.13
Real thermal conductivity (W/m·K)	0.12

The thicknesses of all prepared samples are about 60 μm while the length and width

are of mm scale. The thickness cannot be precisely determined because the fabricated films bear internal loose structure rather than a tightly condensed one like regular bulk material, which is clearly demonstrated in AFM images in Fig. 4-2. When an external force is applied the thickness is easily likely to change and a consequent uncertainty of thickness measurement is estimated to be 10%, which is included in further discussion. A selected sample is used to present the experiment and data processing. Detailed information about the sample dimension and experimental conditions are listed in Table 4-1, and a microscopic image of this sample is shown in Fig. 4-4(a), in which the length and width are marked.

In the TET technique, different thermal diffusivity values of the sample are used to calculate the theoretical temperature rise. The one giving the best of the experimental data is taken as the property of the sample. The normalized curve generated by the least square fitting method is displayed in Fig. 4-4(b) for the sample presented in Fig. 4-4(a). Based on this methodology, the thermal diffusivity of the sample is found at 3.20×10^{-6} m^2/s, which is close to the literature bulk value of 3.17×10^{-6} m^2/s for TiO_2 [137] while the discrepancy stems from both the interior fiber-like structure that may affect the thermal transport and the dimension measurement uncertainty. However, what is attained is not the actual thermal diffusivity of the film. As discussed in the previous section, the TiO_2 was coated with a thin Au film in order to conduct the fed current. The thermal diffusivity obtained by the TET method has the effect introduced by Au coating and this effect can be ruled out using the

concept of thermal conductance as indicated in Eq. (9) with known specific heat and density of the film.

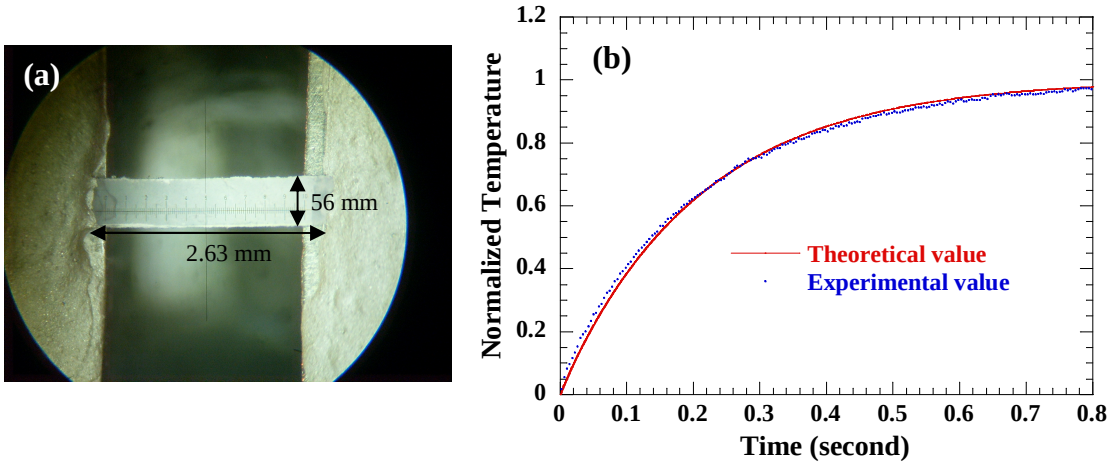

Figure 4-4. (a) Microscopic image of the selected sample listed in Table 4-1 and (b) Comparison between normalized temperature rise versus time between theoretical and experimental data for the sample shown in figure (a).

The specific heat of anatase TiO_2 is mostly treated as a constant and does not change with temperature. However in this study, precise relationship between the temperature and specific heat is required to suppress the uncertainty. Smith [138] gave detailed standard molar specific heat for anatase TiO_2 at different temperatures. The data is fitted with a polynomial curve for ease of future calculation, as presented in Fig. 4-5. Another critical issue in determining the real thermal diffusivity is the density. For bulk anatase TiO_2, the density is measured at 3.89×10^3 kg/m^3 [137]. For loosely-interconnected samples measured in this work, the density is estimated to be much less than 3.89×10^3 kg/m^3 because of the vacancies among the nanowires that compose the film. Therefore correct estimation of sample's density is important for further data processing. In order to

estimate the density, the thermal conductivity of the film is required to be calculated in advance.

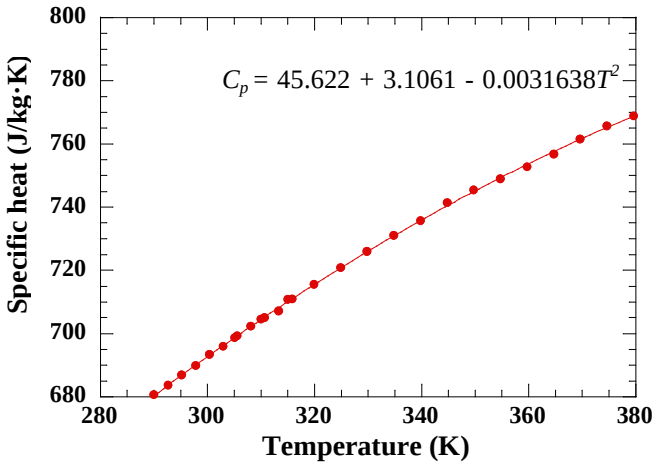

Figure 4-5. Polynomial fitting of the relationship between specific heat and temperature for anatase TiO_2. [138]

The thermal conductivity of the sample is obtained using the calibration of temperature coefficient of resistance η as in previous analysis. The heating power and temperature range is controlled to be moderate to make sure that the sample would not be overheated and the unnecessary heat dissipation is negligible. A profile of temperature coefficient of resistance is displayed in Fig. 4-6 for the sample summarized in Table 4-1. Because the Au coating significantly strengthens the electrical conduction of the sample, the obtained calibration profile presents a temperature-resistance property similar to a good conductor. A linear relationship is fitted to obtain the temperature coefficient of resistance, which is 2.4×10^{-2} Ω/K for this sample. With supplied DC current of 4 mA in the TET experiment, the recorded resistance change of the sample at steady state is 0.89 Ω, which

further helps to determine the total temperature change is about 36.5 K. According to expression of thermal conductivity, with known dimensional parameters and power, it is calculated to be 0.13 W/m·K as listed in Table 4-1 and the effective density is also derived as $k_{eff} \left/ \left(\alpha_{eff} \cdot c_p \right) \right.$. With this expression, the density is calculated to be 53.11 kg/m^3, which is almost two orders of magnitude lower than literature value of about 3.89×10^3 kg /m^3, and then the modification based on Eq. (9) is available to exclude the influence of Au coating. The modified real thermal diffusivity of the film is 2.94×10^{-6} m^2/s, which is about 8% smaller than the effective thermal diffusivity. This indicates that the Au coating has negligible impact on the entire measurement. The real thermal conductivity of the sample is obtained using Eq. (8) and the value is also listed in Table 4-1.

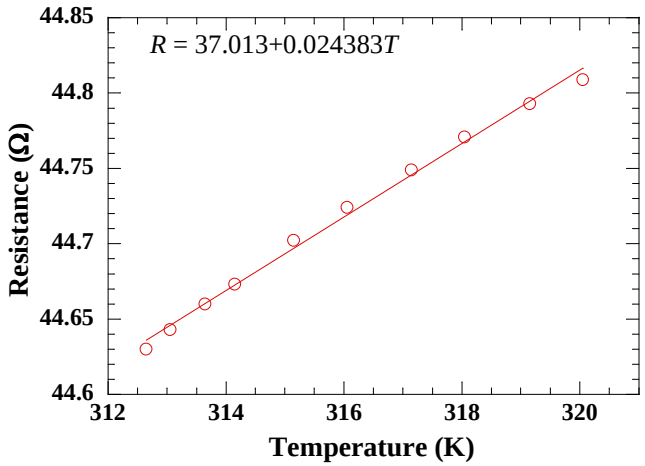

Figure 4-6. Linear fitting curve of temperature coefficient of resistance for the sample listed in Table 4-1.

From Table 4-1, the thermal conductivity of the thin film is only 0.12 W/m·K, more than one order of magnitude lower than the bulk value, 8.5 W/m·K [137]. It is because the

loose structure highly reduces the heat conduction inside the film, and the existence of boundaries oriented perpendicular to the heat flow direction also impacts the effective heat conduction [63].

4.3.2 Thermophysical properties of samples with different dimensions

Samples of various dimensions are measured in this section to explore the relationship between the physical parameters and thermophysical properties. Detailed information of all the samples is listed in Table 4-2, along with the modified thermophysical properties and effective density. The thermal conductivity and diffusivity in Table 4-2 are the values after subtracting the effect of the Au coating. Depending on the duration time and imposed voltage of the electrospinning process, the film thickness varies from 50 to 80 μm and all of them embrace a loosely-interconnected structure. As in previous analysis, because of the nature of interior loose structure, the thickness of a sample cannot be precisely measured and only approximate values are employed in the calculation, which has introduced about 10% uncertainty into calculation. Calculated thermal conductivities are one order of magnitude lower than bulk material, 8.5 W/m·K [137], which approves that the vacant structure within the sample has substantially attenuated the transport of phonon and consequently reduced the thermal conductivity. Based on the expression of thermal conductivity, if the sample is given about 10% measurement error, the uncertainty introduced to the thermal conductivity would not bring significant influence to the calculated results. Listed in Table 4-2 are also the measured results of a sample

before annealing. The as-spun sample composes both amorphous TiO_2 and PVP polymer content, while annealing at 500 ºC selectively removes the PVP content and converts the amorphous TiO_2 structure into anatase polymorph. The measured thermal diffusivity of uncalcined sample is one order of magnitude higher than results of annealed samples, which approves that the vacancies in between the nanowires could weaken the heat transfer process because the annealing removes the PVP polymer and creates more vacancies.

Table 4-2. Experimental data and calculated results of all samples.

	Length (mm)	Width (mm)	Thickness (μm)	I (mA)	$\Delta R/\Delta T$ (Ω/K)	Effective density (kg/m^3)	α ($\times 10^{-6}$ m^2/s)	k (W/m·K)
Unannealed sample	2.28	1.14	30.0	2.00			37.3	
Sample 1	1.31	0.79	55.0	4.00	0.014	25.8	3.05	0.06
Sample 2	1.07	0.55	67.5	4.00	0.044	38.4	3.52	0.10
Sample 3	2.63	0.56	57.0	4.00	0.024	53.1	2.94	0.12
Sample 4	2.45	0.98	82.5	6.00	0.038	109	2.72	0.21
Sample 5	1.39	0.65	60.5	6.00	0.034	160	2.14	0.24
Sample 6	1.85	0.95	59.5	6.00	0.031	217	1.93	0.30
Sample 7	1.36	0.53	63.5	4.00	0.070	373	1.35	0.36

Fig. 4-7 illustrates the variation of thermal conductivity and thermal diffusivity versus effective density, which is calculated based on measured thermal diffusivity and thermal conductivity. The effective density changes a lot from sample to sample, which

means that it majorly depends on the preparation procedure. While the effective density ranges from about 25 kg/m^3 to 370 kg/m^3, the thermal conductivity also varies substantially and displays a relatively ascending profile with density increase, which is consistent with Maekawa's conclusion [63]. This can be interpreted that when density increases, more nanowires and less vacancies appear in the film and therefore enhance the heat conduction. Certain discrepancy is observed in this figure and may be attributed to the impurity and defects in the crystal structure. First, the existence of the defects impairs phonon transport and consequently induces lower thermal conductivity. Second, dimension uncertainty introduced by measurement would also bring slight uncertainty to the calculated thermal conductivity.

The profile of thermal diffusivity change with density is also displayed in Fig. 4-7 and a profile contrary to the thermal conductivity is observed for the measured samples. With density increase, the thermal diffusivity decreases from 3.05×10^{-6} m^2/s to 1.35×10^{-6} m^2/s. Although the ability of the sample to conduct heat is enhanced with a higher density, more condensed structure simultaneously reinforced the capability to storage heat. This comprehensive effect is to weaken the thermal diffusivity because the capability to store heat is augmented more than the ability to conduct heat. Deviation is also observed and it follows the explanation similar to the thermal conductivity. For these samples, they may have impurity and defect inside the crystal structure and hence cause irregularity in the heat conduction capacity.

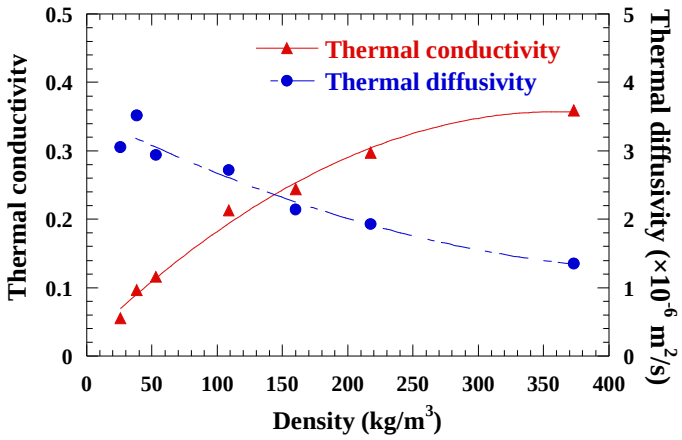

Figure 4-7. Thermal conductivity and thermal diffusivity of TiO_2 thin films versus the density as listed in Table 4-2 and the curves are to guide to view the data trend.

4.4 Intrinsic thermal conductivity of TiO_2 nanowires

The calculated thermal conductivity is the overall (effective) value of the film. From Table 4-2 it can be observed that the values are significantly lower than typical bulk value, 8.5 W/m·K [137]. The interpretation for this significant difference is that for the measured samples, internal loose structure and disordered crystalline extremely reduced the thermal energy transfer between molecules by phonons. When the effective thermal conductivity of film is obtained, to derive the intrinsic thermal conductivity of the discrete TiO_2 nanowire becomes feasible and a physical model is designed to fulfill this purpose. Schematic of the model is displayed in Fig. 4-8. An infinitesimal volume is presumed to accommodate certain number of TiO_2 nanowires, the total amount of which is n and the average cross-sectional area of which is A_f. Assumptions are made that the presumed volume is small

enough to comprise minimal interconnection of nanowires and the heat transfer within each nanowire does not influence the heat transfer in its neighbors. The length and width of this infinitesimal volume are Δl and Δw, respectively. This small volume has a unit length in the direction normal to the paper.

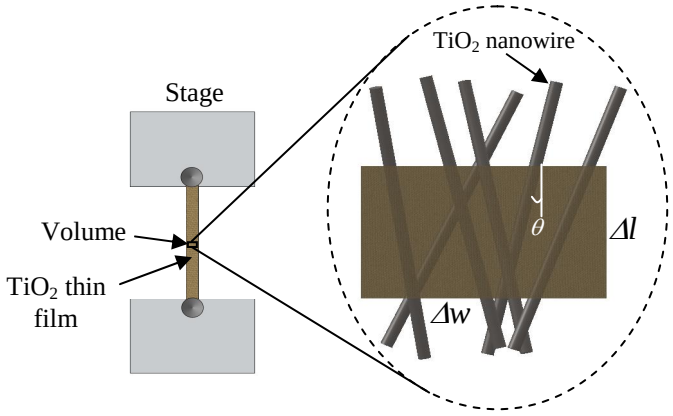

Figure 4-8. Schematic of an infinitesimal volume for deriving intrinsic thermal conductivity of TiO_2 nanowires.

The thermal conductance of the whole volume is attributed to the contribution of every single TiO_2 nanowire. Therefore, considering an arbitrary alignment angle θ, the thermal conductance along the vertical direction for a wire is

$$\frac{2}{\pi}\int_0^{\pi/2}\frac{k_f A_f}{\Delta l/\cos\theta}d\theta\cdot n\cdot\Delta w=\frac{k\cdot\Delta w}{\Delta l}. \tag{16}$$

Then the thermal conductivity of a single nanowire is $k_f=\pi/2\cdot k/(A_f\cdot n)$. The effective length of a single nanowire is determined as

$l_{eff} = 2/\pi \int_0^{\pi/2} \frac{l}{\sin\theta + \cos\theta} d\theta = 0.793\Delta l$. Similarly, the total mass of this volume is estimated as the sum of the mass of each nanowire as $l_{eff} \cdot A_f \cdot \rho_f \cdot n \cdot \Delta w \cdot 1 = \Delta l \cdot \Delta w \cdot 1 \cdot \rho_{eff}$. Then the total number of TiO_2 nanowires n is calculated as $\rho_{eff} \big/ \left(0.793 A_f \rho_f\right)$. The intrinsic thermal conductivity of TiO_2 nanowires is then calculated as

$$k_f = \frac{\pi}{2} \frac{0.793 k \rho_f}{\rho_{eff}} = 1.246 \rho_f \alpha c_p . \tag{17}$$

From Eq. (17), the intrinsic thermal conductivity of TiO_2 nanowires is relevant to bulk density, the thermal diffusivity and specific heat. Calculated results based on Eq. (17) for all samples are listed in Table 4-3. It is observed that the intrinsic thermal conductivities are an order of magnitude higher than the measured value of the thin films and of the same order of magnitude as the reported bulk value, 8.5 W/m·K [137], whereas discrepancies are observed. Such discrepancy could come from the physical model used here. Based on the AFM images, the nanowires contain both straight and curved features. Therefore the straight shape of nanowires is an idealized scenario. Additionally, the target volume is assumed to contain minimal interconnections for simplicity. However, in practical composition, the structure shows distinct entangled characteristic and the interaction between nanowires cannot be ignored. Second, the uncertainty coming from the estimation of thermal diffusivity also impacts the results according to Eq. (17). The thickness of each film could have large uncertainty in measurement because of the interior loose structure of

the film. Inside the films there exists large amount of vacancies which also brought uncertainty into the measurement and calculation.

The mean free path of phonons in the sample is consequently calculated based on the calculated intrinsic thermal conductivity to estimate the effect of nanowire thickness and length. Thermal conductivity is known related to heat capacity per volume (*C*), particle group velocity (phonons) (*v*) and mean free path (*l*) as $k_f = 1/3Cvl$. The typical value of heat capacity (*C*) for anatase TiO_2 is 2.76×10^6 J/m^3·K. The sound velocity of anatase crystal is applied here as the group velocity of phonons and a mean value of 4181 m/s [139] is employed in the calculation. The calculated phonon mean free path for each sample is listed in Table 4-3 and the results fall within the range between 1 to 3 nm. According to the AFM images, the length and thickness of nanowires are substantially greater than the phonon mean free path. Therefore the scale of sample boundary has no strong influence on the phonon transport and the major restriction on the heat conduction comes from crystalline structural defect.

Table 4-3. Intrinsic thermal conductivity of discrete TiO_2 nanowire and derived mean free path.

	Effective thermal conductivity (W/m·K)	Intrinsic thermal conductivity of nanowires (W/m·K)	Mean free path of phonons (nm)
Sample 1	0.06	10.4	2.73
Sample 2	0.10	12.2	3.15
Sample 3	0.12	10.6	2.93
Sample 4	0.21	9.48	2.43
Sample 5	0.24	7.40	1.92
Sample 6	0.30	6.63	1.72
Sample 7	0.36	4.67	1.21

CHAPTER 5. ANATASE SINGLE TIO_2 NANOWIRE

In Chapter 3 and 4, attentions have been paid to thin films of tens microns thickness and the properties are mostly meso-structure properties. Due to the various interior structures, thin films present diverse thermal properties highly dependent on the fabrication conditions and sample preparation process. In this chapter, our focus converts to TiO_2 nanowire, which is intrinsic component of TiO_2 thin film. Consequently the dimension of material is reduced in t his chapter to a few hundred nanometers, which is comparable to the mean free path of phonon and would possibly induce distinctly different thermal transport phenomenon compared with macroscopic samples. In Section 5.1 and 5.2, sample preparation procedure is introduced and because of the extremely small scale, the preparation and characterization procedures are significantly modified compared with that for thin films. In section 5.3, experimental results using TET technique and calibration are displayed to demonstrate the size effect on thermal properties and also the secondary porosity generated during the fabrication process. For the nonlinear effects emerged within the data, two methods are introduced in section 5.4 to suppress unnecessary effects and to obtain more accurate results.

5.1 Sample preparation

Because of the extremely small scale, sample preparation of single TiO_2 nanowire is a more delicate and complicated processes than that of thin films. Fig. 5-1 presents the

whole sample preparation procedure including electrospinning technique setup, coating of iridium film over the nanowire, focused ion beam-assisted platinum soldering process and final configuration of the testing device. Detailed precursor solution configuration is provided in Section 3.2.1. Electrospinning technique, as a manageable technique to synthesize fibular nanostructures, is employed and the setup is indicated in Fig. 5-1 (a). A piece of TEM grid with two 1.5 mm × 0.1 mm slots was pre-coated with gold to have only one slot non-conductively open, serving as the collector to collect spun nanowires and align them over the slot. Because of the symmetric electrical force, the precursor solution will be pulled out, stretched and deposited to have highly-oriented alignment [81]. The as-spun nanowires were then placed in open air for 5 hours to achieve complete hydrolysis, followed by 3-hour calcinations at 500 °C to remove the PVP content. During calcinations, size reduction was observed as mentioned in previous chapter because of the decomposition of PVP content [76]. This process potentially causes internal structure irregularity and defects, inducing certain impact on material properties. After selective removal of other nanowires by using tweezers, only one nanowire was chosen to be left over the slot for later processing and characterization, as presented by the TEM grid in Fig. 5-1(b). A slight modification from previous coating experiment is that iridium sputter coating was applied in this chapter (by Q150T sputter coater) over the TiO_2 nanowire for electrical conducting purpose instead of gold coating [46]. Gold film is prone to have “micro-island” effect, causing rough coated film surface and probably poor electrical contact when the coating target is relatively small. Comparatively, iridium film is known to be much finer and more

uniform than the gold film and it more significantly improves the coating uniformity and conducting effect. Because the nanowire was simply suspended over the TEM grid slot, the contact between the nanowire and the grid surface may not be good enough to eliminate/suppress the influence of contact thermal/electrical resistance. Focused Ion Beam-assisted platinum soldering (Quanta 3D Dual-beam system) was used to weld both ends of the nanowire to the TEM grid surface. As seen in right picture in Fig. 5-1(c), both ends of a single TiO_2 nanowire are covered by deposited rectangular-shaped Pt pads. In Fig. 5-1(d), the left picture gives the overall configuration of a testing base with the prepared TEM grid and suspended Ir-coated and Pt-soldered TiO_2 nanowire. This testing base was then moved to a vacuum chamber for further thermal characterization. On the right is the SEM picture of the nanowire sample 7 and two Pt pads are clearly seen on both ends of the nanowire with an enlarged inset picture of one pad. This pad completely covers the nanowire-base contact and ensures excellent electrical conduction and heat dissipation.

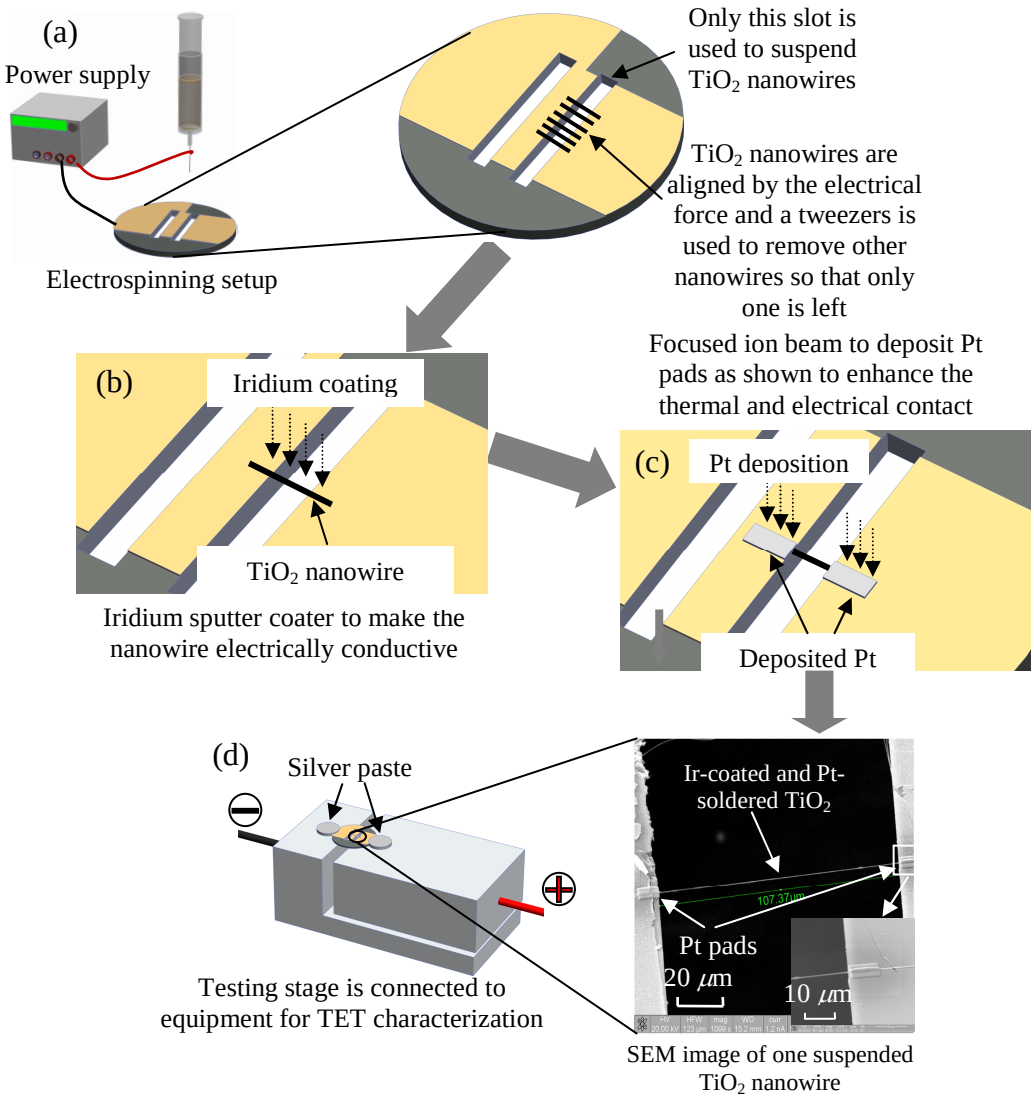

Figure 5-1. Complete sample preparation includes: (a) electrospinning for fabricating parallel TiO_2 nanowires. On the right is a magnified image of a TEM grid for suspending deposited parallel nanowires; (b) Iridium sputter coating to deposit thin iridium film over the single TiO_2 nanowire, on the right is a magnified picture of the working slot only; (c) Focused ion beam-assisted platinum soldering process to solder both ends for better electrical and thermal conducting purpose. Two soldered Pt pads are shown to cover both ends of the nanowire on the slot in the right picture; (d) the whole piece of TEM grid with Ir-coated and Pt-soldered TiO_2 nanowire is transferred onto a testing stage for further thermal characterization. On the right is a SEM image of the fully-prepared TiO_2 nanowire, which is marked as sample 7 in this experiment.

To confirm the polymorph of the prepared sample, Raman spectra examination by using a Voyage confocal Raman spectroscope is displayed in Fig. 5-2(a) to show the authenticity of anatase crystal structure. Four distinct peaks at 132, 390, 514 and 630 cm^{-1} as presented in Chapter 4 show that the annealing at 500 °C for 3 hours has turned the amorphous material into anatase crystalline, which is consistent with previous discussions. According to Ohsaka *et al.* [136], the peaks at 132 cm^{-1} and 390 cm^{-1} are the O-Ti-O bending-type vibrations, and other two modes of peaks at 514 cm^{-1} and 630 cm^{-1} represent Ti-O bond stretching-type vibrations. Additionally, in order to observe the impact from the calcinations and also the surface structure of the nanowire, scanning electron microscopy (SEM) is employed to investigate the nanostructure. In Fig. 5-2(b), the sample is obtained simply after hydrolysis in open air for 5 hours and the surface structure is very smooth and no dents or other features are evident. Fig. 5-2(c) presents an image of a calcined nanowire which exhibits a wavy and uneven surface structure. Similar phenomena have been generally observed in electro-spun TiO_2 nanowires. The porous structure existing between the nanowires inside bulk material is called the primary porous structure. The porous structure within individual TiO_2 nanowires occupies a relatively smaller portion and exists in smaller scale. Therefore, it is defined as secondary porous structure for comparison purpose. The reason of how it originates can be interpreted as follows. First, the TiO_2 nanowires are sintered by aggregation of TiO_2 particles with continuous crystallization at high temperature because the particles favor a round shape to minimize the surface area. Second, the decomposition of PVP content during calcination distorts the nanowire and

leaves an irregular fibrous matrix along with shrinkage of the nanowire diameter. Consequent internal structure irregularity and imperfections from calcination will be the principal explanation for the dramatic change of physical properties and thermal performance.

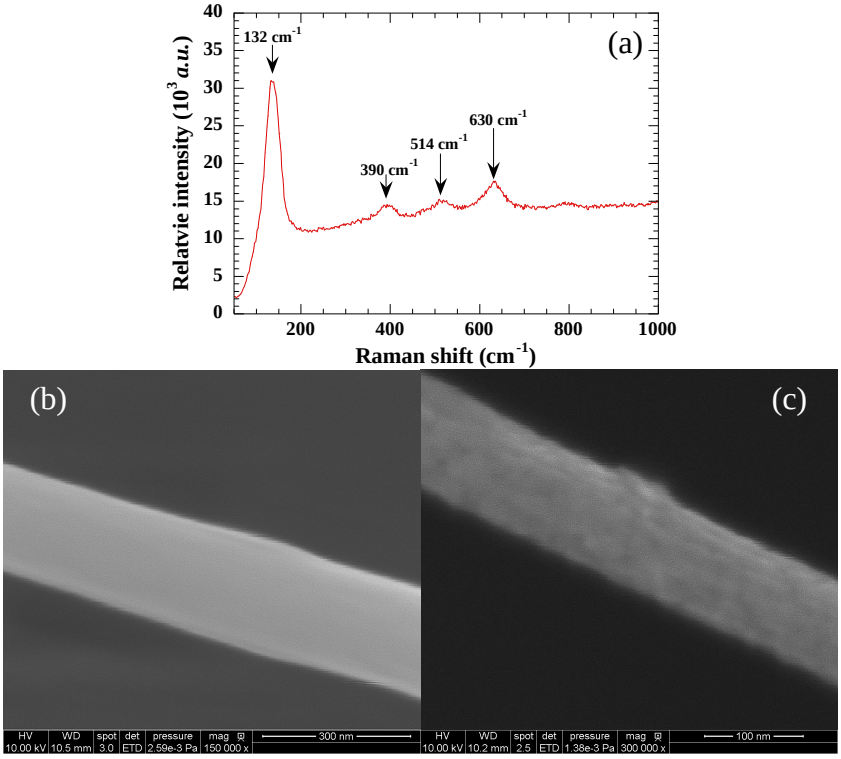

Figure 5-2. (a) Raman spectra of a TiO_2 nanowire after complete calcination to confirm its anatase polymorph; (b) high-magnification SEM image at 150,000× of the as-spun nanowire to show that the surface is very smooth, and (c) SEM image at 300,000× magnification of calcined TiO_2 nanowire that embraces bumpy and porous surface. Images in (b) and (c) are not from the same sample and are only for surface porosity demonstration purpose.

The prepared testing base shown in Fig. 5-1(d) is ready for thermal characterization. Both the electrical and thermal conductance of TiO_2 nanowires are dramatically enhanced

by the iridium coating and it therefore shows metal-like characteristics. To determine the temperature coefficient of resistance of TiO_2 nanowires, calibration procedure is again required and the configuration is indicated in the right dashed line box in Fig. 5-3(a). Different from previous micro-scale film-like samples, it is difficult to directly apply thermocouples to the nanowire surface to sense the temperature change due to its nanometer scale. Furthermore, the layered structure at the wire-base contact generated in sample preparation will cause significant thermal dissipation among layers, thus the ambient temperature would be most likely different from the temperature of the sample. In order to accurately monitor the temperature change of the sample, a device was designed and placed in the vacuum chamber as displayed in Fig. 5-3(a) to both create a uniform temperature field and to maintain equilibrium between the sample temperature and its ambience. For the testing device, the distance between top and bottom plate was about 1 inch and both plates were pasted with a Kapton insulated flexible heater (from Omega) as heat sources. The wall was made from acrylic glass to reduce unnecessary heat loss. Adjustable DC power for both heaters was provided by a dual-output DC power supply (Agilent E3649A) and two pasted thermocouple were connected to a programmable temperature controller (Stanford Research Systems) to monitor the temperature through the whole calibration process. The calibration process was performed when the temperature descends from about 50 °C to room temperature. During the cooling process, limited power is provided from the power supply to ensure the whole process is slow and moderate so that the assumption of quasi-equilibrium is appropriate to describe this calibration procedure.

Taking sample 7 for instance, its typical calibration curve is shown in Fig. 5-3(b), in which the resistance reduces from about 12440 Ω to 12250 Ω while the temperature decreases from 321 K to 307 K. Linear fitting is established based on the recorded data and the deviation from standard metal-like resistance-temperature properties is probably attributed to the structure of Ir on the nanowire surface. The fitted temperature coefficient of resistance for sample 7 is about 12.4 Ω/K and it is adopted to calculate the effective thermal conductivity of the nanowire.

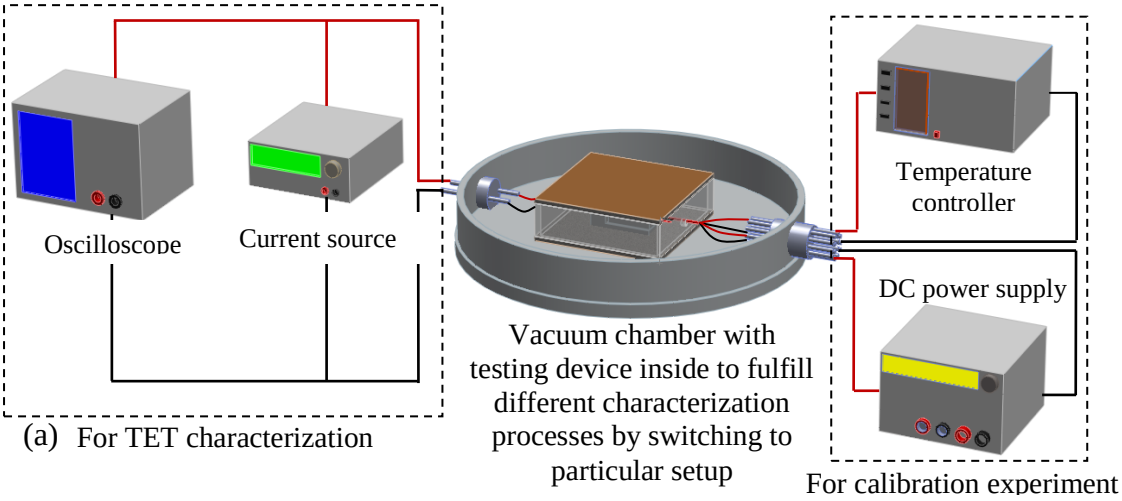

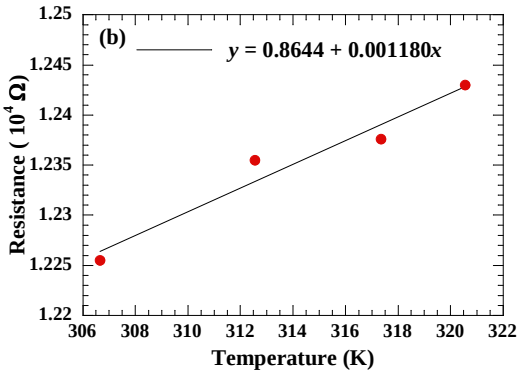

Figure 5-3. (a) Schematic of the thermal characterization setup. A testing device is positioned in a vacuum chamber connecting to two equipment sets. In the left is the equipment for TET characterization and right dashed line box is for calibration experiment. (b) A fitted linear profile of sample 7 from calibration experiment to determine the temperature coefficient of resistance.

5.2 Experimental methods

5.2.1 TET technique

TET technique as introduced before is still employed to characterize the thermal diffusivity of the TiO_2 nanowire but the methodology for deriving is modified due to the

particular abnormality generated in the measurement. As seen in Fig. 5-4(a), when a step DC current provided by the current source is fed through the nanowire, a quick response of voltage evolution of the nanowire is detected by the oscilloscope. Because of the layer-like configuration at the wire-base contact generated from sample preparation, undesired disturbance such as capacitance effect may be included and may give deviation from a pure temperature-resistance relationship. Normally, only one *U-t* profile is required for data fitting to determine the thermal diffusivity. To exclude unnecessary effects, two *U-t* profiles of sample 7 at different feeding currents are needed as shown in Fig. 5-4(a). Two profiles at 20 μA and 10 μA are plotted out and the ratio of their voltage responses is also presented in this figure with the same *x*-coordinate. After precisely calculating the voltage increase, it was found that the voltage is not proportional to the resistance during the transition stage, indicating that the nanowire's transient response is nonlinear and other effects might be included as mentioned before. To exclude other unnecessary effects, the acquired ratio profile will be used for data fitting process because after this treatment, irrelative effects can be eliminated and it contains simply *R-t* relevance. To precisely obtain the effective thermal diffusivity, numerical simulation is employed based on the one-dimensional heat transfer model and the average temperature of the whole sample within each time interval is calculated to obtain the temperature-time profile until steady state is reached. By changing the thermal diffusivity and repeating the numerical procedure, the thermal diffusivity giving the best fitting of the experimental data is taken as the thermal diffusivity of the sample. Detailed theoretical analysis about this signal processing will be

discussed in another work. A fitted curve is shown in Fig. 5-4(b) and it is observed that the fitted normalized curve is very consistent with the theoretical one, indicating that obtained effective thermal diffusivity is accurate enough. The fitted value for sample 7 is 2.28×10^{-6} m^2/s, which is acceptably close to the literature value 3.17×10^{-6} m^2/s [137, 140], considering measurement uncertainty and possible interior structural defect and vacancies that emerged from fabrication. Another two profiles of which the thermal diffusivities are 2.46 and 2.08×10^{-6} m^2/s are also presented to demonstrate how the measurement uncertainty is determined by varying the thermal diffusivity slightly so that the new profiles have distinct deviation from the experimental one. The uncertainty included in the fitting procedure of thermal diffusivity for this sample is about 8%, which will be considered in the uncertainty analysis.

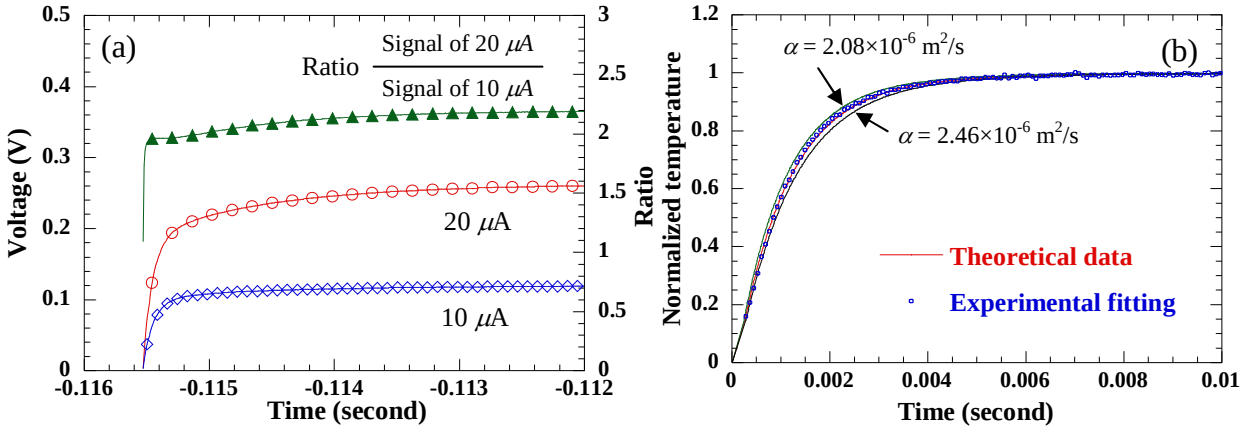

Figure 5-4. (a) *U-t* feedbacks of 10 μA and 20 μA currents for sample 7, and the solid line with triangles represents the ratio of the two *U-t* profiles and (b) comparison plot between theoretical results and experimental fitting for sample 7, with another two fitting curves to demonstrate the uncertainty of this fitting process.

5.2.2 Calibration procedure

The approach to determining thermal conductivity is modified as well compared with that introduced in Chapter 2 [46, 141] and demonstration will be presented also by taking sample 7 as the example. For the TET measurement at each temperature, various currents are supplied to acquire different profiles. For instance, for sample 7 indicated in Fig. 5-4, four different currents, 10 μA, 20 μA, 30 μA and 40 μA, are applied to the sample at 51 °C and the profiles under each current are recorded individually. As metal-like material, the voltage at steady state ascends with increasing current. Based on the TET theory, the thermal conductivity is determined as $k = QL / (12A\Delta T)$. From the calibration results, temperature difference is substituted with the resistance change to modify the equation to $k = QL\eta / (12A\Delta R)$, where η is the temperature coefficient of resistance. Therefore a linear relationship between steady state resistance and supplied power is derived to be $\Delta R / Q = L\eta / (12kA)$, and this relationship for sample 7 is shown in Fig. 5-5, demonstrating an excellent linear trend. A linear fitting is also exhibited in the same figure and the obtained slope contains the thermal conductivity when other parameters are known. For this sample, the slope of fitted straight line is calculated at 3.08×10^8 Ω/W. After incorporating other parameters such as sample length L, cross-sectional area A, and measured temperature coefficient of resistance η, the effective thermal conductivity of sample 7 is finally determined at 4.09 W/m·K, which still includes the impact from iridium coating and will be modified to eliminate its influence.

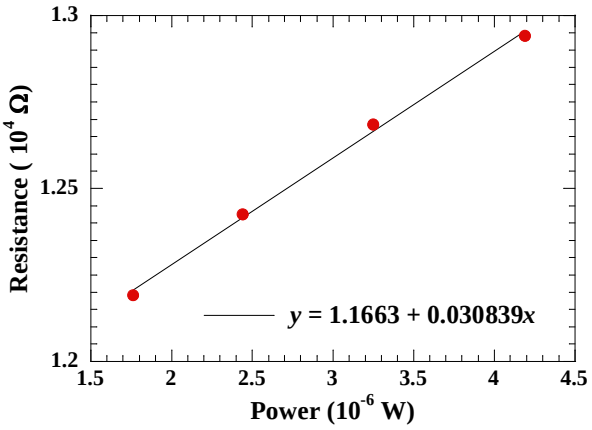

Figure 5-5. Linear relationship between resistance at steady state and power supplied for sample 7 at 51 °C. The slope of the fitting equation is for calculating thermal conductivity if other parameters are known, as shown by equation $\Delta R / Q = L\eta / (12kA)$.

Further modification to obtain the real thermal properties is also needed based on derivation in Chpater 2. The Lorenz number for iridium is chosen to be 2.5×10^{-8} W·Ω/K^2 [129], which is experimentally confirmed to have negligible variation within the temperature range 300K ~ 373K, and consequently is treated as a constant in this experiment [130]. Using temperature and resistance at steady state, the calculated real thermal conductivity of sample 7 is 3.08 W/m·K, indicating that the effect from the iridium coating is about 25%. Compared with previous measurement of micro-scale or submicron-scale material, this effect from iridium coating is relatively large because TiO_2 nanowire is only hundreds of nanometers thick and its surface is rough based on the SEM images. The iridium coating has to reach a certain thickness to form a fine film and to make sure the resistance of the sample reaches a reasonable range for balance between obtaining signal strong enough and including as few unnecessary effects as possible. Therefore the effect

from iridium coatings is higher than that from gold coatings reported before. The same strategy is also applied to calculate the real thermal diffusivity of pure TiO_2 nanowire after the effective volume-based specific heat is obtained as $C_{eff} = \rho c_p = k_{eff} / a_{eff}$. Then the real thermal diffusivity is derived and the impact from iridium coating is excluded.

From the real thermal conductivity, real thermal diffusivity and known specific heat, the density of sample 7 is calculated to be 2545 kg/m^3, lower than reported bulk value of 3890 kg/m^3 [140], supporting the point that possible defects and vacancies are created when PVP content decomposes and the crystalline structure converts from amorphous to anatase during continuous calcination, leading to density lower than bulk value. With other parameters, the modified real thermal diffusivity of sample 7 is 1.76×10^{-6} m^2/s, compared with effective value of 2.28×10^{-6} m^2/s. The estimation of effect from the iridium coating is about 23%, close to the 25% from thermal conductivity modification. The parameters contained in these equations bring in uncertainty and the error propagation will be discussed in following section to examine the accuracy of the techniques.

5.3 Results and discussions

5.3.1 Size effect on thermal and physical properties

In Table 5-1, the dimensional parameters, experimental variables and calculated results are all presented along with experimental uncertainties. The diameters of all

measured nanowires are from 250 nm to 400 nm, and SEM images in Fig. 5-1(d) and Fig. 5-2 indicate that the uniformity of diameter is good. Meanwhile, although the magnification of SEM image is as high as 300,000×, certain vagueness still exists and it causes uncertainty in determining the diameters. The applied current here is controlled to be around tens of μA to ensure the sample structure intact by heating. The temperature coefficient of resistance varies from 1.38 to 17.3 Ω/K and the slopes of resistance-power curves are mostly around 2 to 4×10^8 Ω/W except for two samples. This large variation and particular abnormality are possibly due to the temperature reading oscillation during the calibration process and also the existing thermal contact resistance of the iridium coating. The thermal properties and density in this table are real values excluding the impact from iridium coating and are lower than literature value of anatase TiO_2 crystal [137, 140]. As seen in the SEM image in Fig. 5-2 and also in other publications [76, 78, 80], the wavy and uneven surface structure to some extents demonstrate that the fabricated TiO_2 nanowire features relatively irregular and secondary porous feature compared to bulk material. These irregularities and vacancies are mostly generated from the removal of PVP content during which the degradation may distort the fibrous matrix and also from the aggregation of TiO_2 particles in the crystalline structure transition procedure. With the density, estimates of porosity of the nanowires are also concluded to be much less than 1, from about 31% to 78%, indicating that the calcination not only leaves structural distortions but also remarkable vacancies, which are controllable if experimental parameters are carefully controlled.

Table 5-1. Experimental data and calculated results of all samples.

#	Length (mm)	Diameter (nm)	DC current (μA)	$\Delta R/\Delta T$ (Ω/K)	$\Delta R/\Delta Q$ ($\times 10^8$ Ω/W)	ρ (kg/m^3)	α (10^{-6} m^2/s)	k (W/m·K)	Porosity
1	0.13	250±13	18.0	5.30	2.83	1155.46±142	2.32±0.28	1.38±0.23	29%
2	0.11	370±19	26.0	8.30	2.11	1639.16±202	2.12±0.25	2.26±0.37	42%
3	0.11	295±15	20.0	10.6	2.03	1753.97±216	5.08±0.61	6.01±1.00	45%
4	0.11	383±19	30.0	2.05	0.239	1805.51±222	4.21±0.50	5.14±0.85	46%
5	0.11	320±16	16.0	13.1	4.48	2045.09±252	1.80±0.21	2.42±0.40	53%
6	0.11	340±17	14.0	17.3	4.21	2136.57±263	2.47±0.29	3.59±0.60	55%
7	0.11	342±17	18.0	12.4	3.08	2606.91±321	1.76±0.21	3.08±0.51	67%
8	0.11	360±18	35.0	1.38	0.212	2830.36±348	1.81±0.22	3.34±0.55	73%

The trends on how the thermal properties vary with density are distinctly presented in Fig. 5-6. When the density increases from 866 kg/m^3 to 2677 kg/m^3, the thermal conductivity shows a distinct increasing trend. Except for two obviously abnormal points that are higher than 5 W/m·K, the other data points present ascending tendency around 3 W/m·K with increasing density and the values are lower than the literature value of 8.5 W/m·K for bulk material [137]. As discussed before, the possible reason for this difference is because the interior structure distortions and vacancies from calcination induce phonon-impurity/defect scattering during their transport and thus lower the thermal conductivity. Additionally, the intrinsic thermal conductivity of single TiO_2 nanowire has been estimated before [46] qualitatively and the results were in the range of 5 to 12 W/m·K, which is slightly greater than values acquired from experiment but still consistent considering the

simplifications made in that model and also the secondary porous structure existing within the nanowires in this work. The thermal diffusivity exhibits a contrary moderate trend with changing density. Within the range that density increases, the thermal diffusivity decreases from 2.5 × 10^{-6} m^2/s to 1.77 × 10^{-6} m^2/s, which is almost 30% off. The two exceptional points are still plotted where the error might be induced by measurement uncertainty. With higher density, although the ability of the nanowire to conduct heat is improved, the more condensed structure also reinforces its capability to store heat. The comprehensive outcome is to weaken the thermal diffusivity here because the capability to store heat outweighs the ability to conduct heat.

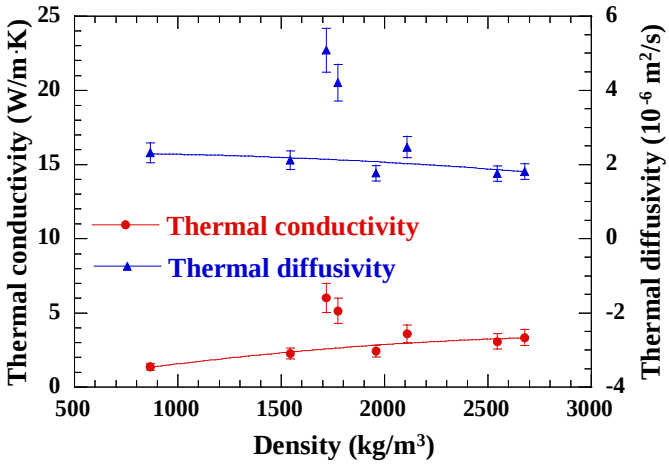

Figure 5-6. Thermal conductivity and thermal diffusivity of single TiO_2 nanowires versus the density for all samples listed in Table 5-1 and the curves are for guiding eyes to view the data trend, with error bar marked on each data point.

The diameter of nanowire is another perspective to understand the thermal properties of small scale material. In Fig. 5-7 a distinct trend is observed between density and diameter. When the diameter increases from 250 nm to 380 nm, the density also

demonstrates a consistently ascending profile from 860 to 2600 kg/m^3 except for a few discrepancies. These discrepancies may come from unexpected experimental variation during sample preparation and also measurement uncertainties. For thermal properties, the variation range of diameter is not large enough to impose substantial impact when it changes from 250 nm to 380 nm, but evident and fluctuating tendency can still be observed for both thermal diffusivity and conductivity. For thermal diffusivity, the value is 2.3×10^{-6} m^2/s when the diameter is 250 nm and decreases to around 2×10^{-6} m^2/s when diameter changes to about 370 nm. While the density increases for about 50%, the thermal diffusivity does not show such a large variation but decreases by 0.3×10^{-6} m^2/s correspondingly with certain discrepancy. As discussed before, because of the extremely small scale, experimental conditions and dimension measurements both can influence experimental uncertainty. As seen in Fig. 5-7, when the diameter increases from 250 to 370 nm, the thermal conductivity strongly increases from 1.38 W/m·K to 6.01 W/m·K. However, this profile is still accompanied with strong fluctuations. Expectation can be made that if diameter increases by more than one order of magnitude, the thermal conductivity would be affected much more significantly.

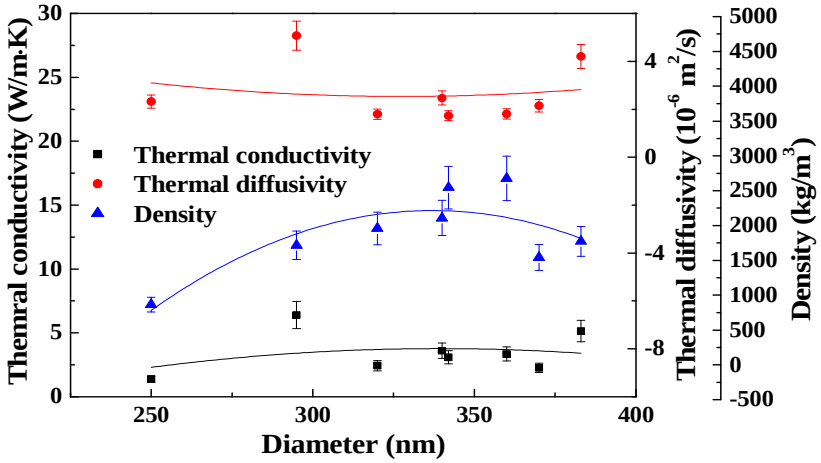

Figure 5-7. Thermal conductivity, thermal diffusivity and density versus the diameter of all measured TiO_2 nanowires, with lines to guide eyes for data trend. Error bar are shown for each data point.

5.3.2 Uncertainty analysis

Because of the small scale of the samples and their delicate nature, uncertainties are inevitably included in the measurement and calculations. The uncertainties primarily come from two parts – dimensional measurement and data acquisition.

The thermal diffusivity is obtained by fitting different values until a profile with the smallest fitting error is acquired. During the fitting procedure, it is reasonable to acquire the fitting uncertainty by changing the values to observe how strong the deviation is from the experimental profile. When the value is varied over ± 8 %, the corresponding profiles show strong deviation from the experimental curve and therefore the uncertainty from data fitting

is 8% as displayed in Fig. 5-4(b). From Eq. (4), the L^2 term also imposes strong impact since it is an exponential expression. With high-magnification SEM image, the error of length measurement uncertainty is as small as 1% and therefore the L^2 term brings about 2% uncertainties. Based on the uncertainty propagation theory, the total uncertainty for thermal diffusivity is about 8.3%. The estimation is basically only for effective thermal diffusivity. For real thermal diffusivity, it is obtained when more factors are considered and will be discussed later after determination of the uncertainty of other variables.

Calculation of thermal conductivity is more complicated based on discussions before. First, the acquisition of the temperature coefficient of resistance includes uncertainties from recording both temperature and resistance. While the temperature is controlled to descend moderately and the fluctuation range is limited to be within 1%, resistance readings show more vibration during the calibration. The possible reason is that the thermal contact resistance makes a certain contribution and has a relatively strong impact on the temperature. The uncertainty is estimated to be 5%. Therefore, the uncertainty existing in temperature coefficient of resistance is about 5.1%, mostly from resistance readings. From the expression of temperature difference, the power is calculated as I^2R, while I is initially set from the current source and R is read directly from the TET profile. Both parameters are accurate enough and the uncertainty can be taken at 1%. Measurement of diameter is based on high-magnification image and it is examined to have 5% uncertainty because of the focusing situation. Uncertainty from length is 1% as

discussed in thermal diffusivity part. Consequently, the total uncertainty for the effective thermal conductivity is about 9%. After the uncertainties of both thermal properties are known as 8.3% and 9%, the uncertainty of effective volume-based specific heat is also calculated to be 12.24% based on discussion before. For real TiO_2 density, it is calculated from the effective value and because the iridium film has a very limited impact, the uncertainty of the real density is the same as that of the effective volume-based specific heat, which is 12.2%

With effective values, the real values are derived based on Eq. (8) and (9), and so are the uncertainties. From Eq. (9), the real thermal diffusivity is calculated from parameters including effective thermal diffusivity α_{eff}, length L, temperature T, resistance R, cross-sectional area A, effective volume-based specific heat ρc_p. The corresponding uncertainties of these variables are 8.3%, 1%, 1%, 1%, 7% and 12.2%, respectively. Therefore the overall uncertainty of the real thermal diffusivity is 11.7%. Following the same method, the uncertainty of the real thermal conductivity is calculated to be 16.5%.

From the uncertainty analysis, it is conclusive that the uncertainty of major parameters and results in this experiment are controlled within acceptable ranges considering the differences among samples and varying experimental conditions. The uncertainties are listed in Table 5-1, as supplements to measurement values, along with error bars marked in figures with each discrete data point.

5.4 Nonlinear effect analysis

An important step in the global fitting procedure is to locate the starting point at which the resistance of the sample can be evaluated. If there is no other effect to shunt the current, the voltage should develop like the one in Fig. 5-8(a) and can be used to represent the resistance-time profile. As indicated in Fig. 5-8(a), at the starting point, the current through the sample already reaches the full value, and the Ohm's law can be used to describe the relation between the measured voltage and the current through the sample. However, after detailed comparison between the original *U-t* profiles of Pt wire and single TiO_2 nanowire (Fig. 5-8(b)), it is obvious that significant dissimilarity exists. For a Pt wire, at the moment that the current is provided, the voltage increases immediately to the value that contains full current and resistance, with simply one abrupt increasing point due to the finite rise time of the current source. Additionally, the decaying state caused by termination of the current is also instantaneous and contains no irregular points. For a single TiO_2 nanowire, as seen in the time range from -0.13 to -0.11 second in Fig. 5-8(b), when a current is provided, the voltage increases gradually and there is no distinct starting point when the current through sample reaches its full value. Therefore the voltage-time profile cannot be used directly to represent the resistance-time profile and to evaluate the thermal transport. In fact, the observed *U-t* profile contains conjugated information about the nonlinear response of the system and thermal transport in the nanowire. This abnormality suggests that the total current from the current source does not entirely flow through the

nanowire until certain moment. Other effects shunt the current so the current fed through the nanowire increases with time slowly before it reaches its full value. In the range from -0.08 to -0.06 second in Fig. 5-8(b), it is the decaying state and is more distinct to show the presence of unknown effects because during this stage, when the current feeding stops the voltage does not drop to zero immediately and instead it exhibits discharge-like effect, showing that there may be other current source in the circuit. This is possibly attributed to some capacitance effect generated from capacitor-like slot structure on the TEM grid as discussed later.

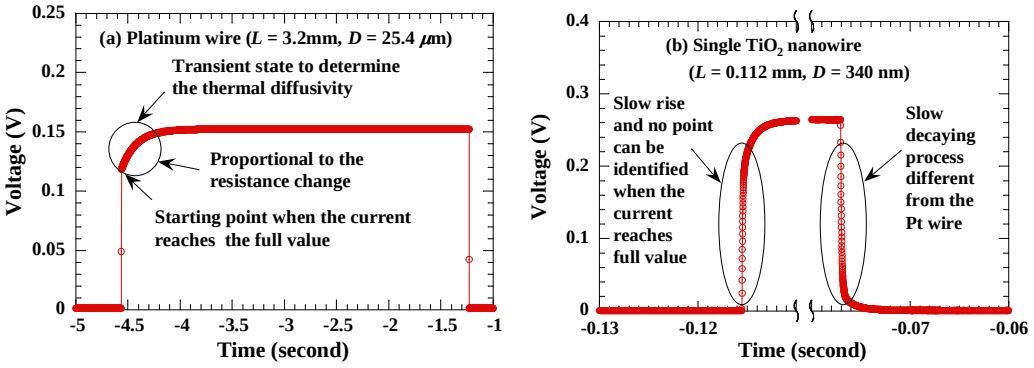

Figure 5-8. (a) Original *U-t* profiles for platinum wire, the diameter of which is 25.4 μm and (b) original *U-t* profile for single anatase TiO_2 nanowire, the diameter of which is about 340 nm, containing both rise and fall stage with irrelevant range is not shown.

5.4.1 Generalized function analysis

In order to exclude undesired effects and to acquire pure linear response, a simplified physical model is presented in Fig. 5-10(a). The whole experiment setup is generalized into a circuit in which the nanowire itself is represented by an equivalent resistor R_0 and other effects together exhibit as another parallel element (e.g., capacitor).

Based on Fig. 5-8(b), the current passing through the nanowire follows a relation $I_0 f_1(t)$, here $f_1(t)$ is a general form of time-relevant function. For example, if the capacitance effect is taken into consideration, $f_1(t)$ can be expressed as (1 - exp(-t/RC)). After detailed examination, the voltage change with time of the nanowire does not exactly fit a capacitor charging process probably because the resistance R in time constant RC is affected by other effects so it changes with time (heating effect in R_0). Therefore a generalized function analysis is exercised to exclude the unnecessary nonlinear effects by universally expressing the current as $I_0 f_1(t)$, regardless of the particular form of the nonlinear effect. Due to the heating effect introduced by the current, the resistance of the sample will change and is expressed as R_0 (1+ $f_2(Q)$), in which Q is the non-constant electrical heating proportional to square of the current passing through the nanowire, I^2. To the end, the voltage over the whole nanowire obeys Ohm's Law as

$$U = I_0 f_1(t) R_0 \left[1 + f_2(I^2)\right]. \tag{18}$$

If two different currents I_{01} and I_{02} are considered, the ratio of the induced voltages is,

$$\frac{U_1}{U_2} = \frac{I_{01} f_1(t) R_0 \left[1 + f_2(I_1^2)\right]}{I_{02} f_1(t) R_0 \left[1 + f_2(I_2^2)\right]}. \tag{19}$$

Here the non-constant heating source is known to be included within the f_2 term. During the TET measurement, the resistance change induced by electrical heating is

relatively small compared with the initial resistance. Because the generated electrical heat is linearly dependent on the square of current passing through the nanowire: $I^2 = I_0^2 f_1^2$, Eq. (17) can be simplified while ignoring the high-order terms as

$$\frac{U_1}{U_2} = \frac{I_{01}}{I_{02}}\left[1 + f_2(I_1^2 - I_2^2)\right], \tag{20}$$

in which only one term is left other than the ratio of currents. If there is no electrical heating effect, $[f_2(I_1^2 - I_2^2)]$ should be zero and only the ratio of current remains. Normally, the resistance of the sample changes because of the temperature change induced by electrical heating. In Eq. (16), the $f_1(t)$ emerges as the nonlinear factor and influences the current distribution in the whole experimental system. By applying this method to obtain Eq. (20), this nonlinear factor is constrained into a term much smaller than 1. Therefore, the ratio of voltages mostly contains impacts from heat transfer along the nanowire. For a particular TiO_2 nanowire (sample 6), two currents 6 μA and 14 μA are used and the ratio is presumed as a constant value 2.33 if no electrical heating and other effects are considered. Nevertheless, from Fig. 5-9, the ratio curve based on signals of both currents is presented. It is seen that the ratio increases very quickly from about 0.6 and then stabilizes around 2.5, implying that there could be other effect acting as time-dependent impact on the current distributed to the nanowire and this nonlinear effect takes only very small portion of the data. It proves again that the assumption to rule out small amount terms is reasonable. This ratio curve is also plotted out to be compared with the plot in Fig. 5-8(a). It is apparent that after this processing, the ratio plot features more metal-like characteristic similar to the

voltage response of Pt wire and the number of irregular points before achieving the anticipated value is also significantly less than original *U-t* profile of single anatase TiO_2 nanowire. It proves that the nonlinear effect in current evolution has been suppressed significantly as seen in Eq. (18) so that less irrelevant points are observed. Further data processing to eliminate the first several irregular points will be discussed later.

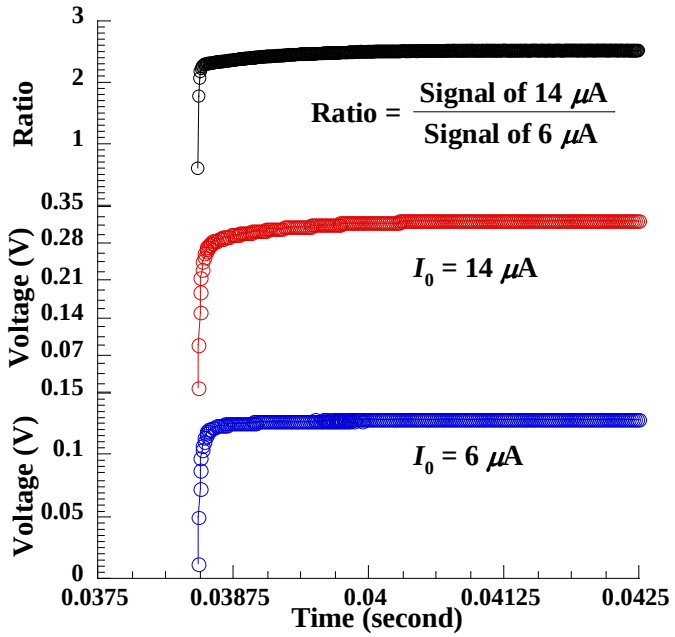

Figure 5-9. Original *U-t* profiles of two different currents: 14 μA and 6 μA and the derived ratio profile based on two voltage profiles for sample 6.

5.4.2 Direct derivation of capacitance effect and resistance profile

As discussed before, from Fig. 5-8(b), both the rise and fall state are observed to be very similar to capacitor charging and discharging behaviors. Although it has been examined that these two profiles do not exactly follow the exponential relation of typical

capacitors probably because the time constant does not stay constant due to impact from other effects (heating in the nanowire) on the capacitors. A method is developed in this section to calculate the capacitance that appears in this RC circuit (Fig. 5-10(a)) based on *U-t* profiles. A simple assumption is made that in this circuit, only the nanowire and another capacitor are connected in parallel to form a resistance-capacitance circuit and no other elements or effects are considered, as shown in Fig. 5-10(a). Therefore, the overall current passing through the capacitor and nanowire will always be constant I_0. After the current through the capacitor is obtained, the current passing through the nanowire is deduced accordingly and so is the resistance change of the nanowire. With an actual resistance-time (*R-t*) profile, the global fitting is adopted again for determining the thermal diffusivity.

According to the definition of capacitance *C*, it is relevant to the voltage between two parallel plates *U* and also the amount the charges stored *q* as $q=C \times U$. Based on the working principle of charging process of a capacitor, with the increase of voltage drop generated from the accumulated charges, the charging current gradually decreases with time and this current to charge the capacitor is expressed as $I_{charging} = C \times (dU / dt)$. In addition, without considering heating effect at the very first few moments, the resistance of the nanowire can be treated as a constant R_0 and the current *I* passing the nanowire then follows the form U/R_0. The summation of these two portions constitutes the overall current I_0 from the current source, as expressed in Eq. (21),

$$C\frac{dU}{dt}+\frac{U}{R_0}=I_0. \tag{21}$$

Due to the high resolution of the oscilloscope, first three or four data points of the voltage-time profile are applied reasonably because within such limited increase range, heating effect is negligible and the resistance is then rationally to be assumed constant. The solution to Eq. (19) is obtained as,

$$U = I_0 R_0 \left[1 - \exp(-\frac{t}{R_0 C}) \right], \tag{22}$$

with the measured values of U and t, it is not hard to use exponential fittings to determine the coefficient I_0R_0 and R_0C, and then obtain the capacitance C and initial resistance R_0. Although when voltage rises later on, the overall relation reflected by Eq. (21) is still applicable except that the resistance R does not maintain constant any more, and it is consequently calculated further based on Eq. (21) with the data from U-t profile,

$$R(t) = \frac{U}{I_0 - CdU / dt}. \tag{23}$$

Eq. (23) gives the intrinsic nanowire resistance development with time by directly fitting to derive the nonlinear capacitance effect based on the U-t profile. In order to confirm the validity of the RC circuit assumption, we calculate the capacitance of the same sample (sample 6) at different currents and different processes. With the U-t data from current 14 μA, the capacitances calculated from charging and discharging processes are 1.18 nF and 1.07 nF, respectively. Based on the voltage data under current 6 μA, the capacitance for charging process is 1.02 nF. These capacitances from different currents and

processes are very consistent to prove the rationality of the RC circuit assumption. For the same sample (sample 6) applied in the generalized analysis section, its original *U-t* profile from the oscilloscope and *R-t* profile from the above derivation method is presented in Figs. 5-10(b). In Fig. 5-10(b), the top plot is the original *U-t* profile of a gradual increase trend of voltage and it is impossible to use the *U-t* profile to obtain the resistance change. After utilizing the data analysis based on Eq. (23), the obtained resistance curve in the middle curve in Fig. 5-10(b) presents significantly improved development characteristics. This curve is very similar to the *U-t* profile of the platinum wire shown in Fig. 5-8(a) and is much more ideal to be used for global fitting to determine the thermal diffusivity. Compared with the ratio profile from the generalized analysis, the resistance curve contains less irrelevant points in rise state and demonstrates more distinct starting point to evaluate the resistance change of the nanowire.

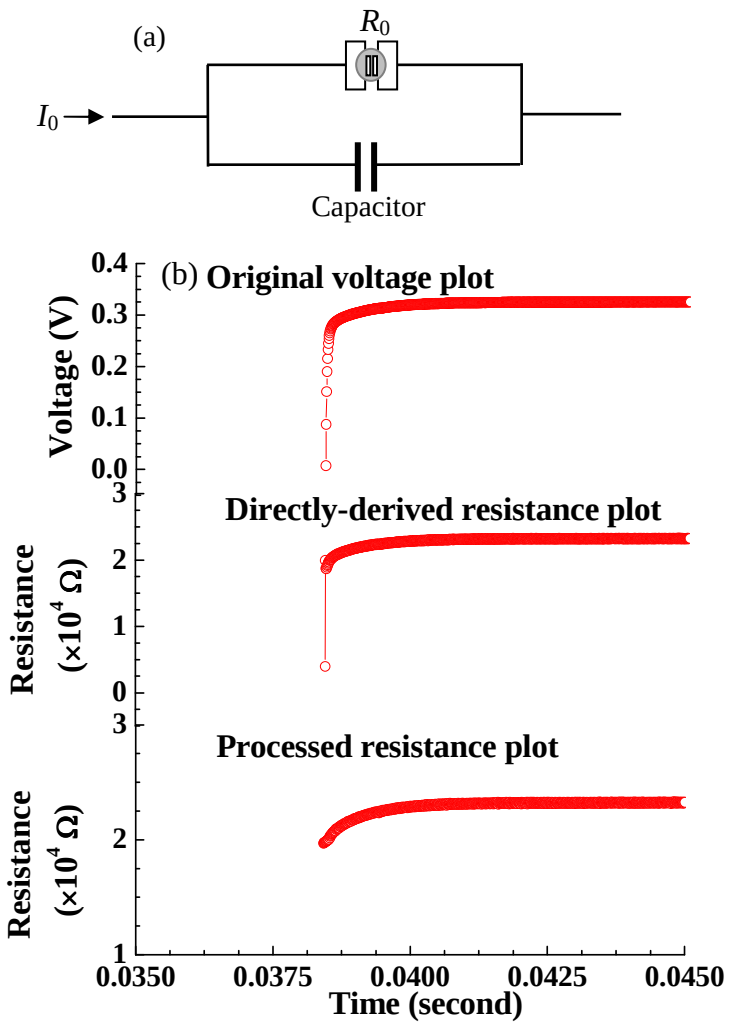

Figure 5-10. (a) Simplified RC circuit model to describe the nonlinear effect and (b) original U-t profile, derived *R-t* profile from the direct derivation before processing and the further processed *R-t* profile with modified starting points. The data is for sample 6.

However, it is further observed in the middle curve in Fig. 5-10(b) that with significantly improved resistance profile, very few abnormal points still exist, with the resistance value about 4000 and 20000 Ω. These irregular points probably are affected by conjugated electrical heating, thermal transport and probably some other unknown effects.

Although the heating effect is relatively small at the beginning, the point at 4000 Ω cannot be ignored and is instead used to explore the actual value under normal heating condition. To further process the data for better analysis, a strategy is developed by considering the linear relation between resistance variation and heating power, which is related to the square of voltage U^2. Therefore, for any initial resistance R_0, its real value is determined as,

$$R_0 = R_1 - \frac{\int_{t_0}^{t_1} U^2 dt}{\int_{t_2}^{t_3} U^2 dt} \cdot (R_3 - R_2), \tag{24}$$

in which R_1, R_2, R_3 are both known resistance values of particular points selected from the normal range when voltage rises. By using the relationship between heating power and resistance increase, the value of irregular points are further explored and the corrected resistance profile is displayed in the bottom plot in Fig. 5-10(b). Comparison between the middle curve and bottom curve in Fig. 5-10(b) explicitly demonstrates that after the processing using Eq. (24), the irregular points are eliminated and the resistance increases from a reasonable value to then follow a typical evolution tendency considering heating effect and thermal transport. This profile is the one that is directly fitted with theoretical temperature profile to acquire the thermal diffusivity. Same process is also used to correct the irregular points presented in Fig. 5-9.

5.4.3 Data processing

Based on the above methods and derived equations, further data processing can be

performed to obtain the thermal diffusivity. For the sample in Fig. 5-9, two profiles of 6 μA and 14 μA currents are used for the ratio-time profile. The ratio of signals from two different currents will attenuate unnecessary effects and contain mostly effect from heating and thermal transport, as shown also in Fig. 5-9. This ratio profile is then normalized into dimensionless form for fitting purpose. For theoretical calculation, from Eq. (1), the heat source does not stay constant because the current passing the nanowire is a varying value during the experiment. Hence, numerical simulation is employed in this work to provide theoretical data with consideration of non-constant heat source as $U^2(t)/R$. A one-dimensional scheme is employed to create the computing mesh and the governing equation (Eq. (1)) is discretized along both time and spatial dimensions. The average temperature of the whole nanowire is calculated at every time step and the temperature evolution with time is thus obtained. By normalizing the temperature variation and using different thermal diffusivity values, best fitting is identified when the error between simulated normalized temperature profile and experimental normalized ratio profile reaches the minimal level (least square method) and this value is determined as the effective thermal diffusivity of the nanowire. A comparison figure based on the generalized analysis method is displayed in Fig. 5-11. Based on the fitting, the effective thermal diffusivity of this sample is determined at 2.44×10^{-6} m^2/s. Combined with the calibration process discussed in our previous section, the thermal conductivity and density of the single TiO_2 nanowire can be determined. This method for data analysis provides a novel perspective to suppress particular forms of nonlinear effects and to maintain the linearity characteristic in experimental data, as shown

in Eq. (18). Instead of processing single a *U-t* profile, the ratio that has inherited linearity of current is more appropriate for data processing. Not only are the nonlinear effects are minimized, the impacts from long rise time of the current source can also be suppressed using data from different currents. Similarly, thermal characterization of materials with ultra-short thermal transport time can also be carried out using this method. For uncertainty analysis purpose, the thermal diffusivity is altered and related numerical fitting curves are shown to indicate that the uncertainty of this data processing is around 7%.

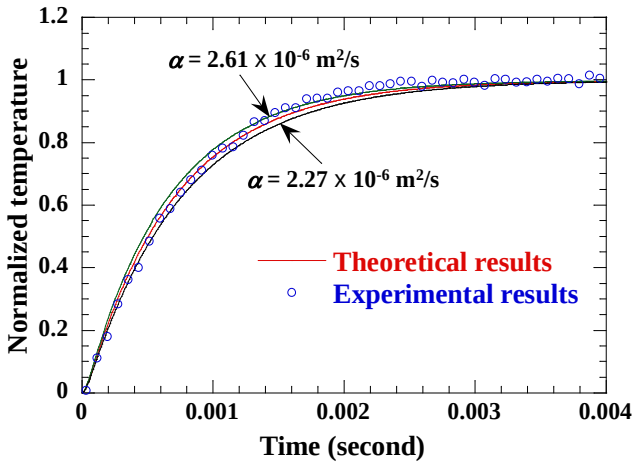

Figure 5-11. Comparison plot of theoretical results and experimental data using generalized analysis method for sample 6, along with another two profiles presenting the uncertainty of this data fitting process.

Applying the further processed resistance profile in Fig. 5-10(b) for global fitting, a fitted profile is shown in Fig. 5-12 and the determined thermal diffusivity is 2.30×10^{-6} m^2/s, while the two fittings to show that the uncertainty of global fitting is about 8%. This thermal diffusivity agrees well with that determined based on generalized analysis, 2.44×10^{-6} m^2/s, with about 6% difference. This difference arises because of several reasons. First,

during the implementation of the global fitting technique, theoretical values are calculated using the numerical simulation method as introduced in the last paragraph. However, in the generalized analysis, the heat power is expressed as $U^2(t)/R$, in which the resistance is a constant since its variation details remain unknown. In the direct derivation method, the resistance change is directly deduced under and is consequently used to calculate the heating power as $U^2(t)/R(t)$. Second, in generalized analysis, derivation of ratio data requires two sets of experimental data but only one set of data is used for fitting purpose. Selection of experimental data from different currents could introduce difference in the thermal diffusivity to certain degree. Detailed observation and comparison between Figs. 5 and 6 shows that within the time range from 0 to 4 ms, experimental results obey mainly similar trends while the results from the direct derivation method present more fluctuations and results from generalized analysis give a smoother feature. This distinction is also supported by the analytic expressions of both methods, as shown by Eq. (20) and (23). For the generalized analysis, it is clearly seen in Eq. (20) that the ratio is majorly dependent on the current I_{01} and I_{02}, and nonlinear effect is only a very small portion much less than 1. For example, this nonlinear function takes only 7% when using general analysis to acquire the ratio curve. For the direct derivation method, the nonlinear capacitance effect is fully contained to obtain the pure resistance change and thus the fluctuation contained in the data is transferred into the expression of resistance. Also in the direct derivation method, determination of the capacitance C is only based on a few points at the beginning of process.

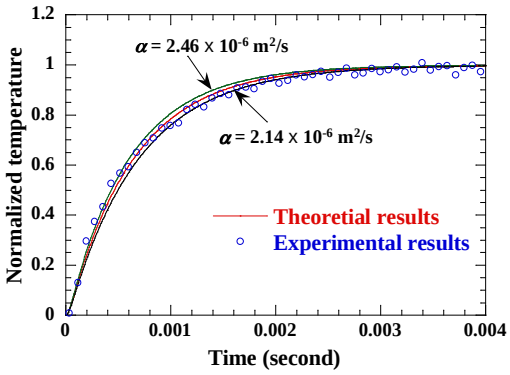

Figure 5-12. Comparison plot of theoretical results and experimental data using direct derivation method for sample 6, along with another two profiles showing the uncertainty of this data fitting process.

Table 5-2. Corresponding results calculated from generalized analysis and direct derivation methods for eight nanowire samples.

Sample	$\alpha_{1,eff}$ [a] ($\times 10^{-6}$ m^2/s)	$\alpha_{2,eff}$ [b] ($\times 10^{-6}$ m^2/s)	k_{eff} [c] (W/m·K)	$\alpha_{1,real}$ [d] ($\times 10^{-6}$ m^2/s)	$\alpha_{2,real}$ [e] ($\times 10^{-6}$ m^2/s)
1	2.94	3.27	4.17	1.30	1.45
2	2.69	2.61	2.26	1.92	1.75
3	4.94	6.62	7.25	4.18	5.61
4	5.91	5.61	6.72	4.60	4.37
5	2.01	2.01	2.42	1.51	1.40
6	2.44	2.30	4.14	2.14	2.02
7	2.14	1.71	4.09	1.65	1.19
8	2.40	2.03	5.85	1.45	1.16

[a] $\alpha_{1,eff}$: effective thermal diffusivity obtained based on the general function analysis method.

[b] $\alpha_{2,eff}$: effective thermal diffusivity obtained based on the direct derivation method.

[c] k_{eff}: effective thermal conductivity.

[d] $\alpha_{1,real}$: real thermal diffusivity obtained based on the general function analysis method.

[e] $\alpha_{2,real}$: real thermal diffusivity obtained based on the direct derivation method.

Both the generalized analysis and direct derivation prove feasible methods to rule out the nonlinear effect and to acquire pure resistance or voltage data for global fitting, as shown in Fig. 5-9 and Fig. 5-10(b). Table 5-2 lists the thermal diffusivities of all eight nanowire samples using the two methods and graphic comparison between two sets of thermal diffusivity is displayed in Fig. 5-13. The thermal diffusivities calculated by using both methods fall mainly in the range from about 2 to 6.5 × 10^{-6} m^2/s with similar distribution and only very few discrepancies are observed, suggesting that both methods are capable of excluding nonlinear effects to give more accurate thermal diffusivity. Detailed percentage of difference between the two sets of thermal diffusivity calculated from the two methods are mostly lower than 15%, except sample 3 and sample 7, the differences of which are about 25%. Considering the consistent vicinity of other data, the distinct deviations for sample 3 and 7 may be attributed to particular disturbances included in the preparation procedure. Except these two value sets, other data demonstrated high agreement. Further examination reveals that the thermal diffusivities from direct derivation are mostly a little lower than those from generalized analysis while exceptions are identified for sample 1 and 3. This difference is analyzed before and is caused by several reasons, such as different consideration of heat source, different selection of experimental data and different simplifications made to derive the capacitance. In addition, distinct basis of the two methods is also accountable. For generalized analysis, due to the unknown factors of nonlinear effects, an expression from Ohm's Law is applied by simplifying those effects into a general function form f_1 regardless of any particular effects. For direct

derivation, assumptions are made that the whole setup is a simple RC circuit and at the very beginning electrical heating effect is negligible thus the resistance is treated a constant. Under these circumstances, direct derivation presents higher quantitative accuracy although its utilization requires more strictly examined conditions. On the other hand, the generalized analysis presents higher adaptability to a variety of conditions. For instance, because it concerns much less about the time-related effects, it can be used to handle samples with faster thermal response time or current source with relatively long rise time.

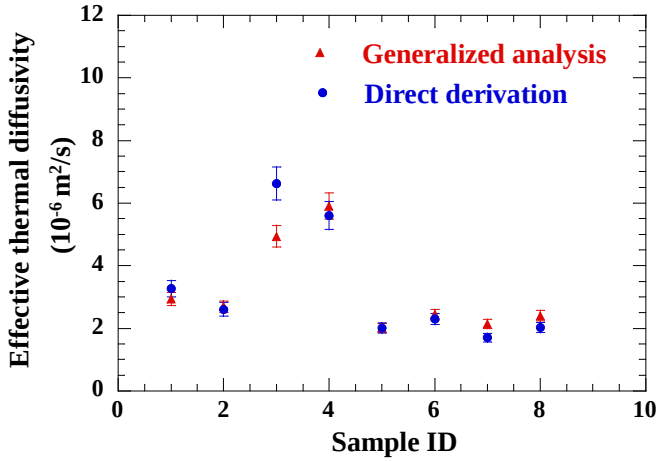

Figure 5-13. Effective thermal diffusivities calculated from two methods for all nanowire samples.

The thermal diffusivity obtained so far is all effective values, meaning that the impact from iridium coating is still included. Based on the nature of the coating, the overall effective thermal diffusivity is assumed to be a superposition of the thermal diffusivity of both TiO_2 nanowire and iridium film. Additionally, Wiedemann-Franz law is applied to interpret the influence of iridium coating because that its thermal and electrical properties

are known already. The consequence is the Lorenz number of iridium is then imported to derive the real thermal diffusivity of pure TiO_2 nanowire. With derived effective thermal conductivity [26], overall effective volume-based specific heat is obtained as $C_{eff} = \rho c_p = k_{eff} / \alpha_{eff}$. Then the real thermal diffusivity is expressed as $\alpha_{real} = \alpha_{eff} - (L_{\text{Lorenz}} TL/RA_w C_{eff})$, in which L and A_w are length and cross-sectional area of the nanowire, R is the resistance and T is the temperature. With this expression, the impact from iridium coating is consequently eliminated and thermal diffusivity of pure TiO_2 nanowire is obtained, as those listed in Table 5-2.

CHAPTER 6. CONCLUSION

As can be seen in this work, the thermophysical properties study of micro/nanoscale materials is a complicated and delicate process, combining knowledge from sample preparation, structure diagnosis, heat transfer study and data analysis. Samples have to been fabricated so that controllable thermal energy could be excited along particular direction or at specific locations. Precise design of experimental apparatus and selection of source of thermal excitation better helps to achieve this goal. For example, in this work, temperature rise is induced by either electricity (TET) or laser beam (PLTR). Electricity source is easy to control and to quantify, by proving accurate value of the heat flux. Compared with the electricity, laser beam is more suitable if a localized temperature increase is needed. In addition, as an ultrafast heat source, PLTR can also be applied to study ultrafast thermal transport phenomenon. After inducing desired temperature distribution, proper probing technique is required to sense the temperature change and the choice of probing technique is strongly dependent on the material and its geometry. Both TET and PLTRs techniques implement the electricity to sense the temperature (steady or transient response). In the development of the techniques to characterize micro/nanoscale thermal transport, simplicity is of paramount importance. Complicated system inevitably brings in more uncertainties and factors that need to be considered. Therefore, for both TET and PLTR2 technique, the setup is kept simple so that appropriate assumptions are made to ensure the feasibility of analytical solutions. Even so, many unnecessary effects and factors are observed for the measurement and the results, For example, the nonlinear effects within the characterization

of TiO_2 nanowires. Approaches are developed to eliminate the nonlinear effects based on the original data. However, some other factors from the scientific equipment, the measurement of dimensions and others may not be able to be completely excluded and will contribute to the accumulated uncertainty in the techniques. Therefore, an in-depth understanding of the thermal transport and proper assumption are both required for the characterization of micro/nanoscale materials, otherwise, anomalous results could be induced.

6.1 Thin films

Two different types of thin films were fabricated and studied using various techniques. As a typical conducting polymer, P3HT thin films were fabricated using spin coating technique from solution of different P3HT weight percentages: 2%, 3%, 5% and 7%. The TET technique combined with a temperature-resistance calibration procedure was employed to determine the thermophysical properties. P3HT solution of different weight percentages in fabrication contributed to different physical properties, such as thickness and density. The thickness of spin-coated P3HT thin film was tens of micrometers and the density varies from 878 to 1640 kg/m^3. Considering the included measurement uncertainty, average thickness and density at each solution weight percentage were positively affected by the P3HT solution weight percentage. The thermophysical properties were also influenced by the P3HT solution weight percentage and density. The thermal diffusivity decreased from 1.03×10^{-6} to 5.75×10^{-7} m^2/s with increasing P3HT solution weight

percentage while the thermal conductivity presented only moderate influence from the P3HT solution weight percentage. Compared with P3HT solution weight percentage, the final film density is a more representative parameter to study the variation of thermal diffusivity and thermal conductivity. The film thermal conductivity increased with density while the thermal diffusivity decreased. The thermal diffusivity decrease demonstrated the effect of density on storing energy is more than that on increasing thermal conductivity.

Because spin coating technique can induce strong anisotropy with crystal structure, which consequently leads to anisotropy with mechanical/thermal properties, P3HT thin films fabricated using spin coating were also investigated for the anisotropic thermal transport. Raman spectroscopy diagnosis showed that the spin-coated P3HT thin films in this work embrace aligned molecular chains and present strong anisotropy within the crystal structure. By referring to the orientation of the aligned P3HT molecular chains, a 3-dimensional characterization system was created to distinguish the thermal transport along three distinct directions: parallel to orientation (P), in-plane perpendicular to orientation ($\perp, in$) and out-of-plane perpendicular to orientation ($\perp, out$). PLTR2 technique, which is capable of studying both in-plane and out-of-plane direction thermal transport, was employed for 3-dimensional characterization of thermophysical properties. As a validation of results from PLTR2 technique, TET technique was also used. Thickness of spin-coated P3HT thin film varied from 10 to 35 □m. Thermal conductivity and thermal diffusivity both presented strong anisotropy based on the orientation of molecular chains. For thermal

conductivity, the anisotropy factor was about 2 to 3, lower than polymer films that comprise perfectly aligned molecular chains. This anisotropy with thermal conductivity generates from the anisotropy with crystal structure. Strong covalent bonding within the molecular chain strengthens the phonon transport while the interactions among the chains are much weaker. For thermal diffusivity, same anisotropy with thermal transport is also supported by measured results. Along out-of-plane direction, thermal diffusivity was observed to be around 1 to 2 × 10^{-7} m^2/s and thermal conductivity was just about 0.2 W/m·K, almost one order of magnitude lower than the other two directions. It is because the spin coating process squeezes the curved molecular chains into a thin layer of just a few microns and there are very few interactions among the chains along thickness direction. Density of P3HT films was also deduced based on the definition of thermal diffusivity and is much lower than the literature value, due to the highly porous structure caused by spin coating process.

Other than polymer materials, as an excellent candidate for photocatalytic effect, TiO_2 thin films of thickness around 60 μm were fabricated using electrospinning technique and interior interconnected TiO_2 nanowires was confirmed by AFM images. Raman spectrum indicated that it is the anatase polymorph of TiO_2 after annealing at 500ºC. The TET technique was adopted to provide a full spectrum measurement of the film thermal diffusivity, density, and thermal conductivity. The obtained effective thermal conductivity ranges from 0.06 to 0.36 W/m·K while the effective density changes from 25.8 to 373

kg/m^3, significantly lower than reported bulk value because of the disordered and loose crystalline structure nature of the sample films. It means bulk values may not be appropriate in the design of thin optical films. With the density increase, the thermal conductivity presented an ascending profile showing that the thermal conductivity of thin film is strongly influenced by the density. A physical model was developed to estimate the intrinsic thermal conductivity of TiO_2 nanowires based on the measured thermal properties of the thin films. The calculated intrinsic thermal conductivity (4.67~12.2 W/m·K) of TiO_2 nanowires varies within a range one order of magnitude higher than that of the thin film, and is acceptably comparable to the value of bulk material 8.5 W/m·K considering the uncertainty introduced into the model and experiment. A calculation of mean free path based on the intrinsic thermal conductivity of TiO_2 nanowires demonstrates that the nanowire size has negligible impact on the phonon transport and the major restriction on the heat transfer originated from the crystalline structure defect.

Although thin films in this chapter have similar appearance, their internal structure features totally diverse nature. The TiO_2 thin film embraces internal network of interconnected TiO_2 nanowires and high porosity is observed from Fig. 4-2. Phonon transport is highly impacted by the scattering with the vacancies and imperfections; therefore the determined thermal conductivity is significantly lower than bulk value of its counterpart. On the other hand, for P3HT film, spin-coating process has strongly spread the P3HT solution drops into extremely thin layer and distinct thermal property anisotropy is

observed. In addition, the thermal conductivity from P3HT thin films is close to or even higher than that of regular polymer materials, indicating that the phonon transport in P3HT suffers less influence from vacancies scattering compared with TiO_2 films. The reason why its thermal conductivity is slightly higher than regular organic materials is probably because the P3HT presents certain electrical conducting property compared with other non-conductive organic materials.

6.2 Nanowire

Based on the study of TiO_2 thin films, single TiO_2 nanowire, which is considered to be the intrinsic unit composing TiO_2 nanofilm and nanowire array, was exclusively studied. High-oriented and aligned TiO_2 nanowires were firstly fabricated by electrospinning and then collected over a pre-processed TEM grid. After hydrolysis and calcination, only one TiO_2 nanowire was particularly picked for followed characterization process. Raman spectra indicate that the obtained single TiO_2 nanowire is of anatase polymorph. SEM images verify that the calcination in which both decomposition of PVP content and transition of TiO_2 crystalline structure happen strongly distorts the fibrous structure and induces obvious aggregation of TiO_2 particles, consequently resulting in secondary porous structure. This porosity is further confirmed by results from thermal characterization procedure. Via TET characterization, the obtained thermal conductivity varies from 1.38 to 6.01 W/m·K while the effective density changes from about 1155 kg/m^3 to 2830 kg/m^3, significantly lower than reported bulk value because the structural distortions and

imperfections strongly hampers the phonon transport. With the density increase, thermal conductivity and thermal diffusivity slightly presented corresponding varying tendency. With the density, an overall porosity of the nanowire can be estimated. For all samples in this chapter, the highest porosity is less than 73%, showing that the crystal structure contains vacancies and spacing and are looser than ideal bulk material. The diameter of the nanowire was also investigated to understand its relationship with thermal properties. The changing range of the diameter is very limited, from 250 to 380 nm. Within this small variance, thermal conductivity and thermal diffusivity simply show certain fluctuation with moderate trends. Density changes more strongly with the diameter, indicating that when diameter varies, the level of vacancies and irregularity may be affected significantly. An error analysis is given to show the accuracy of this experiment in measuring the thermophysical properties and it is demonstrated that errors related to all parameters are controlled within acceptable ranges considering various uncertainties in the experiment.

Due the complexity existed with the sample preparation, time-dependent nonlinear effects are observed within the recorded voltage-time profiles. This nonlinear effect is expected to be related to capacitance and the current is shunted that the current going through the sample varies with time. This nonlinear effect has caused that the *U-t* profile recorded over the sample cannot be used for data analysis directly because the exact time when the current reached a full value was obscure. Two quantitative methods were developed to exclude the nonlinear effects to assist accurate derivation of thermal

properties. Generalized function analysis made use of two signals and constrained the nonlinear time-dependent effect into a small term. The direct capacitance derivation presumed that the whole setup to be a simple RC circuit and the directly derived the resistance change against time. Thermal diffusivities determined using the two methods are in ideal agreement with each other in of 2 to 6 × 10^{-6} m^2/s while small difference was observed due to the distinct principle differences between these methods. The uncertainty of this fitting was also studied by altering the value of thermal diffusivity to identify significant difference in global data fitting. Compared to the direct derivation method, the generalized analysis is more applicable to situations that a current source has relatively long rise time or the material has relatively fast thermal response.

REFERENCES

[1] Xia, Y. N., Yang, P. D., Sun, Y. G., Wu, Y. Y., Mayers, B., Gates, B., Yin, Y. D., Kim, F. and Yan, Y. Q., One-Dimensional Nanostructures: Synthesis, Characterization, and Applications. *Adv Mater* **15**, 353 (2003).

[2] Goodson, K. E. and Ju, Y. S., Heat Conduction in Novel Electronic Films. *Annu Rev Mater Sci* **29**, 261 (1999).

[3] Cahill, D. G., Fischer, H. E., Klitsner, T., Swartz, E. T. and Pohl, R. O., Thermal-Conductivity of Thin-Films - Measurements and Understanding. *Journal of Vacuum Science & Technology a-Vacuum Surfaces and Films* **7**, 1259 (1989).

[4] Swartz, E. T. and Pohl, R. O., Thermal-Resistance at Interfaces. *Appl Phys Lett* **51**, 2200 (1987).

[5] Goodson, K. E., Flik, M. I., Su, L. T. and Antoniadis, D. A., Prediction and Measurement of the Thermal-Conductivity of Amorphous Dielectric Layers. *J Heat Trans-T Asme* **116**, 317 (1994).

[6] Lee, S. M. and Cahill, D. G., Heat Transport in Thin Dielectric Films. *J Appl Phys* **81**, 2590 (1997).

[7] Roncali, J., Conjugated Poly(Thiophenes) - Synthesis, Functionalization, and Applications. *Chem Rev* **92**, 711 (1992).

[8] Chen, T. A. and Rieke, R. D., The 1st Regioregular Head-to-Tail Poly(3-Hexylthiophene-2,5-Diyl) and a Regiorandom Isopolymer - Ni Vs Pd Catalysis of

2(5)-Bromo-5(2)-(Bromozincio)-3-Hexylthiophene Polymerization. *J Am Chem Soc* **114**, 10087 (1992).

[9] Chen, T. A., Wu, X. M. and Rieke, R. D., Regiocontrolled Synthesis of Poly(3-Alkylthiophenes) Mediated by Rieke Zinc - Their Characterization and Solid-State Properties. *J Am Chem Soc* **117**, 233 (1995).

[10] Loewe, R. S., Khersonsky, S. M. and McCullough, R. D., A Simple Method to Prepare Head-to-Tail Coupled, Regioregular Poly(3-Alkylthiophenes) Using Grignard Metathesis. *Adv Mater* **11**, 250 (1999).

[11] Sheina, E. E., Liu, J. S., Iovu, M. C., Laird, D. W. and McCullough, R. D., Chain Growth Mechanism for Regioregular Nickel-Initiated Cross-Coupling Polymerizations. *Macromolecules* **37**, 3526 (2004).

[12] Yokoyama, A., Miyakoshi, R. and Yokozawa, T., Chain-Growth Polymerization for Poly(3-Hexylthiophene) with a Defined Molecular Weight and a Low Polydispersity. *Macromolecules* **37**, 1169 (2004).

[13] Yokoyama, A., Kato, A., Miyakoshi, R. and Yokozawa, T., Precision Synthesis of Poly (N-Hexylpyrrole) and Its Diblock Copolymer with Poly(P-Phenylene) Via Catalyst-Transfer Polycondensation. *Macromolecules* **41**, 7271 (2008).

[14] Erwin, M. M., McBride, J., Kadavanich, A. V. and Rosenthal, S. J., Effects of Impurities on the Optical Properties of Poly-3-Hexylthiophene Thin Films. *Thin Solid Films* **409**, 198 (2002).

[15] Hugger, S., Thomann, R., Heinzel, T. and Thurn-Albrecht, T., Semicrystalline Morphology in Thin Films of Poly(3-Hexylthiophene). *Colloid Polym Sci* **282**, 932 (2004).

[16] Kim, D. H., Park, Y. D., Jang, Y., Kim, S. and Cho, K., Solvent Vapor-Induced Nanowire Formation in Poly(3-Hexylthiophene) Thin Films. *Macromol Rapid Comm* **26**, 834 (2005).

[17] Esenturk, O., Melinger, J. S. and Heilweil, E. J., Intrinsic Photoconductivity of P3HT Films Measured by Time-Resolved Thz Spectroscopy. *2007 Conference on Lasers & Electro-Optics/Quantum Electronics and Laser Science Conference (Cleo/Qels 2007), Vols 1-5* 2743 (2007).

[18] Janssen, G., Aguirre, A., Goovaerts, E., Vanlaeke, P., Poortmans, J. and Manca, J., Optimization of Morphology of P3HT /PCBM Films for Organic Solar Cells: Effects of Thermal Treatments and Spin Coating Solvents. *Eur Phys J-Appl Phys* **37**, 287 (2007).

[19] Khaliq, A., Xue, F. L. and Varahramyan, K., Numerical Simulation of Spin Coated P3HT Organic Thin Film Transistors with Field Dependent Mobility and Distributed Contact Resistance. *Microelectron Eng* **86**, 2312 (2009).

[20] Scavia, G., Porzio, W., Destri, S., Schieroni, A. G. and Bertini, F., Morphology and Orientation of Thin Poly(3-Hexylthiophene) (P3HT) Films on Differently Silanized Silicon Oxide. *E-Polymers* 1 (2009).

[21] Gonzalez, R. a. P., N, Electrospun P3HT Fiber Filed Effect Transistor. *Synthetic Met* **151**, 275 (2005).

[22] Kim, D. H., Han, J. T., Park, Y. D., Jang, Y., Cho, J. H., Hwang, M. and Cho, K., Single-Crystal Polythiophene Microwires Grown by Self-Assembly. *Adv Mater* **18**, 719 (2006).

[23] Savenije, T. J., Kroeze, J. E., Yang, X. N. and Loos, J., The Formation of Crystalline P3HT Fibrils Upon Annealing of a Pcbm : P3HT Bulk Heterojunction. *Thin Solid Films* **511**, 2 (2006).

[24] Laforgue, A. and Robitaille, L., Fabrication of Poly-3-Hexylthiophene/Polyethylene Oxide Nanofibers Using Electrospinning. *Synthetic Met* **158**, 577 (2008).

[25] Kuo, C. C., Wang, C. T. and Chen, W. C., Poly(3-Hexylthiophene)/Poly(Methyl Methacrylate) Core-Shell Electrospun Fibers for Sensory Applications. *Macromol Symp* **279**, 41 (2009).

[26] Lee, S., Moon, G. D. and Jeong, U., Continuous Production of Uniform Poly(3-Hexylthiophene) (P3HT) Nanofibers by Electrospinning and Their Electrical Properties. *J Mater Chem* **19**, 743 (2009).

[27] Pinto, N. J., Carrasquillo, K. V., Rodd, C. M. and Agarwal, R., Rectifying Junctions of Tin Oxide and Poly(3-Hexylthiophene) Nanofibers Fabricated Via Electrospinning. *Appl Phys Lett* **94**, 083504 (2009).

[28] Lee, S. W., Lee, H. J., Choi, J. H., Koh, W. G., Myoung, J. M., Hur, J. H., Park, J. J., Cho, J. H. and Jeong, U., Periodic Array of Polyelectrolyte-Gated Organic

Transistors from Electrospun Poly(3-Hexylthiophene) Nanofibers. *Nano Lett* **10**, 347 (2010).

[29] Zhao, K., Xue, L. J., Liu, J. G., Gao, X., Wu, S. P., Han, Y. C. and Geng, Y. H., A New Method to Improve Poly(3-Hexyl Thiophene) (P3HT) Crystalline Behavior: Decreasing Chains Entanglement to Promote Order-Disorder Transformation in Solution. *Langmuir* **26**, 471 (2010).

[30] Northrup, J. E., Atomic and Electronic Structure of Polymer Organic Semiconductors: P3HT, PQT, and PBTTT. *Phys Rev B* **76**, 245202 (2007).

[31] Roy, D., Tripathi, N. K., Saraiya, A. and Ram, K., Modification of Conductivity of P3HT by Addition of Endometallo Fullerene. *J Appl Polym Sci* **114**, 491 (2009).

[32] Kim, H., So, W. W. and Moon, S. J., Effect of Thermal Annealing on the Performance of P3HT/Pcbm Polymer Photovoltaic Cells. *J Korean Phys Soc* **48**, 441 (2006).

[33] Henning, J., Anisotropy and Structure in Uniaxially Stretched Amorphous High Polymers. *J. Polym. Sci. C* **16**, 2751 (1967).

[34] Hansen, D. and Ho, C. C., Thermal Conductivity of High Polymers. *Journal of Polymer Science Part A: General Papers* **3**, 659 (1965).

[35] Choy, C., Thermal Conductivity of Polymers. *Polymer* **18**, 984 (1977).

[36] Kilian, H. G. and Pietralla, M., Anisotropy of Thermal-Diffusivity of Uniaxial Stretched Polyethylenes. *Polymer* **19**, 664 (1978).

[37] Rantala, J., A Measurement Method for the Determination of the Anisotropy Ratio of Thermal-Conductivity of Plastic Foils. *Review of Scientific Instruments* **63**, 5472 (1992).

[38] Piraux, L., Kinanyalaoui, M., Issi, J. P., Begin, D. and Billaud, D., Thermal-Conductivity of an Oriented Polyacetylene Film. *Solid State Commun* **70**, 427 (1989).

[39] Choy, C. L., Yang, G. W. and Wong, Y. W., Thermal Diffusivity of Polymer Films by Pulsed Photothermal Radiometry. *J Polym Sci Pol Phys* **35**, 1621 (1997).

[40] Kurabayashi, K., Asheghi, M., Touzelbaev, M. and Goodson, K. E., Measurement of the Thermal Conductivity Anisotropy in Polyimide Films. *J Microelectromech S* **8**, 180 (1999).

[41] Ju, Y. S., Kurabayashi, K. and Goodson, K. E., Thermal Characterization of Ic Passivation Layers Using Joule Heating and Optical Thermometry. *Microscale Therm Eng* **2**, 101 (1998).

[42] Ju, Y. S., Kurabayashi, K. and Goodson, K. E., Thermal Characterization of Anisotropic Thin Dielectric Films Using Harmonic Joule Heating. *Thin Solid Films* **339**, 160 (1999).

[43] Liu, C. J., Oshima, K., Shimomura, M. and Miyauchi, S., Anisotropic Conductivity-Temperature Characteristic of Solution-Cast Poly(3-Hexylthiophene) Films. *Synthetic Met* **156**, 1362 (2006).

[44] Maizel, K., Ezzahri, Y., Wang, X., Singer, S., Majumdar, A. and Shakouri, A., Measurement of Thin Film Isotropic and Anisotropic Thermal Conductivity Using 3 Omega and Thermoreflectance Imaging. *Twenty Fourth Annual Ieee Semiconductor Thermal Measurement and Management Symposium, Proceedings 2008* 187 (2008).

[45] Guo, J. Q., Wang, X. W., Geohegan, D. B., Eres, G. and Vincent, C., Development of Pulsed Laser-Assisted Thermal Relaxation Technique for Thermal Characterization of Microscale Wires. *J Appl Phys* **103**, 113505 (2008).

[46] Feng, X., Wang, X., Chen, X. and Yue, Y., Thermo-Physical Properties of Thin Films Composed of Anatase TiO_2 Nanofibers. *Acta Mater* **59**, 1934 (2011).

[47] Feng, X. H. and Wang, X. W., Thermophysical Properties of Free-Standing Micrometer-Thick Poly (3-Hexylthiophene) Films. *Thin Solid Films* **519**, 5700 (2011).

[48] Dagan, G. and Tomkiewicz, M., TiO_2 Aerogels for Photocatalytic Decontamination of Aquatic Environments. *J Phys Chem-Us* **97**, 12651 (1993).

[49] Azad, A. M., Akbar, S. A., Younkman, L. B. and Alim, M. A., High-Temperature Immittance Response in Anatase-Based Sensor Materials. *J Am Ceram Soc* **77**, 3145 (1994).

[50] Azad, A. M., Younkman, L. B., Akbar, S. A. and Alim, M. A., Characterization of TiO_2-Based Sensor Materials Using Immittance Spectroscopy. *J Am Ceram Soc* **77**, 481 (1994).

[51] Bach, U., Lupo, D., Comte, P., Moser, J. E., Weissortel, F., Salbeck, J., Spreitzer, H. and Gratzel, M., Solid-State Dye-Sensitized Mesoporous TiO_2 Solar Cells with High Photon-to-Electron Conversion Efficiencies. *Nature* **395**, 583 (1998).

[52] Gratzel, M., Photoelectrochemical Cells. *Nature* **414**, 338 (2001).

[53] Melendres, C. A., Narayanasamy, A., Maroni, V. A. and Siegel, R. W., Raman-Spectroscopy of Nanophase TiO_2. *J Mater Res* **4**, 1246 (1989).

[54] Terwilliger, C. D. and Chiang, Y. M., Excess Thermodynamic Properties of Nanophase Titanium-Dioxide Prepared by Chemical and Physical Methods. *Mat Res S C* **286**, 15 (1993).

[55] Lei, Y., Zhang, L. D., Meng, G. W., Li, G. H., Zhang, X. Y., Liang, C. H., Chen, W. and Wang, S. X., Preparation and Photoluminescence of Highly Ordered TiO_2 Nanowire Arrays. *Appl Phys Lett* **78**, 1125 (2001).

[56] Lin, Y., Wu, G. S., Yuan, X. Y., Xie, T. and Zhang, L. D., Fabrication and Optical Properties of TiO_2 Nanowire Arrays Made by Sol-Gel Electrophoresis Deposition into Anodic Alumina Membranes. *J Phys-Condens Mat* **15**, 2917 (2003).

[57] Miao, L., Tanemura, S., Toh, S., Kaneko, K. and Tanemura, M., Heating-Sol-Gel Template Process for the Growth of TiO_2 Nanorods with Rutile and Anatase Structure. *Appl Surf Sci* **238**, 175 (2004).

[58] Miao, L., Tanemura, S., Toh, S., Kaneko, K. and Tanemura, M., Fabrication, Characterization and Raman Study of Anatase TiO_2 Nanorods by a Heating-Sol-Gel Template Process. *J Cryst Growth* **264**, 246 (2004).

[59] Jung, K. Y. and Park, S. B., Anatase-Phase Titania: Preparation by Embedding Silica and Photocatalytic Activity for the Decomposition of Trichloroethylene. *J Photoch Photobio A* **127**, 117 (1999).

[60] Jung, K. Y. and Park, S. B., Enhanced Photoactivity of Silica-Embedded Titania Particles Prepared by Sol-Gel Process for the Decomposition of Trichloroethylene. *Appl Catal B-Environ* **25**, 249 (2000).

[61] De Farias, R. F., Silva, C. C. G. and Restivo, T. A. G., Thermal Study of the Anatase-Rutile Structural Transitions in Sol-Gel Synthesized Titanium Dioxide Powders. *J Serb Chem Soc* **70**, 675 (2005).

[62] Hoffmann, P., Halary, E., Benvenuti, G. and Wagner, F., Light Induced Chemical Vapour Deposition of Titanium Oxide Thin Films at Room Temperature. *Appl Surf Sci* **154**, 146 (2000).

[63] Maekawa, T., Kurosaki, K., Tanaka, T. and Yamanaka, S., Thermal Conductivity of Titanium Dioxide Films Grown by Metal-Organic Chemical Vapor Deposition. *Surf Coat Tech* **202**, 3067 (2008).

[64] Yuan, Z. Y. and Su, B. L., Titanium Oxide Nanotubes, Nanofibers and Nanowires. *Colloid Surface A* **241**, 173 (2004).

[65] Francioso, L. and Siciliano, P., Top-Down Contact Lithography Fabrication of a TiO_2 Nanowire Array over a Sio2 Mesa. *Nanotechnology* **17**, 3761 (2006).

[66] Kolen'ko, Y. V., Kovnir, K. A., Gavrilov, A. I., Garshev, A. V., Frantti, J., Lebedev, O. I., Churagulov, B. R., Van Tendeloo, G. and Yoshimura, M., Hydrothermal

Synthesis and Characterization of Nanorods of Various Titanates and Titanium Dioxide. *J Phys Chem B* **110**, 4030 (2006).

[67] Zhang, X. W., Pan, J. H., Du, A. J., Fu, W. J., Sun, D. D. and Leckie, J. O., Combination of One-Dimensional TiO_2 Nanowire Photocatalytic Oxidation with Microfiltration for Water Treatment. *Water Res* **43**, 1179 (2009).

[68] Ge, Z. X., Wei, A. X., Liu, J., Zhao, W. and Liu, C. B., Synthesis and Photovoltaic Devices Performance of Single Crystalline TiO_2 Nanowire Bundle Arrays. *J Inorg Mater* **25**, 1105 (2010).

[69] Liao, J. Y., Lei, B. X., Wang, Y. F., Liu, J. M., Su, C. Y. and Kuang, D. B., Hydrothermal Fabrication of Quasi-One-Dimensional Single-Crystalline Anatase TiO_2 Nanostructures on Fto Glass and Their Applications in Dye-Sensitized Solar Cells. *Chem-Eur J* **17**, 1352 (2011).

[70] Xu, Y., Gu, H. S., Xia, H. T. and Hu, M. Z., TiO_2 Nanowire Dye-Sensitized Solar Cells Fabricated by Hydrothermal Method. *3rd International Photonics and Optoelectronics Meetings (Poem 2010)* **276**, (2011).

[71] Lei, Y., Zhang, L. D. and Fan, J. C., Fabrication, Characterization and Raman Study of TiO_2 Nanowire Arrays Prepared by Anodic Oxidative Hydrolysis of Ticl3. *Chem Phys Lett* **338**, 231 (2001).

[72] Zhang, X. Y., Yao, B. D., Zhao, L. X., Liang, C. H., Zhang, L. D. and Mao, Y. Q., Electrochemical Fabrication of Single-Crystalline Anatase TiO_2 Nanowire Arrays. *J Electrochem Soc* **148**, G398 (2001).

[73] Jiao, Z., Wu, M. H., Shi, L. Y., Li, Z. and Wang, Y. L., Preparation of TiO_2 Nanowire by Atomic Force Microscopy Electrochemical Anode Oxidation. *Chinese J Inorg Chem* **20**, 1325 (2004).

[74] Liu, S. Q. and Huang, K. L., Straightforward Fabrication of Highly Ordered TiO_2 Nanowire Arrays in Aam on Aluminum Substrate. *Sol Energ Mat Sol C* **85**, 125 (2005).

[75] Cai, F. G., Yang, F., Zhao, Y. and Cheng, C. H., Preparation of TiO_2 Nanotube and Nanotube/Nanowire Composite Arrays by Temperature Control. *Chinese J Inorg Chem* **27**, 504 (2011).

[76] Li, D. and Xia, Y. N., Fabrication of Titania Nanofibers by Electrospinning. *Nano Lett* **3**, 555 (2003).

[77] Subbiah, T., Bhat, G. S., Tock, R. W., Pararneswaran, S. and Ramkumar, S. S., Electrospinning of Nanofibers. *J Appl Polym Sci* **96**, 557 (2005).

[78] Son, W. K., Cho, D. and Park, W. H., Direct Electrospinning of Ultrafine Titania Fibres in the Absence of Polymer Additives and Formation of Pure Anatase Titania Fibres at Low Temperature. *Nanotechnology* **17**, 439 (2006).

[79] Tekmen, C., Suslu, A. and Cocen, U., Titania Nanofibers Prepared by Electrospinning. *Mater Lett* **62**, 4470 (2008).

[80] Zhao, J. G., Jia, C. W., Duan, H. G., Li, H. and Xie, E. Q., Structural Properties and Photoluminescence of TiO_2 Nanofibers Were Fabricated by Electrospinning. *J Alloy Compd* **461**, 447 (2008).

[81] Li, D., Wang, Y. L. and Xia, Y. N., Electrospinning of Polymeric and Ceramic Nanofibers as Uniaxially Aligned Arrays. *Nano Lett* **3**, 1167 (2003).

[82] Zhu, R., Jiang, C. Y., Liu, X. Z., Liu, B., Kumar, A. and Ramakrishna, S., Improved Adhesion of Interconnected TiO_2 Nanofiber Network on Conductive Substrate and Its Application in Polymer Photovoltaic Devices. *Appl Phys Lett* **93**, 013102 (2008).

[83] Lozzi, L., Rinaldi, M., Ruggieri, F. and Santucci, S., Well-Aligned Tio(2) Nanofibers Grown by near-Field-Electrospinning. *J Vac Sci Technol B* **27**, 1829 (2009).

[84] Chung, Y. A., Lee, C. Y., Peng, C. W. and Chiu, H. T., Reactive Template Assisted Growth of One-Dimensional Nanostructures of Titanium Dioxide. *Mater Chem Phys* **100**, 380 (2006).

[85] Venkataramanan, N. S., Matsui, K., Kawanami, H. and Ikushima, Y., Green Synthesis of Titania Nanowire Composites on Natural Cellulose Fibers. *Green Chem* **9**, 18 (2007).

[86] Baik, J. M., Kim, M. H., Larson, C., Chen, X. H., Guo, S. J., Wodtke, A. M. and Moskovits, M., High-Yield TiO_2 Nanowire Synthesis and Single Nanowire Field-Effect Transistor Fabrication. *Appl Phys Lett* **92**, 242111 (2008).

[87] Kim, J. I., Lee, S. Y. and Pyun, J. C., Characterization of Photocatalytic Activity of TiO_2 Nanowire Synthesized from Ti-Plate by Wet Corrosion Process. *Curr Appl Phys* **9**, E252 (2009).

[88] Park, J., Ryu, Y., Kim, H. and Yu, C., Simple and Fast Annealing Synthesis of Titanium Dioxide Nanostructures and Morphology Transformation During Annealing Processes. *Nanotechnology* **20**, 105608 (2009).

[89] Inoue, Y., Noda, I., Torikai, T., Watari, T., Hotokebuchi, T. and Yada, M., TiO_2 Nanotube, Nanowire, and Rhomboid-Shaped Particle Thin Films Fixed on a Titanium Metal Plate. *J Solid State Chem* **183**, 57 (2010).

[90] Kim, M. H., Baik, J. M., Zhang, J. P., Larson, C., Li, Y. L., Stucky, G. D., Moskovits, M. and Wodtke, A. M., TiO_2 Nanowire Growth Driven by Phosphorus-Doped Nanocatalysis. *J Phys Chem C* **114**, 10697 (2010).

[91] Sedach, P. A., Gordon, T. J., Sayed, S. Y., Furstenhaupt, T., Sui, R. H., Baumgartner, T. and Berlinguette, C. P., Solution Growth of Anatase TiO_2 Nanowires from Transparent Conducting Glass Substrates. *J Mater Chem* **20**, 5063 (2010).

[92] Wakaya, F., Miki, M., Fukuyama, C., Murakami, K., Abo, S. and Takai, M., Fabrication and Electron Field-Emission Properties of Titanium Oxide Nanowire on Glass Substrate. *J Vac Sci Technol B* **28**, C2b24 (2010).

[93] Yu, C. and Park, J., Thermal Annealing Synthesis of Titanium-Dioxide Nanowire-Nanoparticle Hetero-Structures. *J Solid State Chem* **183**, 2268 (2010).

[94] Chen, X. and Mao, S. S., Titanium Dioxide Nanomaterials: Synthesis, Properties, Modifications, and Applications. *Chem Rev* **107**, 2891 (2007).

[95] Li, Y. L. and Ishigaki, T., Controlled One-Step Synthesis of Nanocrystalline Anatase and Rutile TiO_2 Powders by in-Flight Thermal Plasma Oxidation. *J Phys Chem B* **108**, 15536 (2004).

[96] Wang, W. Z., Varghese, O. K., Paulose, M., Grimes, C. A., Wang, Q. L. and Dickey, E. C., A Study on the Growth and Structure of Titania Nanotubes. *J Mater Res* **19**, 417 (2004).

[97] Poudel, B., Wang, W. Z., Dames, C., Huang, J. Y., Kunwar, S., Wang, D. Z., Banerjee, D., Chen, G. and Ren, Z. F., Formation of Crystallized Titania Nanotubes and Their Transformation. Into Nanowires. *Nanotechnology* **16**, 1935 (2005).

[98] Xu, C. K., Zhan, Y. J., Hong, K. Q. and Wang, G. H., Growth and Mechanism of Titania Nanowires. *Solid State Commun* **126**, 545 (2003).

[99] Adachi, M., Murata, Y., Takao, J., Jiu, J. T., Sakamoto, M. and Wang, F. M., Highly Efficient Dye-Sensitized Solar Cells with a Titania Thin-Film Electrode Composed of a Network Structure of Single-Crystal-Like TiO_2 Nanowires Made by the "Oriented Attachment" Mechanism. *J Am Chem Soc* **126**, 14943 (2004).

[100] Qi, L. M. and Zhang, D. Y., Synthesis of Mesoporous Titania Networks Consisting of Anatase Nanowires by Templating of Bacterial Cellulose Membranes. *Chem Commun* 2735 (2005).

[101] Stengl, V., Bakardjieva, S., Murafa, N., Vecernikova, E., Subrt, J. and Balek, V., Preparation and Characterization of Titania Based Nanowires. *J Nanopart Res* **9**, 455 (2007).

[102] Boercker, J. E., Enache-Pommer, E. and Aydil, E. S., Growth Mechanism of Titanium Dioxide Nanowires for Dye-Sensitized Solar Cells. *Nanotechnology* **19**, 095604 (2008).

[103] Huber, B., Gnaser, H. and Ziegler, C., Characterization of Nanocrystalline Anatase TiO_2 Thin Films. *Anal Bioanal Chem* **375**, 917 (2003).

[104] Choi, Y., Yamamoto, S., Umebayashi, T. and Yoshikawa, A., Fabrication and Characterization of Anatase TiO_2 Thin Film on Glass Substrate Grown by Pulsed Laser Deposition. *Solid State Ionics* **172**, 105 (2004).

[105] Huber, B., Gnaser, H. and Ziegler, C., Electrical Properties of Nanocrystalline Anatase TiO_2 Thin Films with Different Crystallite Size. *Surf Sci* **566**, 419 (2004).

[106] Yang, H., Shen, Q. H., Gao, J. W. and Yang, J. G., Low-Temperature Fabrication of Porous Anatase TiO_2 Film with Tiny Slots and Its Photocatalytic Activity. *Mater Lett* **61**, 4160 (2007).

[107] Nan, C. W., Zhou, X. S., Li, L. J. and Lin, Y. H., Characterization and Properties of Anatase Tio(2) Film Prepared Via Colloidal Sot Method under Low Temperature. *Journal of electroceramics* **21**, 795 (2008).

[108] Ho, G. W. and Agarwala, S., Synthesis and Tuning of Ordering and Crystallinity of Mesoporous Titanium Dioxide Film. *Mater Lett* **63**, 1624 (2009).

[109] Long, M. C., Wu, Y. H., Cai, W. M., Dai, S. D., Chen, C., Wu, D. Y. and Bai, J., Preparation of Photocatalytic Anatase Nanowire Films by in Situ Oxidation of Titanium Plate. *Nanotechnology* **20**, 185703 (2009).

[110] Gu, G. R., Li, Y. A., Tao, Y. C., He, Z., Li, J. J., Yin, H., Li, W. Q. and Zhao, Y. N., Investigation on the Structure of Tio(2) Films Sputtered on Alloy Substrates. *Vacuum* **71**, 487 (2003).

[111] Zhang, X. R., Lin, S., He, J., Li, G. H. and Zhang, L. D., Investigation of Thermal Diffusivity of Nano-Structured TiO_2 Films. *Review of Progress in Quantitative Nondestructive Evaluation, Vols 22a and 22b* **20**, 1292 (2003).

[112] Lambropoulos, J. C., Jolly, M. R., Amsden, C. A., Gilman, S. E., Sinicropi, M. J., Diakomihalis, D. and Jacobs, S. D., Thermal-Conductivity of Dielectric Thin-Films. *J Appl Phys* **66**, 4230 (1989).

[113] Wu, Z. L., Reichling, M., Hu, X. Q., Balasubramanian, K. and Guenther, K. H., Absorption and Thermal-Conductivity of Oxide Thin-Films Measured by Photothermal Displacement and Reflectance Methods. *Appl Optics* **32**, 5660 (1993).

[114] Cahill, D. G. and Allen, T. H., Thermal-Conductivity of Sputtered and Evaporated Sio2 and TiO_2 Optical Coatings. *Appl Phys Lett* **65**, 309 (1994).

[115] Lee, S. M., Cahill, D. G. and Allen, T. H., Thermal-Conductivity of Sputtered Oxide-Films. *Phys Rev B* **52**, 253 (1995).

[116] Kim, S. W., Mun, J., Kato, R., Hatta, I., Lee, S. H. and Kang, K. H., Measurement of the Thermal Conductivity of TiO_2 Thin Films by Using the Thermo-Reflectance Method. *Thermochim Acta* **455**, 55 (2007).

[117] Martan, J., Herve, O. and Lang, V., Two-Detector Measurement System of Pulse Photothermal Radiometry for the Investigation of the Thermal Properties of Thin Films. *J Appl Phys* **102**, 064903 (2007).

[118] Fang, J., Reitz, C., Brezesinski, T., Nemanick, E. J., Kang, C. B., Tolbert, S. H. and Pilon, L., Thermal Conductivity of Highly-Ordered Mesoporous Titania Thin Films from 30 to 320 K. *J Phys Chem C* **115**, 14606 (2011).

[119] Kim, P., Shi, L., Majumdar, A. and McEuen, P. L., Thermal Transport Measurements of Individual Multiwalled Nanotubes. *Phys Rev Lett* **87**, 215502 (2001).

[120] Shi, L., Li, D. Y., Yu, C. H., Jang, W. Y., Kim, D., Yao, Z., Kim, P. and Majumdar, A., Measuring Thermal and Thermoelectric Properties of One-Dimensional Nanostructures Using a Microfabricated Device. *J Heat Trans-T Asme* **125**, 881 (2003).

[121] Li, D. Y., Wu, Y. Y., Kim, P., Shi, L., Yang, P. D. and Majumdar, A., Thermal Conductivity of Individual Silicon Nanowires. *Appl Phys Lett* **83**, 2934 (2003).

[122] Shi, L., Yu, C. H., Saha, S., Zhou, J. H., Cassell, A. M., Cruden, B. A., Ngo, Q. and Li, J., Thermal Contact Resistance and Thermal Conductivity of a Carbon Nanofiber. *J Heat Trans-T Asme* **128**, 234 (2006).

[123] Zhang, Y., Christofferson, J., Shakouri, A., Li, D. Y., Majumdar, A., Wu, Y. Y., Fan, R. and Yang, P. D., Characterization of Heat Transfer Along a Silicon Nanowire Using Thermoreflectance Technique. *Ieee T Nanotechnol* **5**, 67 (2006).

[124] Yang, R. G., Chen, G. and Dresselhaus, M. S., Thermal Conductivity of Simple and Tubular Nanowire Composites in the Longitudinal Direction. *Phys Rev B* **72**, 125418 (2005).

[125] Beppu, T., Yamaguchi, S. and Hayase, S., Improvement of Heat Resistant Properties of TiO_2 Nanowires and Application to Dye-Sensitized Solar Cells. *Jpn J Appl Phys 1* **46**, 4307 (2007).

[126] Guo, J. Q., Wang, X. W. and Wang, T., Thermal Characterization of Microscale Conductive and Nonconductive Wires Using Transient Electrothermal Technique. *J Appl Phys* **101**, 063537 (2007).

[127] Hou, J. B., Wang, X. W. and Guo, J. Q., Thermal Characterization of Micro/Nanoscale Conductive and Non-Conductive Wires Based on Optical Heating and Electrical Thermal Sensing. *J Phys D Appl Phys* **39**, 3362 (2006).

[128] Wang, T., Wang, X. W., Guo, J. Q., Luo, Z. Y. and Cen, K., Thermal Characterization of Micro/Nanoscale Conductive and Nonconductive Wires by Transient Photo-Electro-Thermal Technique. *Proceedings of the Micro/Nanoscale Heat Transfer International Conference 2008, Pts a and B* 1119 (2008).

[129] Kumar, G. S., Prasad, G. and Pohl, R. O., Experimental Determinations of the Lorenz Number. *J Mater Sci* **28**, 4261 (1993).

[130] R. W. Powell, R. P. T. a. M. J. W., Thermal Conductivities and Electrical Resistivities of the Platinum Metals. *Platinum Metals Rev.* **6**, 138 (1962).

[131] Parker, W. J., Jenkins, R. J., Abbott, G. L. and Butler, C. P., Flash Method of Determining Thermal Diffusivity, Heat Capacity, and Thermal Conductivity. *J Appl Phys* **32**, 1679 (1961).

[132] Baibarac, M., Lapkowski, M., Pron, A., Lefrant, S. and Baltog, I., Sers Spectra of Poly(3-Hexylthiophene) in Oxidized and Unoxidized States. *J Raman Spectrosc* **29**, 825 (1998).

[133] Sugiyama, K., Kojima, T., Fukuda, H., Yashiro, H., Matsuura, T. and Shimoyama, Y., Esr and X-Ray Diffraction Studies on Thin Films of Poly-3-Hexylthiophene: Molecular Orientation and Magnetic Interactions. *Thin Solid Films* **516**, 2691 (2008).

[134] Feng, X., Wang, X., Chen, X. and Yue, Y., Thermo-Physical Properties of Thin Films Composed of Anatase Tio(2) Nanofibers. *Acta Mater* **59**, 1934 (2011).

[135] Choy, C. L., Wong, S. P. and Young, K., Model Calculation of the Thermal-Conductivity of Polymer Crystals. *J Polym Sci Pol Phys* **23**, 1495 (1985).

[136] Ohsaka, T., Izumi, F. and Fujiki, Y., Raman-Spectrum of Anatase, TiO_2. *J Raman Spectrosc* **7**, 321 (1978).

[137] Touloukian, Y. S. P., R. W.; Ho, C. Y.; Klemens, P. G. 1970 *Thermophyiscal Properties of Matter-Thermal Conductivity of Non-Metallic Solids* vol 2 (New York: IFI/Plenum)

[138] Smith, S. J., Stevens, R., Liu, S. F., Li, G. S., Navrotsky, A., Boerio-Goates, J. and Woodfield, B. F., Heat Capacities and Thermodynamic Functions of Tio(2) Anatase and Rutile: Analysis of Phase Stability. *Am Mineral* **94**, 236 (2009).

[139] Shojaee, E. and Mohammadizadeh, M. R., First-Principles Elastic and Thermal Properties of TiO_2: A Phonon Approach. *J Phys-Condens Mat* **22**, 015401 (2010).

[140] Guo, L. Y., Wang, X. W., Wang, J., Lin, Z. Q. and Gacek, S., Anisotropic Thermal Transport in Highly Ordered TiO_2 Nanotube Arrays. *J Appl Phys* **106**, 123526 (2009).

[141] Feng, X. H. and Wang, X. W., Thermophysical Properties of Free-Standing Micrometer-Thick Poly(3-Hexylthiophene) Films. *Thin Solid Films* **519**, 5700 (2011).